8-25-1995

Matched wavelet construction and its application to target detection

Joseph Chapa

Matched Wavelet Construction and Its Application to Target Detection

by
Major Joseph O. Chapa, USAF

B.S. Illinois College (1981)
B.E.E. Auburn University (1983)
M.S. Stanford University (1986)

A thesis submitted in partial fulfillment of the
requirements for the degree of Ph.D. in the
Center for Imaging Science
Rochester Institute of Technology

August 25, 1995

Signature of the Author Joseph O. Chapa

Accepted by Dr. Mark Fairchild, Coordinator, Ph.D. Degree Program — 8/25/95 Date

CENTER FOR IMAGING SCIENCE
ROCHESTER INSTITUTE OF TECHNOLOGY
ROCHESTER, NEW YORK

CERTIFICATE OF APPROVAL

Ph.D. DEGREE DISSERTATION

The Ph.D. Degree Dissertation of Joseph O. Chapa
has been examined and approved by the
dissertation committee as satisfactory for the
dissertation requirement for the
Ph.D. degree in Imaging Science

Dr. Mysore Raghuveer, Thesis Advisor

Dr. Edwin Hoefer

Dr. Harvey Rhody

Dr. Navalgund Rao

August 25, 1995

Date

THESIS RELEASE PERMISSION
ROCHESTER INSTITUTE OF TECHNOLOGY
CENTER FOR IMAGING SCIENCE

Title of Thesis: Matched Wavelet Construction and Its Application to Target Detection

I, Joseph O. Chapa, hereby grant permission to the Wallace Memorial Library of R.I.T. to reproduce my thesis in whole or in part. Any reproduction will not be for commercial use or profit.

Signature: _____

Date: 8/25/95

ACKNOWLEDGEMENTS

I wish to acknowledge my Sovereign God for his love and provision and for faith in Christ which He worked in me and for the hope that He gave me from the first day of this school assignment, through every obstacle and every success.

I wish to thank my loving wife, Debbie, for her patience, love, support, and encouragement during the course of this Ph.D. program. I would also like to thank my children, Katie, Joey, Frank, and Becky for their love and understanding even during times of stress in their Dad's life.

I wish to thank my advisor, Dr. Mysore Raghuveer, for his patience, guidance, and knowledge as he helped me through my research and for teaching me, by example, the difference between a student and a scholar.

I wish to thank my committee, Dr. Edwin Hoefer, Dr. Harvey Rhody, and Dr. Navalgund Rao for their comments and critiques.

Abstract

This dissertation develops a new wavelet design technique that produces a wavelet that matches a desired signal in the least squares sense. The Wavelet Transform has become very popular in signal and image processing over the last 6 years because it is a linear transform with an infinite number of possible basis functions that provides localization in both time (space) and frequency (spatial frequency).

The Wavelet Transform is very similar to the matched filter problem, where the wavelet acts as a zero mean matched filter. In pattern recognition applications where the output of the Wavelet Transform is to be maximized, it is necessary to use wavelets that are specifically matched to the signal of interest. Most current wavelet design techniques, however, do not design the wavelet directly, but rather, build a composite wavelet from a library of previously designed wavelets, modify the bases in an existing multiresolution analysis or design a multiresolution analysis that is generated by a scaling function which has a specific corresponding wavelet. In this dissertation, an algorithm for finding both symmetric and asymmetric matched wavelets is developed. It will be shown that under certain conditions, the matched wavelets generate an orthonormal basis of the Hilbert space containing all finite energy signals. The matched orthonormal wavelets give rise to a pair of Quadrature Mirror Filters (QMF) that can be used in the fast Discrete Wavelet Transform. It will also be shown that as the conditions are relaxed, the algorithm produces dyadic wavelets which when used in the Wavelet Transform provides significant redundancy in the transform domain.

Finally, this dissertation develops a shift, scale and rotation invariant technique for detecting an object in an image using the Wavelet Radon Transform (WRT) and matched wavelets. The detection algorithm consists of two levels. The first level detects the location, rotation and scale of the object, while the second level detects the fine details in the object. Each step of the wavelet matching algorithm and the object detection algorithm is demonstrated with specific examples.

Contents

List of Figures

List of Tables

Chapter 1

Introduction

For many years, the primary linear mathematical analysis tool used to transform signal information was the Fourier Transform. However, the end of the 1980's saw the development of an alternative mathematical framework, called the wavelet transform, with applications in signal and image analysis [30]. While much of the theory associated with it is not new and can be described in a Hilbert space setting, it did provide a consolidated framework for a number of previously diverse disciplines, like multiresolution analysis used in computer vision, subband coding developed for speech and image compression, and orthonormal basis expansions developed in applied mathematics [30].

The Fourier Transform of a signal, $f(x)$, given by

$$F(\omega) = \int_{-\infty}^{\infty} f(x) e^{-i\omega x} dx, \tag{1.1}$$

is a projection operation onto the basis formed by dilating the complex exponential, e^{ix}. The Wavelet Transform, given by

$$W_{\psi}(a,b) = \int_{-\infty}^{\infty} f(x) |a|^{-\frac{1}{2}} \psi\left(\frac{x-b}{a}\right) dx, \tag{1.2}$$

is a projection operation onto the basis formed by dilating and *shifting* a "mother" wavelet, $\psi(x)$, which is zero mean and decays very rapidly in x. These properties of the wavelet provide an advantage over Fourier analysis because the Wavelet Transform can achieve localization in both time and frequency or in the case of images, space and spatial frequency [10]. That is to say that the Wavelet Transform can provide information about the frequency content of a particular group of pixels. Another advantage of

wavelet analysis over Fourier analysis is the flexibility in the transform operator used for decomposition or signal representation. Fourier methods are locked into bases that are based on the complex exponential kernel, e^{ix}. Wavelet transforms can have many different operators. They may or may not be orthogonal, and they may or may not form bases. Even in the case of orthonormal bases, there are still infinitely many wavelets that satisfy the appropriate conditions. Because of this flexibility, it is possible, and wise, to choose or design a wavelet that is matched to the application.

Many wavelet design techiques have been developed since the early theoretical work of the wavelet pioneers. However, most of the techniques do not directly match a wavelet to a signal of interest. Many build adaptive wavelets from existing wavelets and their effectiveness is dependent on the effectiveness of the existing wavelets used. Others impose requirements on the wavelets to ensure some degree of smoothness or differentiability, which guarantees the wavelet to exhibit certain properties, but does not guarantee anything with regards to its shape.

Using adaptive wavelets for image pattern recognition is very attractive because of the scale (or zoom) insensitivity of the wavelet transform. For instance, if a wavelet can be constructed that matches a pattern of interest in an image, then the peak of the wavelet transform (or lack thereof) will indicate whether the pattern is present (or not) and due to the localization properties of the wavelet, where the pattern is located. Applying the Continous Wavelet Transform (CWT) to the image would be too data intensive because of the redundancy contained in the CWT. The 2-D Discrete Wavelet transform is much faster because it processes the projection coefficients only. However, it is not shift or rotation invariant, making its application to pattern recognition of limited use.

These two problems, wavelet matching and application to pattern recognition are addressed in this dissertation. First, a wavelet design algorithm is developed that takes any 1-D signal as input and finds the wavelet that comes closest to it in the least squares sense. The algorithm assumes that the wavelet is bandlimited. The bandlimit conditions can be set such that the resultant wavelet is an orthonormal basis of the function space $L^2(\Re)$, or they can be relaxed or widened, so that the algorithm generates a "dyadic" wavelet. Second, a target detection and identification algorithm is developed based on the Radon Transform, and the Continuous Wavelet Transform using matched wavelets. The target detec-

tion algorithm is shift, scale and rotation invariant. The Radon Transform is used to reduce the data burden on the CWT and to provide some degree of rotation invariance. Using matched wavelets in the CWT provides scale and shift invariance as well as optimal amplitude detection. The matched wavelet algorithm in conjunction with the target detection algorithm provide a thorough framework from which more detailed target classification algorithms could be developed.

This dissertation provides an in-depth review of wavelet theory, first in Chapter 2 with a short review of Hilbert spaces and a comparison between Fourier and Wavelet analysis. Chapter 3 provides an historical chronology of the development of wavelet theory from the Continuous Wavelet Transform of Morlet and Grossman to multiresolution analyses and the Discrete Wavelet Transform of Mallat. Several current wavelet design techniques are presented in Chapter 4 as motivation for the matching algorithm developed in Chapter 5. Chapter 6 gives several examples of the wavelet matching algorithm to demonstrate its performance and to assist anyone trying to implement the algorithm themselves. After a summary of the Radon Transform and image reconstruction using backprojection, Chapter 7 provides the step by step development of the target detection and identification algorithm taking advantage of the matched wavelet algorithm of Chapter 5. Chapter 8 provides a summary of the research results contained in this dissertation, and the Appendix contains proofs to many of the theorems.

Chapter 2

Background

This chapter contains brief background material that will be helpful in understanding the development of wavelet analysis. The first section contains definitions of terms used throughout the dissertation, and an introduction to Hilbert spaces, the projection theorem and its application to signal representations in Hilbert spaces. The Fourier series is shown to be a direct application of the projection theorem on the Hilbert space of all periodic, finite energy signals. The limitations of Fourier analysis on real world signals are indentified followed by the introduction of the Short Time Fourier Transform (STFT). The last section introduces wavelet analysis as a recent solution to the limitations of Fourier analysis and the STFT. More detailed development of wavelet theory will be provided in Chapter 3.

2.1 Hilbert Spaces

The Hilbert space is a complete, linear vector space with a norm $\|\cdot\|$ and an inner product $\langle\cdot,\cdot\rangle$ defined [22]. There are two Hilbert spaces used in wavelet analysis, $L^2(\Re)$, and, $l^2(\mathbb{Z})$, where $\Re$ is the set of all real numbers and $\mathbb{Z}$ is the set of all integers.

Definition 1 *The Hilbert space $L^2(\Re)$ consists of complex-valued, measurable functions, x(t), on the real line, $\Re$, where*

$$\int_{-\infty}^{\infty} |x(t)|^2 dt < \infty \tag{2.1}$$

and the integral is the Lebesque integral. The norm of $x \in L^2(\Re)$ *is defined as*

$$\|x\| = \left(\int_{-\infty}^{\infty} |x(t)|^2 dt \right)^{\frac{1}{2}}. \tag{2.2}$$

The inner product of $x, y \in L^2(\Re)$ *is defined as*

$$\langle x, y \rangle = \int_{-\infty}^{\infty} x(t)\overline{y(t)}dt \tag{2.3}$$

where $\overline{y(t)}$ *is the complex conjugate of* $y(t)$.

Definition 2 *The Hilbert space* $l^2(\mathbb{Z})$ *consists of all complex valued sequences of scalars* $x = \{\ldots, \eta_{-1}, \eta_0, \eta_1, \ldots\}$ *for which*

$$\sum_{i=-\infty}^{\infty} |\eta_i|^2 < \infty \tag{2.4}$$

for all $i \in \mathbb{Z}$, *the integer number line. The norm of* x *is defined as*

$$\|x\| = \left(\sum_{i=-\infty}^{\infty} |\eta_i|^2 \right)^{\frac{1}{2}}. \tag{2.5}$$

The inner product of $x = \{\ldots, \eta_{-1}, \eta_0, \eta_1, \ldots\}$ *and* $y = \{\ldots, \nu_{-1}, \nu_0, \nu_1, \ldots\}$ *is defined as*

$$\sum_{i=-\infty}^{\infty} \eta_i \nu_i. \tag{2.6}$$

A set of vectors in a Hilbert space, $x_i \in H$, is said to be orthonormal if $x_i \perp x_j$ for $i \neq j$ for all $x_i \in H$ and if each vector has unit norm, that is,

$$\langle x_i, x_j \rangle = \begin{cases} 1 & \text{for } i = j \\ 0 & \text{for } i \neq j \end{cases}. \tag{2.7}$$

The projection theorem is a fundamental theorem used in vector space analysis and is used to formulate the mathematics of both Fourier and wavelet decompositions for functions in Hilbert spaces.

Theorem 1 Projection Theorem *Let* H *be a Hilbert space and* M *a closed subspace of* H. *Corresponding to any vector* $x \in H$, *there is a unique vector* $m_0 \in M$ *such that* $\|x - m_0\| \leq \|x - m\|$ *for all* $m \in M$. *Furthermore, a necessary and sufficient condition that* $m_0 \in M$ *be the unique minimizing vector is that* $x - m_0$ *be orthogonal to* M *[22].*

The Projection Theorem states that if we want to construct a vector $m_0 \in M$, a subspace of H, then we can do so uniquely. Furthermore, the vector that best approximates x will be the one that minimizes the norm of the error vector, $\|x - m_0\|$, and the error vector, $x - m_0$, will be orthogonal to the approximation subspace, M (Figure 2.1) [22].

Suppose we want to construct an approximation of $x \in H$ from a set of vectors $y = \{y_1, y_2, \ldots, y_n\} \in M$, where M is a closed subspace of H and y is a basis of M. Then, the approximation, or projection

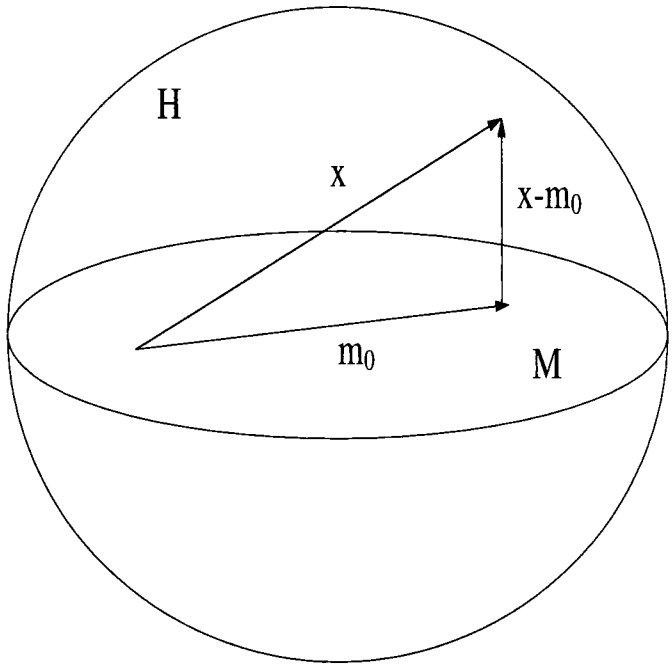

Figure 2.1: Orthonormal projection

of x onto M is a linear combination of y_i

$$(P_M x) = \sum_{i=1}^{n} \alpha_i y_i \tag{2.8}$$

where P_M is the projection operator onto the subspace M [22]. From the Projection Theorem, the best approximation of x will be the one that minimizes $\|x - P_M x\|$ and $x - P_M x$ will be orthogonal to all elements of y, that is,

$$\langle x - P_M x, y_i \rangle = 0. \tag{2.9}$$

Substituting (2.8) into (2.9) gives

$$\langle x - \sum_{j=1}^{n} \alpha_j y_j, y_i \rangle = 0. \tag{2.10}$$

Since the Hilbert space is linear and the inner product is a linear operator, (2.10) can be rewritten as

$$\langle x, y_i \rangle = \sum_{j=1}^{n} \alpha_j \langle y_j, y_i \rangle. \tag{2.11}$$

If $y \in M$ is an orthonormal basis of M, then $\langle y_i, y_j \rangle = 0$ for $i \neq j$ and $\|y_i\| = 1$. Equation (2.11) reduces to

$$\langle x, y_i \rangle = \alpha_i \tag{2.12}$$

making (2.8)

$$(P_M x) = \sum_{i=1}^{n} \langle x, y_i \rangle y_i. \tag{2.13}$$

Equation (2.13) gives the expression for the projection of the vector x onto an orthonormal basis y of M [22].

2.2 Fourier Analysis

Signal and image analysis has long benefited from Fourier analysis, where the set of functions, $e^{i2\pi kx/T}$, forms an orthonormal basis of $L^2(0,T)$, the Hilbert space consisting of all square integrable functions defined on the interval $[0,T]$. All periodic functions, with period T, also reside in $L^2(0,T)$, since they can be completely described by one period on the interval $[0,T]$. Since $L^2(0,T)$ is a Hilbert space, it has an inner product and a norm [10] defined as

$$\langle f, g \rangle = \frac{1}{T} \int_0^T f(x)\overline{g(x)}dx \tag{2.14}$$

$$\|f\| = \langle f, f \rangle = \left(\frac{1}{T} \int_0^T |f(x)|^2 dx \right)^{-\frac{1}{2}} \tag{2.15}$$

Since $e^{i2\pi kx/T}$ is an orthonormal basis of $L^2(0,T)$, $f(x) \in L^2(0,T)$ can be represented using (2.13) and (2.12),

$$f(x) = \sum_{k=-\infty}^{\infty} c_k e^{i\frac{2\pi kx}{T}} \tag{2.16}$$

$$c_k = \langle f(x), e^{i\frac{2\pi kx}{T}} \rangle = \frac{1}{T}\int_0^T f(x)e^{-i\frac{2\pi kx}{T}}dx. \tag{2.17}$$

The function, f, is decomposed into the sum of infinitely many mutually orthogonal components, $g_k(x) = c_k e^{i2\pi kx/T}$, where orthogonality means:

$$\langle g_n, g_m \rangle = 0, \quad \text{for all } m \neq n. \tag{2.18}$$

That (2.18) holds is a consequence of the fact that:

$$w_k(x) = e^{i2\pi kx/T} \qquad k = \{\ldots, -1, 0, 1, \ldots\} \tag{2.19}$$

is an orthonormal basis of $L^2(0,T)$ [10]. It is important to note further that the orthonormal basis, w_k, is formed by dilating (known as integral dilation) a single function, $e^{i2\pi x}$ Chui [10] emphasizes the significance of these facts in the introduction to his book:

> Let us summarize this remarkable fact by saying that *every 2π-periodic square integrable function is generated by a "superposition" of integral dilations of the basic function $w(x) = e^{ix}$.*

Chui develops his section on Fourier analysis assuming a period of 2π, thereby giving rise to his mention of 2π-periodic functions and the basic function e^{ix}

The decomposition in (2.16) and (2.17) is known as the Fourier series expansion of $f(x)$[17]. The basis, $e^{i2\pi kx/T}$, is a complex exponential with fundamental frequency, $\xi_0 = 1/T$. Integer multiples of the fundamental frequency are called harmonics. So, a periodic function of period T, can be perfectly represented by the sum of a complex exponential at a fundamental frequency and its harmonics. The weights of these complex exponential components, c_k, constitute the frequency spectrum of f. It is often called the line spectrum because it is discrete.

Square integrable, non-periodic, functions whose domain is the real number line, $\Re$, constitute the Hilbert space, $L^2(\Re)$, with its inner product and norm defined as:

$$(f, g\rangle = \int_{-\infty}^{\infty} f(x)\overline{g(x)}dx \tag{2.20}$$

$$\|f\| = \left[\int_{-\infty}^{\infty} |f(x)|^2 dx\right]^{-\frac{1}{2}}. \tag{2.21}$$

The Fourier series of $f(x) \in L^2(\Re)$ does not exist since f is non-periodic and its domain is the entire real line, $\Re$. The frequency spectrum of f can still be determined by taking its inner product with the function, $e^{i2\pi\xi x}$, where ξ is the continuous frequency variable[17]. Letting $\omega = 2\pi\xi$ gives

$$F(\omega) = (\mathcal{F}f)(\omega) = \langle f(x), e^{i\omega x} \rangle = \int_{-\infty}^{\infty} f(x)e^{-i\omega x}dx. \tag{2.22}$$

$F(\omega)$ is the Fourier Transform of $f(x)$ and is at least piecewise continuous[17]. The Fourier Transform can be interpreted in a manner similar to the Fourier series. A non-periodic, square integrable function, $f(x) \in L^2(\Re)$ can be represented by the integral sum of complex exponentials with weights given by the frequency spectrum, $F(\omega)$,

$$f(x) = \frac{1}{2\pi} \int_{-\infty}^{\infty} F(\omega)e^{i\omega x}d\omega. \tag{2.23}$$

The Fourier Series and Fourier Transform are powerful tools for determining the frequency content of discrete and continuous signals. However, in order to study the spectral behavior of analog signals from its Fourier Transform, full knowledge of the signal in the time or space domain must be obtained[10]. In addition, if a signal is altered in a small neighborhood of some time instant, then the entire spectrum is affected. If a signal of some frequency exists for a finite period of time, the Fourier Transform does not give visibility into where in time the signal occurred. Being able to determine where in time a signal of some frequency occurs is called time localization. Being able to determine the frequency content of a signal at a particular frequency is called frequency localization. The Fourier Transform provides excellent frequency localization, but poor time localization [10].

In order to obtain localization in both time and frequency, an additional parameter must be added. Gabor [16] was the first to adapt Fourier analysis to include a modulation window, $g(x)$ [30]. Gabor's Short-Time Fourier Transform (STFT) [30], $S(\tau, \omega)$, is given as

$$S(\tau, \omega) = \int_{-\infty}^{\infty} f(x)\overline{g(x-\tau)}e^{-i\omega}dx. \tag{2.24}$$

The signal is weighted by a finite duration window, $g(x)$, prior to taking the Fourier Transform (Figure 2.2). The additional parameter, τ, is the translation parameter of the window and it provides the additional dimension needed to obtain localization in both time and frequency. If a frequency pulse or burst

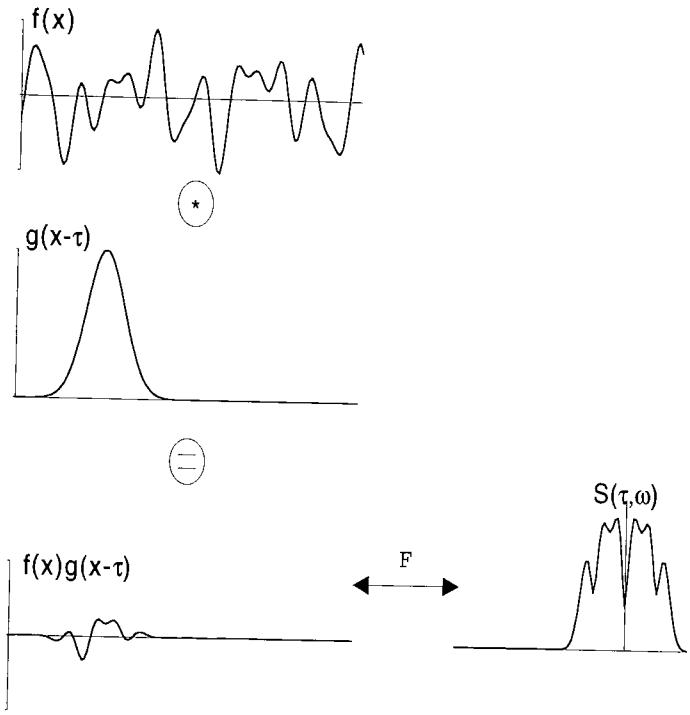

Figure 2.2: Short-Time Fourier Transform

is present in the signal for a finite duration, it will show up in $S(\tau, \omega)$ at values of τ corresponding to the location of the frequency pulse. The function, $S(\tau, \omega)$, provides a two dimensional map of time and frequency (Figure 2.3) [30]. By fixing frequency at some value, ω_0, $S(\tau, \omega_0)$ gives a 1-D function indi-

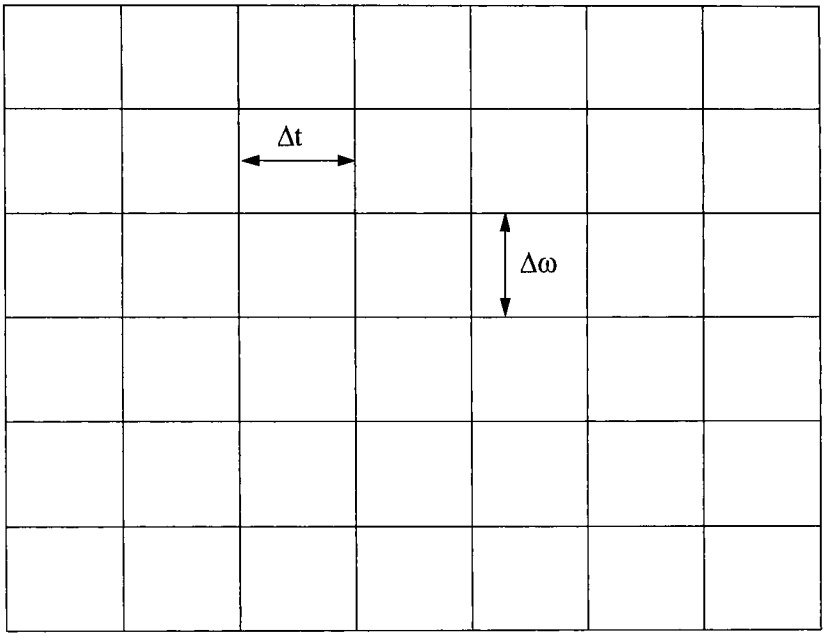

Figure 2.3: Time-frequency map - Short Time Fourier Transform

cating where in time ω_0 existed. Alternatively, by fixing $\tau = \tau_0$, $S(\tau_0, \omega)$ gives the Fourier Transform for that time slice of f. The resolution in both time and frequency depend on the window function $g(t)$. Time and frequency resolutions are traded off according to the uncertainty principle [10, 30]

$$\text{Time-bandwidth product} = \Delta t \Delta \omega \geq \frac{1}{2} \tag{2.25}$$

where Δt and $\Delta \omega$ are the rms measures of time width and bandwidth given by

$$\Delta t = \frac{\left\{ \int_{-\infty}^{\infty} (x - E(g)) \left| g(x) \right|^2 dx \right\}^{\frac{1}{2}}}{\|g\|} \tag{2.26}$$

$$\Delta \omega = \frac{\left\{ \int_{-\infty}^{\infty} (\omega - E(G)) \left| G(\omega) \right|^2 d\omega \right\}^{\frac{1}{2}}}{\|G\|}. \tag{2.27}$$

$G(\omega)$ is the Fourier Transform of $g(x)$ and the operator, $E(\cdot)$ is given as

$$E(f) = \frac{\int_{-\infty}^{\infty} x\,|f(x)|^2\,dx}{\|f\|^2}. \tag{2.28}$$

For this reason, a gaussian window is often used since it satisfies the equality of (2.25) [30]. However, modulating the signal with a gaussian window correlates the Fourier coefficients and therefore destroys orthonormality. Furthermore, the window function, $g(x)$, with its corresponding frequency spectrum, $G(\omega)$, sets both the time and frequency resolutions for the entire time-frequency plane. This is a disadvantage for analyzing signals with both high and low frequencies [10]. In order to properly represent a signal of some fundamental frequency, the window must contain one or more periods of that signal. Low frequency signals, therefore, require long time windows, which corresponds to high resolution in the frequency domain. High frequency signals require a small time window in order to capture one or more periods. The small time window corresponds to low resolution in the frequency domain. The STFT's window widths are fixed in both time and frequency, as illustrated in Figure 2.3, and therefore, cannot effectively analyze signals containing both high and low frequencies [10].

The obvious solution to Gabor's Short-Time Fourier Transform is an orthonormal basis of $L^2(\Re)$ that provides both time and frequency localization for signals with high and low frequencies. Wavelet analysis provides just such a solution.

2.3 Wavelet Analysis

The "basic wavelet" or "mother wavelet" is a function, $\psi(x) \in L^2(\Re)$, whose Fourier transform, $\Psi(\omega)$, satisfies the admissibility condition [10, 12, 14, 23, 27]:

$$C_\psi = \int_{-\infty}^{\infty} \frac{|\Psi(\omega)|^2}{|\omega|} d\omega < \infty. \tag{2.29}$$

Since $\psi(x) \in L^2(\Re)$, then

$$\int_{-\infty}^{\infty} \|\psi(x)\|^2\,dx < \infty \tag{2.30}$$

must be true, which means that $\psi(x)$ must have, effectively, finite support. Assuming $\Psi(\omega)$ is continuous, (2.29) and (2.30) imply

$$\Psi(0) = 0, \qquad \stackrel{\mathcal{F}}{\Longleftrightarrow} \qquad \int_{-\infty}^{\infty} \psi(x)dx = 0. \tag{2.31}$$

This is the reason that ψ is called a "wavelet" [10]. In order for ψ to have an average of 0 (2.31), it must be wave-like in nature. In order for it to be in $L^2(\Re)$, it must be effectively finite or of short duration as in (2.30), hence the term "small wave" or "wavelet." Equation (2.31) also indicates that $\psi(x)$ has the characteristics of a bandpass filter.

If we let

$$\psi_{a,b} = |a|^{-\frac{1}{2}}\psi(\frac{x-b}{a}), \tag{2.32}$$

then the continuous wavelet transform (CWT) [10, 12, 30] is defined as

$$W_f(a,b) = \langle f, \psi_{a,b}\rangle = |a|^{-\frac{1}{2}} \int_{-\infty}^{\infty} f(x)\overline{\psi(\frac{x-b}{a})}dx \tag{2.33}$$

where $f(x) \in L^2(\Re)$, $a; b \in \Re$, and $a \neq 0$. The parameters, a and b, are the scale and shift parameters, respectively, and they provide localization in both the time and frequency domains. The parameter b centers the wavelet at $t = b$ and a scales the wavelet function, ψ, on the x-axis. The CWT is analogous to the Fourier Transform where frequency has been replaced by scale, since a gives insight into the frequency content of a passband, not a single frequency. The bandwidth of the passband changes with a [10, 30] such that

$$\frac{\Delta\omega}{\omega} = K. \tag{2.34}$$

This characteristic is common in communication theory and is called "constant Q" (Figure 2.4) [10, 30]. Now, the windowing function is effectively the support of the wavelet, ψ, which changes with a. It is not fixed as in the case of the STFT, and can therefore provide both time and frequency localization of a signal containing both high and low frequencies.

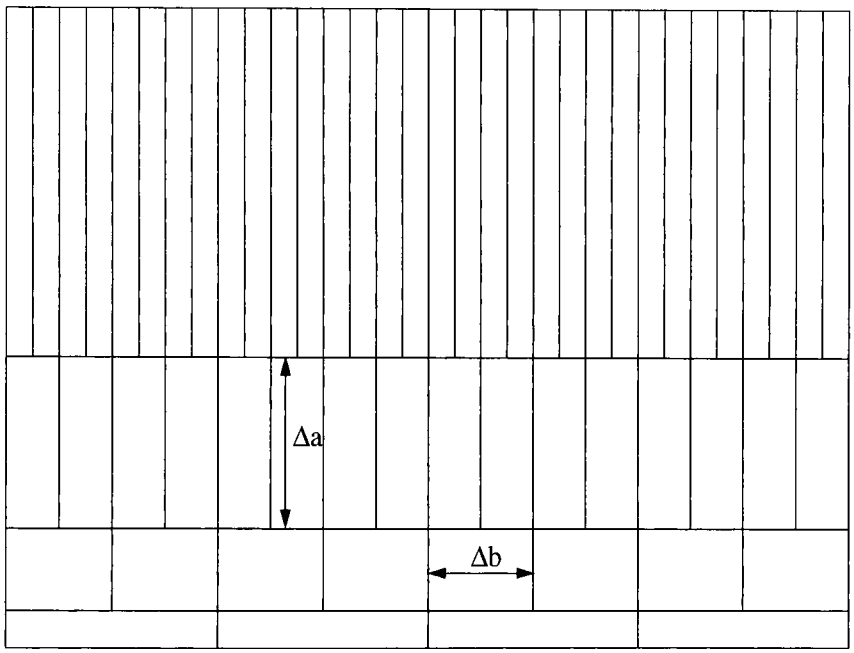

Figure 2.4: Time-scale map - Wavelet Transform

Chapter 3

Wavelet Theory Development

In this chapter, the history of the development of wavelet theory will be presented from the original work of Morlet and Grossman through the algorithm development of Stephane Mallat. The development of wavelet theory was motivated by the need to analyze a finite energy signal with a single, finite energy function, called a wavelet, dilated and shifted by real parameters. It was shown that the condition on the analyzing function was simple and easily met. As the constraints on the dilation and shift parameters tightened, for instance, confinement to $\mathbb{Z}$, the conditions on the analyzing function also increased. It was shown by Meyer that if the dilation parameter values were constrained to be powers of 2 and the shift parameter values to be integer multiples of powers of 2, then a wavelet could be found such that its shifts and dilates formed an orthonormal basis of $L^2(\Re)$. This chapter goes through in chronological order the development of each "class" of wavelet and the conditions associated with each, culminating with orthonormal bases and multiresolution analyses.

3.1 Continuous Wavelet Transform

J. Morlet, a French geophysicist, first proposed the use of "wavelets of constant shape" for analyzing seismic data. His reference to constant shape was intended to contrast these new functions with the Short Time Fourier Transform (STFT), which are not of constant shape [14]. A. Grossman, a French theoretical physicist, showed that Morlet's function, dilated and shifted by real parameters, generated

a square integrable representation of functions in $L^2(\Re)$ and this representation was referred to as the wavelet transform [14, 30]. The wavelet transform is defined as follows:

Definition 3 (Continuous Wavelet Transform) *[10] If $\psi \in L^2(\Re)$ satisfies the "admissibility" condition:*

$$C_\psi = \int_{-\infty}^{\infty} \frac{|\Psi(\omega)|^2}{|\omega|} d\omega < \infty, \tag{3.1}$$

where $\Psi(\omega)$ is the Fourier transform of ψ, then ψ is called a "basic wavelet". Relative to every basic wavelet ψ, the continuous wavelet transform (CWT) on $L^2(\Re)$ is defined by

$$\begin{aligned} W_f(a,b) &= \langle f, \psi_{a,b} \rangle \\ &= \int_{-\infty}^{\infty} f(x)|a|^{-\frac{1}{2}} \overline{\psi\left(\frac{x-b}{a}\right)} dx \end{aligned} \tag{3.2}$$

for $f \in L^2(\Re)$, and $a, b \in \Re$ with $a \neq 0$.

The wavelet operator,

$$\psi_{a,b}(x) = |a|^{-\frac{1}{2}} \psi\left(\frac{x-b}{a}\right), \tag{3.3}$$

is a dilated and shifted version of a single function, $\psi(x)$, sometimes referred to as the mother wavelet, and it maps a one dimensional signal into a two dimensional analysis domain, that is, scale, a, and shift, b. This mapping provides visibility into the frequency content of a signal through the scale parameter, a, and time localization through the shift parameter, b, a significant advantage over standard Fourier analysis. Figure 3.1 shows the effect of the dilation and shift parameters, a and b on the wavelet operator. The wavelet shown, used by Morlet andGrossman, is a cosine function modulated by a gaussian window. Notice that as a increases, the wavelet gets wider and shorter in height and when a decreases, the wavelet gets thinner and taller. This effect provides a zoom-in, zoom-out capability in the frequency domain. The bandwidth of the wavelet for small a is large and the bandwidth for large a is small. Of course, changes in b shift the wavelet up and down the x-axis giving full two dimensional latitude in both time and frequency. The admissibility condition (3.1) on ψ implies

$$\Psi(0) = 0 \qquad \overset{\mathcal{F}}{\Longleftrightarrow} \qquad \int_{-\infty}^{\infty} \psi(x) dx = 0. \tag{3.4}$$

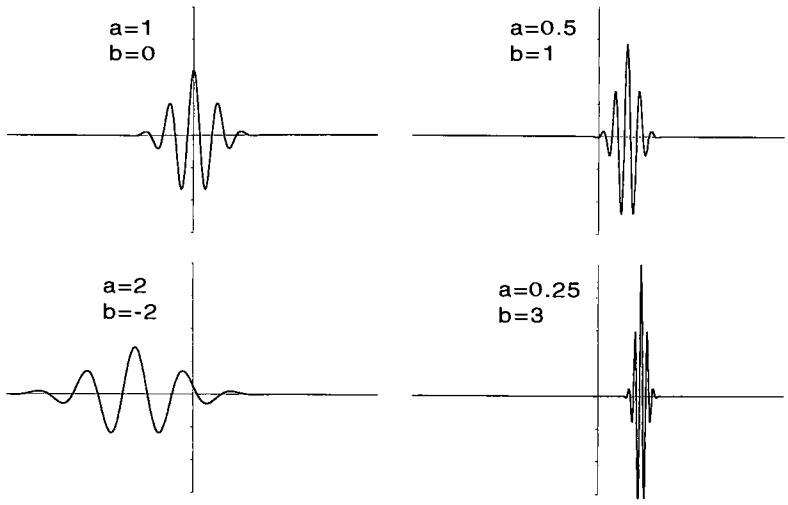

Figure 3.1: The Gabor or Morlet wavelet

Therefore, ψ has an average value of 0, acts like a highpass or bandpass filter and hence must oscillate. The fact that $\psi \in L^2(\Re)$ means that ψ has finite energy and therefore must fall off fairly rapidly. These two features are what motivated Morlet and Grossman to refer to these functions as "wavelets" or short waves.

The admissibility condition (3.1) was not specifically derived with these features in mind. Rather, the admissibility condition is necessary for the inverse transform to exist and for the inverse wavelet operator itself to be a shifted and dilated version of a mother wavelet, referred to as the dual of ψ.

Theorem 2 (Inverse Wavelet Transform) *[10] Let ψ be a basic wavelet which defines a CWT, W_f. Then*

$$f(x) = \frac{1}{C_\psi} \int_{-\infty}^{\infty} \int_{-\infty}^{\infty} W_f(a,b)\psi_{a,b}(x) \frac{dadb}{a^2} \tag{3.5}$$

□

Kaiser [19] provides a very understandable derivation of both the Inverse Wavelet Transform and the admissibility condition that is worth including here, since it will be used later to determine the conditions

for dyadic wavelets and frames. Using Parseval's theorem, (3.2) can be rewritten as

$$W_f(a,b) = \langle f, \psi_{a,b} \rangle = \langle F, \Psi_{a,b} \rangle \tag{3.6}$$

where $F(\xi)$ is the Fourier Transform of $f(x)$ and $\Psi_{a,b}(\xi)$ is the Fourier Transform of $\psi_{a,b}(x)$, given as

$$\Psi_{a,b}(\xi) = |a|^{\frac{1}{2}} e^{-i2\pi\xi b} \Psi(a\xi) \tag{3.7}$$

where $\Psi(\xi)$ is the Fourier Transform of $\psi(x)$. Expanding the inner product of (3.6) gives

$$\begin{aligned} W_f(a,b) &= \int_{-\infty}^{\infty} F(\xi) \overline{|a|^{\frac{1}{2}} \Psi(a\xi) e^{-i2\pi\xi b}} d\xi \\ &= |a|^{\frac{1}{2}} \int_{-\infty}^{\infty} F(\xi) \overline{\Psi(a\xi)} e^{i2\pi\xi b} d\xi \end{aligned} \tag{3.8}$$

The right side of (3.8) is the Inverse Fourier Transform of $F(\xi)\overline{\Psi(a\xi)}$, so taking the Fourier Transform of both sides with respect to b gives

$$\int_{-\infty}^{\infty} W_f(a,b) e^{-i2\pi\xi b} db = |a|^{\frac{1}{2}} F(\xi) \overline{\Psi(a\xi)} \tag{3.9}$$

Kaiser uses some clever manipulation to isolate $F(\xi)$ in (3.9). He multiplies both sides by $|a|^{\frac{1}{2}} \Psi(a\xi)$ and integrates with respect to a where the measure of integration is $da/|a|^2$

$$\begin{aligned} \int_{-\infty}^{\infty} \int_{-\infty}^{\infty} W_f(a,b) |a|^{\frac{1}{2}} \Psi(a\xi) e^{-i2\pi\xi b} \frac{dadb}{|a|^2} &= \int_{-\infty}^{\infty} F(\xi) |\Psi(a\xi)|^2 \frac{da}{|a|} \\ &= F(\xi) \int_{-\infty}^{\infty} |\Psi(a\xi)|^2 \frac{da}{|a|} \\ &= F(\xi) Z(\xi) \end{aligned} \tag{3.10}$$

where

$$Z(\xi) = \int_{-\infty}^{\infty} |\Psi(a\xi)|^2 \frac{da}{|a|}. \tag{3.11}$$

Choosing $da/|a|^2$ as the measure associated with the integral in (3.10) guarantees that the admissibility condition is a constant and therefore guarantees that the dual can be represented as a shifted and dilated version of a mother wavelet [19]. Now $F(\xi)$ in (3.10) can be solved if and only if $0 < A < Z^{-1}(\xi) < B < \infty$,

$$F(\xi) = Z^{-1}(\xi) \int_0^{\infty} \int_{-\infty}^{\infty} W_f(a,b) |a|^{\frac{1}{2}} \Psi(a\xi) e^{-i2\pi\xi b} \frac{dadb}{|a|^2}. \tag{3.12}$$

Substituting $\omega = a\xi$ in (3.11) gives the admissibility condition, which is a constant and therefore bounded,

$$Z(\xi) = C_\psi = \int_{-\infty}^{\infty} \frac{|\Psi(\omega)|^2}{|\omega|} d\omega \tag{3.13}$$

Substituting $Z(\xi) = C_\psi$ in (3.12) and taking the Inverse Fourier Transform of both sides with respect to ξ gives

$$f(x) = \frac{1}{C_\psi} \int_{-\infty}^{\infty} \int_{-\infty}^{\infty} W_f(a,b)|a|^{-\frac{1}{2}} \psi\left(\frac{x-b}{a}\right) \frac{dadb}{|a|^2} \tag{3.14}$$

which is the form of the Inverse Wavelet Transform given in Theorem 2.

Figure 3.2 shows an example of a continuous wavelet transform. The signal being analyzed is a transient sinusoid with exponentially decaying amplitude. The analyzing wavelet is Morlet's wavelet from Figure 3.1. The horizontal axis is shift, b, and the vertical axis is scale, a with a increasing downward.

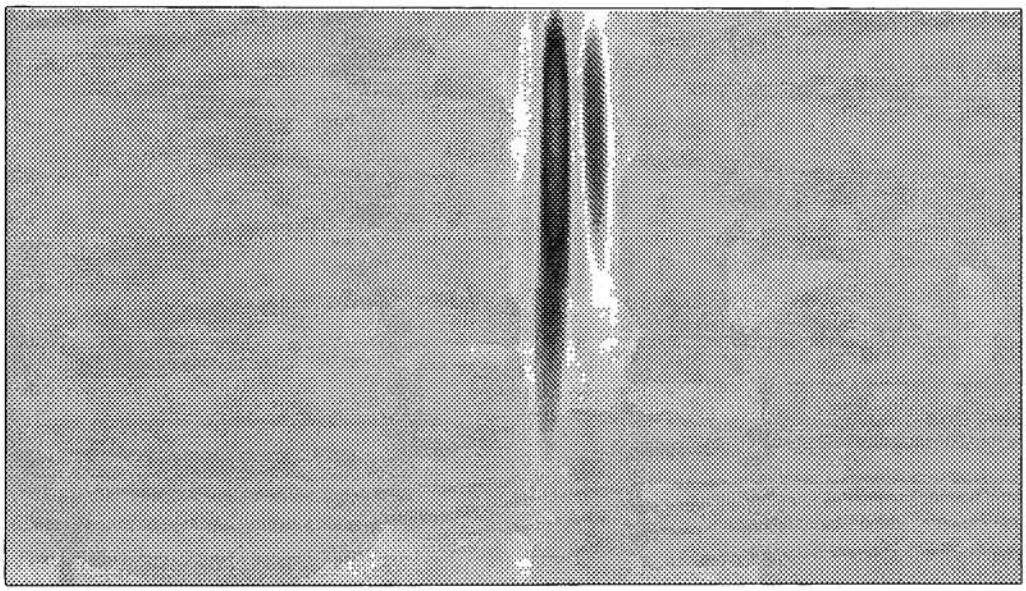

Figure 3.2: Continuous Wavelet Transform of a transient signal

The transient signal has an average value of 0, so for large values of a, the CWT vanishes since a very wide wavelet tends to average over the transient signal. The CWT also vanishes for very small values of a since the signal appears constant over a very short interval. There is a value of a, however, that coincides very nicely with the oscillation of the transient signal, thereby producing a very large response in the CWT, which can be seen in Figure 3.2. The time localization feature of the CWT, provided through

the shift parameter, b, gives the approximate location of the transient signal.

The continuous wavelet transform, characterized by $a, b \in \Re$, where $a \neq 0$, is rather simple to use and requires very few restrictions on the analyzing wavelet. However, it contains a lot of redundancy and is computationally intensive. Notice in Figure 3.2 the high degree of correlation in the CWT. This correlation is due to the redundancy and can be removed by less redundant representations. The following sections will show the development of different classes of wavelets with lesser degrees of redundancy as a and b are further constrained. While these constraints add conditions on the wavelets, they lead to the generation of bases, new design techniques, and fast algorithms for the wavelet transform.

3.2 Dyadic Wavelets

In order to reduce the computational burden of the CWT, let the scale parameter take on values of $a = 2^j$ where $j \in \mathbb{Z}$ and $b \in \Re$. The wavelet transform becomes

$$\begin{aligned} W_f(2^j, b) &= \langle f, \psi_{2^j,b} \rangle \\ &= \int_{-\infty}^{\infty} f(x)\ 2^{-\frac{j}{2}} \psi(2^{-j}x - b2^{-j}) dx \end{aligned} \tag{3.15}$$

This class of wavelets is known as "dyadic" wavelets and are defined as follows:

Definition 4 (Dyadic Wavelets) *[10] A function $\psi \in L^2(\Re)$ is called a dyadic wavelet if there exist two positive constants A and B, with $0 < A \leq B < \infty$, such that*

$$A \leq \sum_{j=-\infty}^{\infty} \left|\Psi\left(2^{-j}\omega\right)\right|^2 \leq B. \tag{3.16}$$

Condition (3.16) is known as the stability condition and again is driven by the necessity for an inverse transform. Since (3.15) has the same form as the CWT, but with $a = 2^j$, then (3.11) must still hold where $a = 2^j$. Substituting $\Delta a = 2^{j+1} - 2^j = 2^j$ for da gives $da/a = 1$. Summing over j gives

$$Z(\xi) = \sum_{j \in \mathbf{Z}} \left|\Psi\left(2^j \xi\right)\right|^2 \tag{3.17}$$

As before, $Z(\xi)$ must be bounded, which leads to the stability condition

$$0 < A < \sum_{j \in \mathbf{Z}} \left|\Psi\left(2^j \xi\right)\right|^2 < B < \infty. \tag{3.18}$$

Notice this time that $Z(\xi)$ must not necessarily be a constant. However, since it is bounded, the Inverse Wavelet Transform can be found by substituting $a = 2^j$ and $\Delta a = 2^j$ into (3.12) and summing over j instead of integrating over a,

$$\begin{aligned} F(\xi) &= \sum_{j\in\boldsymbol{Z}} \int_{-\infty}^{\infty} Z^{-1}(\xi) W_f(2^j, b) 2^{\frac{j}{2}} \Psi(2^j\xi) e^{-i2\pi\xi b} \frac{db}{2^j} \\ &= \sum_{j\in\boldsymbol{Z}} \int_{-\infty}^{\infty} 2^{-j} W_f(2^j, b) 2^{\frac{j}{2}} \tilde{\Psi}(2^j\xi) e^{-i2\pi\xi b} \frac{db}{2^j} \end{aligned} \tag{3.19}$$

where $\tilde{\Psi}(\xi) = \Psi(\xi)/Z(\xi)$ and $Z(\xi)$ is given in (3.17). Taking the Inverse Fourier Transform of both sides of (3.19) gives the expression for the Inverse Wavelet Transform using dyadic wavelets,

$$f(x) = \sum_{j\in\boldsymbol{Z}} \int_{-\infty}^{\infty} 2^{-j} W_f(2^j, b) 2^{-\frac{j}{2}} \tilde{\psi}\left(\frac{x-b}{2^j}\right) db \tag{3.20}$$

where $\tilde{\psi}(x)$ is the Inverse Fourier Transform of $\tilde{\Psi}(\xi)$ and is the dual wavelet to $\psi(x)$.

3.3 Frames

The next step in reducing the computational burden of the CWT is to sample the shift parameter, letting $b_{j,k} = k2^j b_0$, where b_0 is a constant known as the sampling rate [10]. Now the wavelet operator is given as

$$\psi_{b_0;j,k}(x) = 2^{-\frac{1}{2}} \psi(2^{-j}x - kb_0) \tag{3.21}$$

and the wavelet transform given by

$$W_f(a_j, b_{j,k}) = \langle f, \psi_{b_0;j,k} \rangle \tag{3.22}$$

The condition on the wavelet also tightens beyond the stability condition, namely,

$$A\|f\|^2 \leq \sum_{j,k\in\boldsymbol{Z}} |\langle f, \psi_{b_0;j,k}\rangle|^2 \leq B\|f\|^2 \tag{3.23}$$

where $\|\cdot\|^2$ is the $L^2(\Re)$ norm and $0 < A \leq B < \infty$. This condition is identical to that for a frame of $L^2(\Re)$, meaning that in order for ψ to be a wavelet with the stated conditions on a and b, it must generate a frame of $L^2(\Re)$ [10].

Definition 5 (Frames of $L^2(\Re)$) *[10] A function $\psi \in L^2(\Re)$ is said to generate a frame $\{\psi_{b_0;j,k}\}$ of $L^2(\Re)$ with sampling rate $b_0 > 0$ if (3.23) holds for some positive constants A and B, which are called frame bounds. If $A = B$, then the frame is called a tight frame.*

Before giving the expression for the inverse transform, let T be a linear operator on $L^2(\Re)$, defined by

$$Tf = \sum_{j,k \in \mathbf{Z}} \langle f, \psi_{b_0;j,k} \rangle \psi_{b_0;j,k} \tag{3.24}$$

where $f \in L^2(\Re)$. Then the dual of $\psi_{b_0;j,k}$ is given by $\psi_{b_0}^{j,k} = T^{-1}\psi_{b_0;j,k}$ and the inverse wavelet transform by

$$f(x) = \sum_{j,k \in \mathbf{Z}} \langle f, \psi_{b_0;j,k} \rangle \psi_{j,k}^{b_0} \tag{3.25}$$

If $A = B = 1$, then $\psi_{b_0;j,k}$ is an orthonormal basis of $L^2(\Re)$. If $A = B \neq 1$, then the frame is called a tight frame, which acts like an orthonormal basis, but may not even be linearly independent [12]. The intent of discretizing both the scale and shift parameters is to reduce the redundancy of the wavelet transform. Frames provide an intermediate step between the continuous wavelet transform, which contains the maximum amount of redundancy, and wavelet orthonormal bases, which generate decompositions with no redundancy. The ratio of the frame bounds, B/A, acts like a redundancy indicator. For instance, in speech processing, B/A is very large indicating a lot of redundancy in the wavelet transform and in fact approximates the continuous wavelet transform [12]. At the other extreme, applications like image compression, requiring no redundancy, constrain the wavelets so that they generate a tight frame, that is, $B/A = 1$.

A. Grossman with the help of Y. Meyer first realized the importance of the frame concept with regards to wavelet analysis. Meyer showed how the wavelet frame construction was the same as that of the Weyl-Heisenberg coherent states. However, for the W-H coherent states, if a basis, g, was required (no redundancy) as opposed to a frame, then either $xg(x)$ or $\omega G(\omega)$ was not square integrable (not in $L^2(\Re)$)[12]. Meyer set out to show that Grossman's wavelet frames were subject to the same limitation, but instead discovered a bandlimited, orthonormal wavelet basis such that $x\psi(x)$ and $\omega\Psi(\omega)$ were both in $L^2(\Re)$ [13]. This discovery led many of the wavelet pioneers toward developing the mathematics for orthonormal wavelet bases.

3.4 Orthonormal Wavelets

Y. Meyer showed that for $a = 2^j$ and $b = k2^j$ (assume $b_0 = 1$), there exists a family of functions, $\{\psi_{j,k} = 2^{-j/2}\psi(2^{-j}x - k)\}$ that form an orthonormal basis of $L^2(\Re)$. Chui and Mallat define an orthonormal wavelet basis as follows.

Definition 6 (Orthonormal Wavelet Bases) *[10, 23, 27] A function $\psi \in L^2(\Re)$ is called an orthonormal wavelet if the family $\{\psi_{j,k}\}$, is an orthonormal basis of $L^2(\Re)$, that is,*

$$\langle \psi_{j,k}, \psi_{l,m} \rangle = \delta_{j,l} \cdot \delta_{k,m} \tag{3.26}$$

where

$$\delta_{j,k} = \begin{cases} 1 & for\ j = k \\ 0 & j \neq k \end{cases} \tag{3.27}$$

and every $f \in L^2(\Re)$ can be written as

$$f(x) = \sum_{j=-\infty}^{\infty} \sum_{k=-\infty}^{\infty} d_k^j 2^{\frac{j}{2}} \psi(2^j x - k) \tag{3.28}$$

Equation (3.26) indicates that the family of wavelets, $\psi_{j,k}$ is orthogonal in two dimensions. Integer translates of the wavelet at a given scale are orthogonal to one another ($\delta_{k,m}$) as are wavelets at two different scales ($\delta_{j,l}$). At a given scale, j, $\langle \psi_{j,k}, \psi_{j,m} \rangle = \delta_{k,m}$ and $\psi_{j,k}$ forms an orthonormal basis of W_j, a subspace of $L^2(\Re)$. Because of orthogonality across scales, $W_j \perp W_l$ for all $j \neq l$. Therefore, applying (2.13) to the projection of f onto W_j gives

$$g^j(x) = (\mathcal{Q}_\psi^j f)(x) = \sum_{k=-\infty}^{\infty} d_k^j 2^{\frac{j}{2}} \psi(2^j x - k) \tag{3.29}$$

where $g^j(x) \in W_j$ and

$$d_k^j = \langle f, \psi_{j,k} \rangle = \int_{-\infty}^{\infty} f(x) 2^{\frac{j}{2}} \overline{\psi(2^j x - k)} dx \tag{3.30}$$

$\mathcal{Q}_\psi^j$ is the projection operator with respect to the basis ψ. Substituting (3.29) into (3.28) gives

$$f(x) = \sum_{j=-\infty}^{\infty} (\mathcal{Q}_\psi^j f)(x) \tag{3.31}$$

which says that f can be decomposed into an infinite sum of its projections onto orthogonal subspaces, W_j [10]. Furthermore, $L^2(\Re)$ can be expressed as the direct sum of orthogonal subspaces W_j

$$L^2(\Re) = \ldots \dot{+} W_{-1} \dot{+} W_0 \dot{+} W_1 \dot{+} \ldots \tag{3.32}$$

Because the wavelet has the characteristic of a bandpass filter (3.4), the projection operator, $\mathcal{Q}_\psi^j$, is effectively projecting or filtering out the detail or high frequency content of f at scale j, and (3.31) shows that f consists of the infinite sum of these detail functions, $(\mathcal{Q}_\psi^j f)(x)$ [10, 12, 23, 27]. Furthermore, the detail functions $(\mathcal{Q}_\psi^j f)(x)$, contained in W_j, are orthogonal to one another since $W_j \perp W_l$ for all $j \neq l$.

3.5 Multiresolution Analysis

A major breakthrough in the understanding of orthonormal wavelet bases came when Y. Meyer and S. Mallat imposed the concept of multiresolution analysis on wavelet decompositions [14]. Mallat had been working with the Laplacian pyramid algorithm developed by Burt and Adelson [6] and recognized that the sequence of functions generated by an orthonormal wavelet were in essence "detail" functions that representated the information lost in going from one scale to a lower scale [13]. He and Y. Meyer developed the mathematics for what came to be known as a multiresolution analysis.

Let V_j be defined as a subspace of $L^2(\Re)$ where

$$V_j = \ldots \dot{+} W_{j-3} \dot{+} W_{j-2} \dot{+} W_{j-1} \tag{3.33}$$

Then, the direct sum decomposition of $L^2(\Re)$ in (3.32) can be rewritten [10, 23] as

$$L^2(\Re) = V_j \dot{+} W_j \dot{+} W_{j+1} \dot{+} \ldots \tag{3.34}$$

From (3.33), it is clear that

$$V_{j+1} = V_j \dot{+} W_j \tag{3.35}$$

and V_j forms a nested sequence of subspaces of $L^2(\Re)$, that is,

$$\ldots V_{j-1} \subset V_j \subset V_{j+1} \ldots \tag{3.36}$$

Let $\phi_{j,k}$ be a set of functions that spans the subspace V_j [10], where

$$\phi_{j,k} = 2^{\frac{j}{2}}\phi(2^j x - k) \tag{3.37}$$

Then, any function in V_j can be represented by a linear combination of $\phi_{j,k}$.

$$f^j(x) = \sum_{k=-\infty}^{\infty} c_k^j 2^{\frac{j}{2}}\phi(2^j x - k) \tag{3.38}$$

Assume $\phi_{j,k}$ forms an orthonormal basis of V_j, then

$$\langle \phi_{j,k}, \phi_{j,m} \rangle = \delta_{k,m} \tag{3.39}$$

and,

$$c_k^j = \langle f^j(x), \phi_{j,k} \rangle \tag{3.40}$$

This assumption is not as bold as it may seem. The Fourier transform of (3.39), called the Poisson summation, is a 2π periodic function given by

$$\sum_{k=-\infty}^{\infty} |\Phi(\omega + 2\pi k)|^2 = 1 \tag{3.41}$$

where $\Phi(\omega)$ is the Fourier transform of $\phi(x)$. Let $\hat{\phi}(x)$ be a function such that $\hat{\phi}_{j,k}$ spans V_j, then $\phi_\perp(x)$ can be found such that it satisfies (3.39) by way of the following orthogonalizing "trick" and taking the inverse Fourier transform [10]:

$$\Phi_\perp(\omega) = \frac{\hat{\Phi}(\omega)}{\left(\sum_{k=-\infty}^{\infty} |\Phi(\omega + 2\pi k)|^2\right)^{\frac{1}{2}}} \tag{3.42}$$

where $0 < A \leq |\sum_{k=-\infty}^{\infty} |\Phi(\omega + 2\pi k)|^2 \leq B < \infty$ for all ω. Because a non-orthogonal function that spans V_j can be orthogonalized using (3.42), it is safe to assume that $\phi_{j,k}$ is orthonormal in the first place.

Now, if f^j is a function in the subspace V_j, then by (3.35) it can be represented by the sum of its projections on W_{j-1} and V_{j-1} [10, 12]

$$f^j(x) = \mathcal{P}_\phi^{j-1}(f^j)(x) + \mathcal{Q}_\psi^{j-1}(f^j)(x) \tag{3.43}$$

Since $\mathcal{Q}_{\psi}^{j-1}(f)$ represents the detail of f^j at scale $j-1$, then $\mathcal{P}_{\phi}^{j-1}(f)$ must represent f^j with those details removed, that is, a lower resolution approximation of f^j at scale $j-1$ [10, 12, 23]. Subsequent projections onto complement subspaces, V and W, produce the decomposition map shown in Figure 3.3. V_j contains lower and lower resolution approximations of f^j as $j \rightarrow -\infty$. The nested sequence of

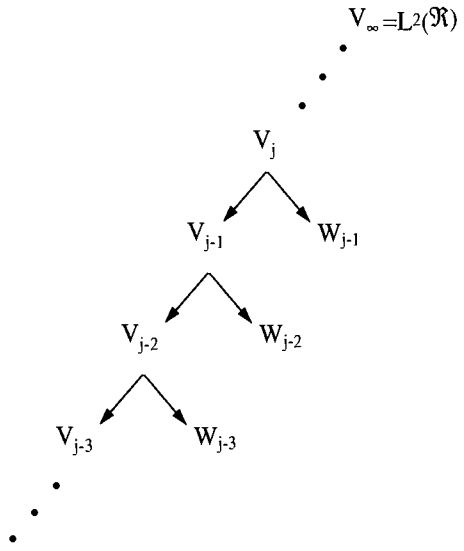

Figure 3.3: Multiresolution Decomposition of $L^2(\Re)$

subspaces is called a multiresolution analysis and satisfies the following conditions:

Definition 7 Multiresolution Analysis*[10, 12, 23, 24, 27]*

The sequence of subspaces, V_j, form a multiresolution analysis if the following conditions are satisfied:

1. $\ldots \subset V_{-1} \subset V_0 \subset V_1 \ldots$;
2. $clos_{L^2}\left(\bigcup_{j\in Z} V_j\right) = L^2(\Re)$;
3. $\bigcap_{j\in Z} V_j = \{0\}$;
4. $V_{j+1} = V_j \dot{+} W_j, j \in Z$; *and*

5. $f(x) \in V_j \Leftrightarrow f(2x) \in V_{j+1}, j \in Z$

Items 7.1 and 7.2 state that a multiresolution analysis is a nested sequence of subspaces whose union spans $L^2(\Re)$. Item 7.3 states that there is no portion of $L^2(\Re)$ that is common to all subspaces V_j, except the all zero function, $\{0\}$. Item 7.4 states that a subspace, V_j consists of the sum of the subspace V_{j-1} and its complement W_{j-1}. Finally, Item 7.5 states that if a function, f, resides in the subspace at scale j, then f dilated by 2 resides in the subspace at scale $j+1$, which can be seen easily in (3.43) by letting $x' = 2x$.

An orthonormal multiresolution analysis (MRA) [10, 12, 23, 24, 27] further requires that the two complementary subspaces, V_j and W_j be orthogonal complements, $V_j \perp W_j$, which leads to the following condition on their bases

$$\langle \phi_{j,k}, \psi_{j,l} \rangle = 0 \tag{3.44}$$

Let f^{j+1} be some function that can be completely represented by the orthonormal basis of V_{j+1}, that is, $f^{j+1}(x) \in V_{j+1}$. From (3.43), f^{j+1} can be decomposed into a detail function and low resolution approximation at scale j [10, 12, 23], that is,

$$f^{j+1}(x) = \mathcal{P}_\phi^j(f^{j+1})(x) + \mathcal{Q}_\psi^j(f^{j+1})(x) \tag{3.45}$$

$$= f^j(x) + g^j(x) \tag{3.46}$$

where f^j and g^j reside in orthogonal subspaces, V_j and W_j. In a MRA, $f^j(x)$ can be decomposed again into orthogonal subspaces, V_{j-1} and W_{j-1},

$$f^j(x) = \mathcal{P}_\phi^{j-1}(f^j)(x) + \mathcal{Q}_\psi^{j-1}(f^j)(x) \tag{3.47}$$

$$= f^{j-1}(x) + g^{j-1}(x) \tag{3.48}$$

Substituting (3.48) into (3.46) gives a two level decomposition of $f^{j+1}(x)$

$$f^{j+1}(x) = f^{j-1}(x) + g^{j-1}(x) + g^j(x) \tag{3.49}$$

The N-level decomposition of $f^j(x)$ is given as

$$f^{j+1}(x) = f^{j+1-N}(x) + \sum_{i=1}^{N} g^{j-i+1}(x) \tag{3.50}$$

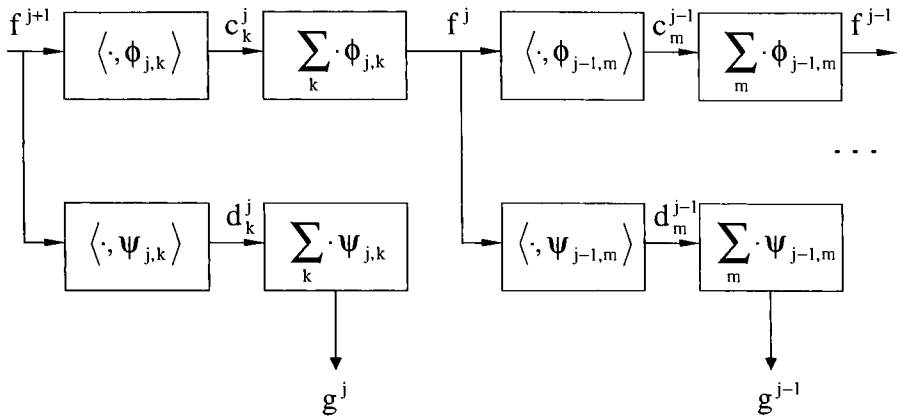

Figure 3.4: N-level Multiresolution Decomposition

and is shown in Figure 3.4. It is helpful to visualize what a multiresolution decomposition looks like by looking at an example. Let the wavelet be Daubechies' D4 wavelet, a known orthonormal wavelet, shown in Figure 3.5 with its corresponding scaling function. Daubechies' technique for deriving these

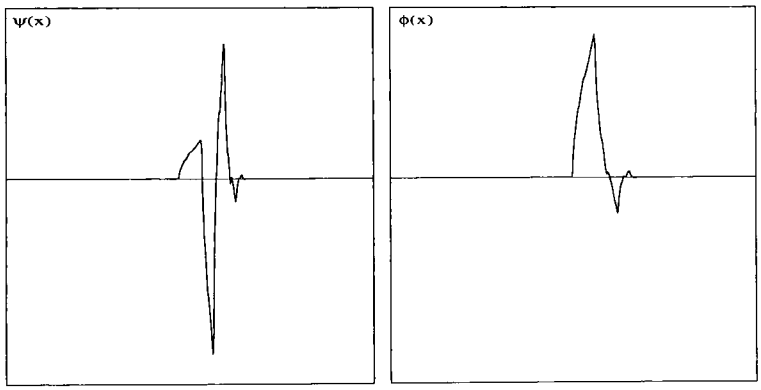

Figure 3.5: Daubechies' D4 Wavelet and Scaling Function

wavelets will be discussed in more detail in Chapter 4. Figure 3.6 shows the multiresolution decomposition of a transient signal using the D4 wavelet and corresponding scaling function. The functions on the left are the successive low resolution approximations of the transient signal at each scale. The functions on the right are the detail functions found by projecting the signal onto the orthonormal wavelet basis

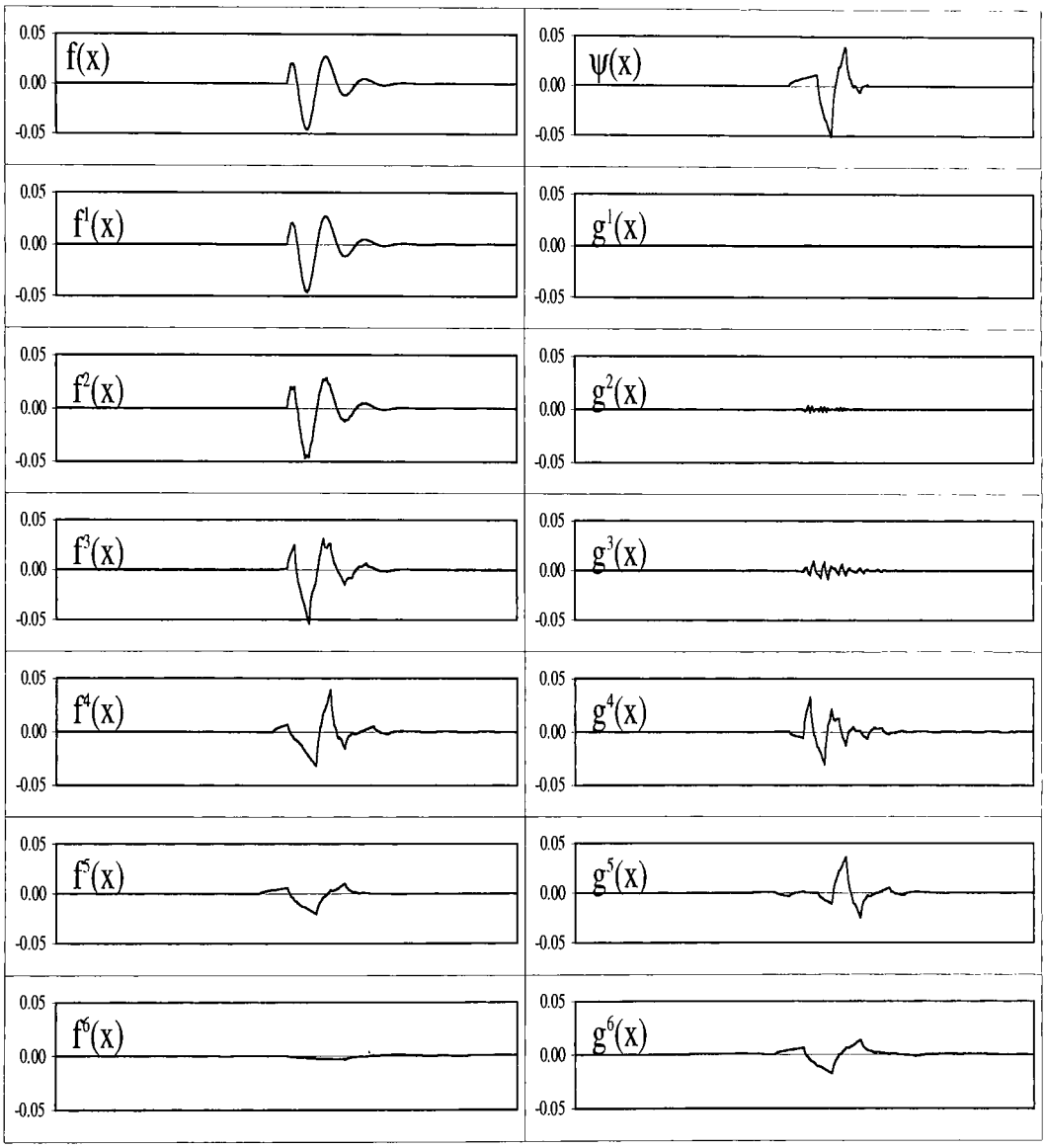

Figure 3.6: Multiresolution Decomposition Example using the D4 wavelet

for that scale. The basis is constructed by integer shifts of the wavelet dilated by 2^j. Notice the effect of projection. As the signal is projected into lower and lower scales, both the approximation and detail functions begin to look like the scaling function and wavelet, respectively, which is expected since each is a linear combination of the basis functions of each subspace, V and W. This effect is one reason why one might desire a wavelet basis that "looks" like the signal being analyzed. The original signal in Figure 3.6 is completely represented by the detail functions and the last low resolution approximation and can be reconstructed simply by summation.

As mentioned previously, the constraints on the wavelet increase in complexity as one moves from the integral wavelet transform to orthonormal bases. It is important to understand those constraints, since they will be used extensively in the wavelet design algorithm presented in Chapter 5.

3.5.1 Properties of ϕ and ψ

As shown previously, in an orthonormal multiresolution, $\{V_j\}$, $\phi_{j,k}$ is an orthonormal basis of the subspace V_j, and $\psi_{j,k}$ is an orthonormal basis of the subspace W_j, where $V_j \perp W_j$. Furthermore, the family of functions $\{\psi_{j,k}; -\infty < j < \infty\}$ is an orthonormal basis of $L^2(\Re)$. These conditions lead to the following relationships between $\phi_{j,k}$ and $\psi_{j,k}$ [10]

$$\langle \phi_{j,k}, \phi_{j,l} \rangle = \delta_{k,l} \tag{3.51}$$

$$\langle \phi_{j,k}, \psi_{j,l} \rangle = 0 \tag{3.52}$$

$$\langle \psi_{j,k}, \psi_{l,m} \rangle = \delta_{j,l} \cdot \delta_{k,m} \tag{3.53}$$

as given previously in (3.39) (3.44) and (3.26). Furthermore, since $\psi(x)$ is a wavelet, then by (3.4)

$$\int_{-\infty}^{\infty} \psi(x)dx = 0 \qquad \stackrel{\mathcal{F}}{\Longleftrightarrow} \qquad \Psi(0) = 0 \tag{3.54}$$

By (3.35) it is clear that since $\phi_{j,k}$ and $\psi_{j,k}$ are bases of $V_j \in V_{j+1}$ and $W_j \in V_{j+1}$, respectively, they both reside in V_{j+1} and can therefore be represented by a linear combination of the basis of V_{j+1} [10, 12, 23, 31]. For $j = 0$, $\phi_{0,0} = \phi(x) \in V_1$ can be represented using (3.38) as:

$$\phi(x) = \sum_{k=-\infty}^{\infty} c_k 2^{\frac{1}{2}} \phi(2x - k) \tag{3.55}$$

Since $\psi(x)$ also resides in V_1, (3.38) gives the generating equation for the wavelet

$$\psi(x) = \sum_{k=-\infty}^{\infty} b_k 2^{\frac{1}{2}} \phi(2x-k). \tag{3.56}$$

The $2^{1/2}$ term in both of the above equations can be included in the coefficients giving

$$\phi(x) = \sum_{k=-\infty}^{\infty} p_k \phi(2x-k) \tag{3.57}$$

and

$$\psi(x) = \sum_{k=-\infty}^{\infty} q_k \phi(2x-k) \tag{3.58}$$

Equation (3.57) is a recursive equation called the *two scale relation* for ϕ, and p_k and q_k are called the *generating sequences* for ϕ and ψ, respectively [10]. Taking the Fourier Transform of (3.57) and (3.58) gives the relationship between $\Phi(\omega)$, $\Psi(\omega)$, $P(\omega)$, and $Q(\omega)$.

$$\Phi(\omega) = \frac{1}{2} P\left(\frac{\omega}{2}\right) \Phi\left(\frac{\omega}{2}\right) \tag{3.59}$$

$$\Psi(\omega) = \frac{1}{2} Q\left(\frac{\omega}{2}\right) \Phi\left(\frac{\omega}{2}\right) \tag{3.60}$$

Assume $\phi(x)$, called the scaling function [10, 12, 23, 24, 27], generates the multiresolution analysis, $\{V_j\}$, and is normalized [31] such that

$$\int_{-\infty}^{\infty} \phi(x)dx = 1 \qquad \stackrel{\mathcal{F}}{\Longleftrightarrow} \qquad \Phi(0) = 1 \tag{3.61}$$

Since $\phi(x+n)$ and $\psi(x+n)$ form orthonormal bases of V_0 and W_0, respectively, and are orthogonal to one another, then the following must be true

$$\int_{-\infty}^{\infty} |\phi(x)|^2 dx = 1 \tag{3.62}$$

$$\int_{-\infty}^{\infty} |\psi(x)|^2 dx = 1 \tag{3.63}$$

$$\int_{-\infty}^{\infty} \phi(x)\phi(x+n)dx = \delta(n) \tag{3.64}$$

$$\int_{-\infty}^{\infty} \psi(x)\psi(x+n)dx = \delta(n) \tag{3.65}$$

$$\int_{-\infty}^{\infty} \phi(x)\psi(x+n)dx = 0 \tag{3.66}$$

Taking the Fourier Transform of (3.64) gives the Poisson Summation on $\Phi(\omega)$ [23, 24]

$$\begin{aligned}
\mathcal{F}\left(\int_{-\infty}^{\infty}\phi(x)\phi(x+n)dx\right) &= \mathcal{F}(\delta(n)) \\
\mathcal{F}\left([\phi(x)\star\phi(x)]\cdot\sum_{n=-\infty}^{\infty}\delta(x+n)\right) &= 1 \\
|\Phi(\omega)|^2 * \sum_{n=-\infty}^{\infty}\delta(\omega+2\pi n) &= 1 \\
\sum_{n=-\infty}^{\infty}|\Phi(\omega+2\pi n)|^2 &= 1
\end{aligned} \tag{3.67}$$

where "$\star$" is the correlation operator and "$*$" is the convolution operator. Likewise, taking the Fourier Transform of (3.65) gives the Poisson Summation on $\Psi(\omega)$.

$$\sum_{n=-\infty}^{\infty}|\Psi(\omega+2\pi n)|^2 = 1 \tag{3.68}$$

Substituting (3.57) and (3.58) into (3.4) and (3.61)-(3.66) produces several conditions on p_k and q_k [10, 12]

$$\sum_{k=-\infty}^{\infty}p_k = 2 \quad \overset{\mathcal{F}}{\Longleftrightarrow} \quad P(0) = 2 \tag{3.69}$$

$$\sum_{k=-\infty}^{\infty}q_k = 0 \quad \overset{\mathcal{F}}{\Longleftrightarrow} \quad Q(0) = 0 \tag{3.70}$$

$$\sum_{k=-\infty}^{\infty}p_k^2 = 2 \tag{3.71}$$

$$\sum_{k=-\infty}^{\infty}q_k^2 = 2 \tag{3.72}$$

$$\sum_{k=-\infty}^{\infty}p_k p_{k-2n} = 2\delta(n) \tag{3.73}$$

$$\sum_{k=-\infty}^{\infty}q_k q_{k-2n} = 2\delta(n) \tag{3.74}$$

$$\sum_{k=-\infty}^{\infty}p_k q_{k-2n} = 0. \tag{3.75}$$

Two additional conditions on $P(\omega)$ and $Q(\omega)$ are stated here without proof or explanation. The details are provided in Section 3.6.

$$|P(\omega)|^2 + |Q(\omega)|^2 = 4 \tag{3.76}$$

$$P(\omega)\overline{P(\omega+\pi)} + Q(\omega)\overline{Q(\omega+\pi)} = 0 \tag{3.77}$$

Conditions (3.76) and (3.77) allow for perfect reconstruction of the decomposition of f.

It is important to note that the scaling function, $\phi(x)$, generates the multiresolution analysis, $\{V_j\}$ and the wavelet, $\psi(x)$, generates the multiresolution decomposition, $\{g^j(x)\}$. Before the MRA was formulated by Meyer and Mallat, there was no standard technique for finding orthonormal wavelet bases. Through the scaling function, however, several design techniques were developed and they will be discussed in Chapter 4. Furthermore, because the scaling function is the MRA generator, the conditions for an orthonormal MRA rest on the scaling function as will be shown in Chapter 5.

3.6 Discrete Wavelet Transform

The purpose for moving from the continuous wavelet transform (CWT) to frames and ultimately to orthonormal bases was to remove the redundancy in the wavelet transform. Multiresolution analyses summarized in Section 3.5 provide the framework for finding orthonormal bases of $L^2(\Re)$, but are still based on continuous functions. That is, the orthogonal multiresolution decomposition given in (3.50) starts with a continuous function and decomposes it into a series of detail functions and a final low resolution residual. However, each detail and low resolution function can be uniquely defined by its corresponding projection coefficients, c_k^j and d_k^j at some scale j, as shown in (3.29), (3.38) and Figure 3.4. In some digital signal and image processing applications, like compression, one would like to deal with the coefficients only and never have to produce the continuous detail or low resolution functions. Mallat [24] used his MRA construction to develop a fast algorithm for finding the multiresolution decomposition of a signal. In Figure 3.4, let $f^{j+1} = f$, then

$$\begin{aligned} c_m^{j-1} &= \langle \mathcal{P}_\phi^j f, \phi_{j-1,m} \rangle \\ &= \langle \sum_{k=-\infty}^{\infty} c_k^j \phi_{j,k}, \phi_{j-1,m} \rangle \\ &= \sum_{k=-\infty}^{\infty} c_k^j \langle \phi_{j,k}, \phi_{j-1,m} \rangle \end{aligned} \tag{3.78}$$

and likewise,

$$d_m^{j-1} = \sum_{k=-\infty}^{\infty} c_k^j \langle \phi_{j,k}, \psi_{j-1,m} \rangle \tag{3.79}$$

Through a change in variables and some algebra it can be shown [10, 12, 23] that

$$\langle \phi_{j,k}, \phi_{j-1,m} \rangle = 2^{-\frac{1}{2}} \int_{-\infty}^{\infty} \phi(\frac{1}{2}x)\phi(x-(k-2m))dx \tag{3.80}$$

Notice that the inner product of two scaling functions from adjacent scales is not a function of their scales at all! The scale parameter, j, does not appear in the right side of (3.80). Similarly,

$$\langle \phi_{j,k}, \psi_{j-1,m} \rangle = 2^{-\frac{1}{2}} \int_{-\infty}^{\infty} \psi(\frac{1}{2}x)\phi(x-(k-2m))dx \tag{3.81}$$

Let

$$h_n = 2^{-1} \int_{-\infty}^{\infty} \phi(\frac{1}{2}x)\phi(x-n)dx \tag{3.82}$$

and

$$g_n = 2^{-1} \int_{-\infty}^{\infty} \psi(\frac{1}{2}x)\phi(x-n)dx \tag{3.83}$$

then (3.78) and (3.79) become

$$c_m^{j-1} = \sum_{k=-\infty}^{\infty} c_k^j h_{k-2m} \tag{3.84}$$

and

$$d_m^{j-1} = \sum_{k=-\infty}^{\infty} c_k^j g_{k-2m} \tag{3.85}$$

where the remaining $2^{-1/2}$ term is included in c_k^j. Equations (3.84) and (3.85) show that the projection coefficients for the low resolution and detail functions can be obtained by filtering and downsampling the low resolution projection coefficients from the previous scale. Furthermore, the digital filters used are the same regardless of which scale is being decomposed. Equations (3.84) and (3.85) are known as the Discrete Wavelet Transform. [10, 12, 23, 30] The multiresolution decomposition shown in Figure 3.4 can be represented by a sequence of Discrete Wavelet Transforms (Figure 3.7) [23]. Substituting (3.57) and (3.58) into (3.82) and (3.83), respectively, gives

$$h_n = \frac{1}{2} p_n \tag{3.86}$$

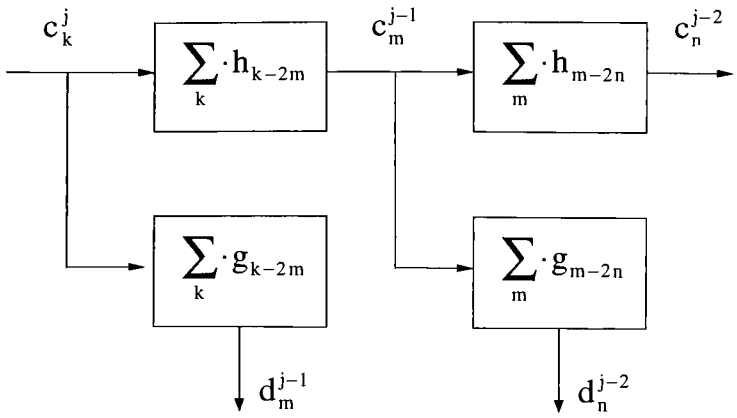

Figure 3.7: Discrete Wavelet Transform

$$g_n = \frac{1}{2} q_n. \tag{3.87}$$

So, except for a constant scale factor, the digital filters, h_n and g_n, used to implement the Discrete Wavelet Transform are precisely the generating sequences for $\phi(x)$ and $\psi(x)$, respectively [12]. Given this relationship and the fact that for digital signals, one would like to deal with only the projection coefficients and the digital filters, as in (3.84) and (3.85), the conditions on p and q in (3.59), (3.60), (3.69), (3.70), and (3.71)-(3.77) can be translated directly to conditions on h and g.

$$\phi(x) = 2 \sum_{k=-\infty}^{\infty} h_k \phi(2x - k) \tag{3.88}$$

$$\psi(x) = 2 \sum_{k=-\infty}^{\infty} g_k \phi(2x - k) \tag{3.89}$$

$$\Phi(\omega) = H\left(\frac{\omega}{2}\right) \Phi\left(\frac{\omega}{2}\right) \tag{3.90}$$

$$\Psi(\omega) = G\left(\frac{\omega}{2}\right) \Phi\left(\frac{\omega}{2}\right) \tag{3.91}$$

$$\sum_{k=-\infty}^{\infty} h_k = 1 \tag{3.92}$$

$$\sum_{k=-\infty}^{\infty} g_k = 0 \tag{3.93}$$

$$\sum_{k=-\infty}^{\infty} h_k^2 = \frac{1}{2} \tag{3.94}$$

$$\sum_{k=-\infty}^{\infty} g_k^2 = \frac{1}{2} \tag{3.95}$$

$$\sum_{k=-\infty}^{\infty} h_k h_{k-2n} = \frac{1}{2}\delta(n) \tag{3.96}$$

$$\sum_{k=-\infty}^{\infty} g_k g_{k-2n} = \frac{1}{2}\delta(n) \tag{3.97}$$

$$\sum_{k=-\infty}^{\infty} h_k g_{k-2n} = 0 \tag{3.98}$$

$$|H(\omega)|^2 + |G(\omega)|^2 = 1 \tag{3.99}$$

$$H(\omega)\overline{H(\omega+\pi)} + G(\omega)\overline{G(\omega+\pi)} = 0 \tag{3.100}$$

From (3.92) and (3.93) it can be shown that h_k and g_k are low pass and high pass filters, respectively [10, 12, 23, 30]. From (3.84) and (3.85), c_m^{j-1} is found by passing c_k^j through a low pass filter and d_m^{j-1} by passing c_k^j through a high pass filter, which is consistent since c_m^{j-1} represents a low resolution approximation of the original sequence and d_m^{j-1} represents the details (or high frequency content) of the original signal.

Since (3.90) is recursive, (3.90) and (3.91) can be rewritten [10, 12, 23, 24] as

$$\Phi(\omega) = \prod_{n=1}^{\infty} H\left(\frac{\omega}{2^n}\right) \tag{3.101}$$

$$\Psi(\omega) = G\left(\frac{\omega}{2}\right) \prod_{n=2}^{\infty} H\left(\frac{\omega}{2^n}\right) \tag{3.102}$$

Continuing with Daubechies' D4 wavelet as an example, Figure 3.8 shows the same multiresolution decomposition as Figure 3.6 but in terms of the projection coefficients, c_k^j and d_k^j, only. Notice that as the decomposition proceeds to more levels, the number of coefficients decreases due to the downsampling in (3.84) and (3.85).

In applications like image compression or image enhancement, it is necessary to reconstruct the original coefficients from the decomposition coefficients. Equations (3.99) and (3.100) are the conditions on H and G that guarantee perfect reconstruction, and they can be derived by forming the reconstruction

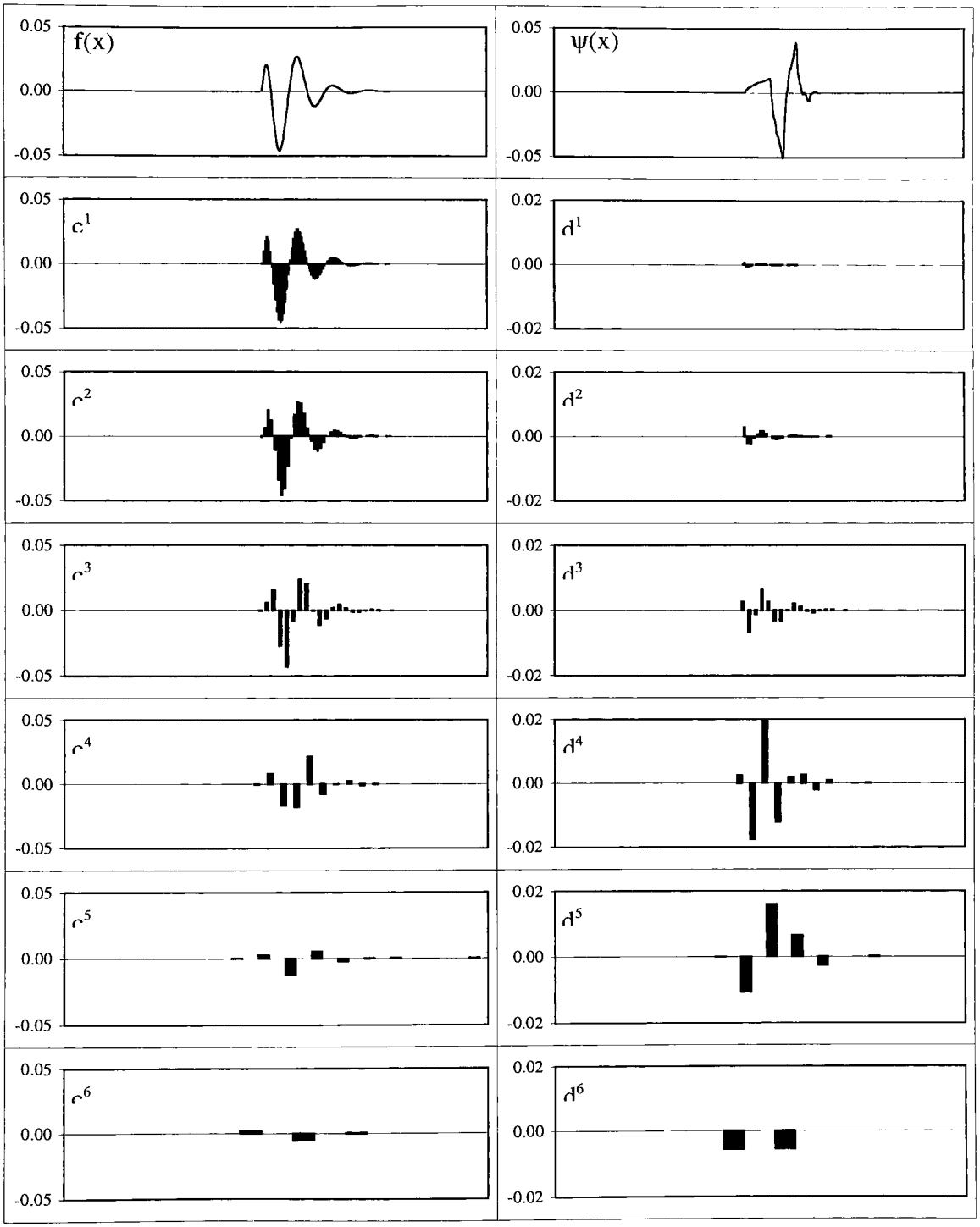

Figure 3.8: Discrete Multiresolution Decomposition of transient signal - Daubechies' D4 filters

expression for c_k^j in Figure 3.4 [12]. $\mathcal{P}^j f$ is the projection of f onto V_j, where $f = f^{j+1}$ in Figure 3.4, and c_k^j are the projection coefficients of $\mathcal{P}^j f \in V_j$,

$$c_k^j = \langle \mathcal{P}^j f, \phi_{j,k} \rangle. \tag{3.103}$$

Substituting (3.43) into (3.103) where $f^j = \mathcal{P}^j f$ gives

$$\begin{aligned} c_k^j &= \langle \mathcal{P}^{j-1} f + \mathcal{Q}^{j-1} f, \phi_{j,k} \rangle \\ &= \langle \mathcal{P}^{j-1} f, \phi_{j,k} \rangle + \langle \mathcal{Q}^{j-1} f, \phi_{j,k} \rangle \\ &= \sum_{m=-\infty}^{\infty} c_m^{j-1} \langle \phi_{j-1,m}, \phi_{j,k} \rangle + \sum_{m=-\infty}^{\infty} d_m^{j-1} \langle \psi_{j-1,m}, \phi_{j,k} \rangle \\ &= \sum_{m=-\infty}^{\infty} c_m^{j-1} h_{k-2m} + \sum_{m=-\infty}^{\infty} d_m^{j-1} g_{k-2m} \end{aligned} \tag{3.104}$$

So, reconstruction is accomplished by upsampling the two sets of coefficients, c_m^{j-1} and d_m^{j-1} and interpolating with the same filters, h_m and g_m, respectively. A single stage decomposition/reconstruction cycle is shown in Figure 3.9 [23]. Figure 3.10 shows the signal spectrum at each stage of the decom-

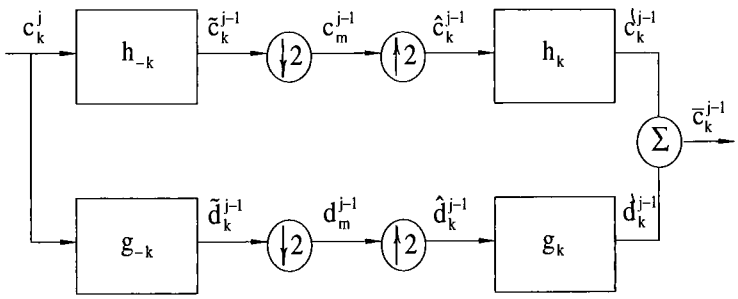

Figure 3.9: Decomposition/Reconstruction cycle with QMF filters

position/reconstruction process. Let the Fourier Transforms of the sequences in Figure 3.9 be given by

$$\begin{aligned} \mathcal{F}(c_k^j) &= C^j(\omega) \\ \mathcal{F}(\tilde{c}_k^{j-1}) &= \tilde{C}^{j-1}(\omega) \\ &\vdots \end{aligned}$$

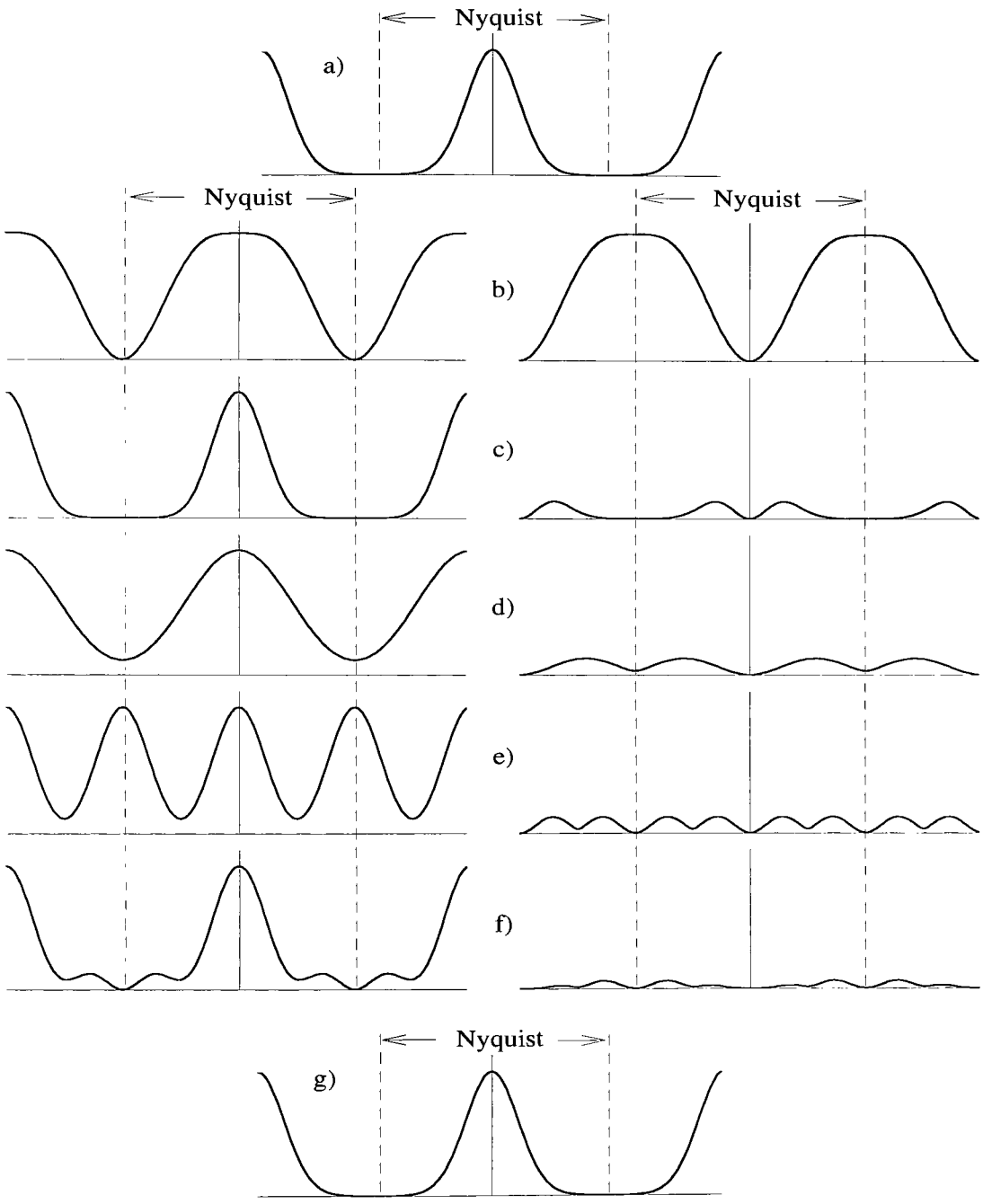

Figure 3.10: DWT Decomposition/Reconstruction - Effects on the Signal Spectrum. a) Original Signal; b) Spectrum of H and G; c) Spectrum of $\tilde{C}^{j-1}$ and $\tilde{D}^{j-1}$; d) Spectrum of C^{j-1} and D^{j-1}; e) Spectrum of $\hat{C}^{j-1}$ and $\hat{D}^{j-1}$; f) Spectrum of $\check{C}^{j}$ and $\check{D}^{j}$; g) Spectrum of $\bar{C}^{j}$

In order to have perfect reconstruction, $\bar{C}^j(\omega)$ must equal $C^j(\omega)$. An expression for $\bar{C}(\omega)$ is obtained by working backwards through Figure 3.9.

$$\bar{C}^j(\omega) = \hat{C}^{j-1}(\omega)H(\omega) + \hat{D}^{j-1}(\omega)G(\omega) \tag{3.105}$$

Upsampling c_m^{j-1} and d_m^{j-1} to obtain $\hat{c}_k^{j-1}$ and $\hat{d}_k^{j-1}$ is done by placing zeroes between each sample, causing a simple dilation of the respective frequency spectra (Figures 3.10d and 3.10e), that is,

$$\begin{aligned} \hat{C}^{j-1}(\omega) &= C^{j-1}(2\omega) \\ \hat{D}^{j-1}(\omega) &= D^{j-1}(2\omega) \end{aligned} \tag{3.106}$$

Downsampling $\tilde{c}_k^{j-1}$ and $\tilde{d}_k^{j-1}$ to obtain c_m^{j-1} and d_m^{j-1} is not as straightforward, because it causes aliasing (Figures 3.10c and 3.10d) [35]. The filtered spectra, $\tilde{C}^{j-1}(\omega)$ and $\tilde{D}^{j-1}(\omega)$ are 2π-periodic and oversampled (Figure 3.10c). However, since $H(\omega)$ and $G(\omega)$ are not ideal filters (Figure 3.10b), the oversampling of $\tilde{C}^{j-1}(\omega)$ and $\tilde{D}^{j-1}(\omega)$ is less than 2, and therefore, downsampling by 2 causes aliasing [35]. The expression for $C^{j-1}(\omega)$ and $D^{j-1}(\omega)$ in terms of $\tilde{C}^{j-1}(\omega)$ and $\tilde{D}^{j-1}(\omega)$ must include the aliasing terms

$$\begin{aligned} C^{j-1}(\omega) &= \tilde{C}^{j-1}\left(\frac{\omega}{2}\right) + \tilde{C}^{j-1}\left(\frac{\omega}{2} + \pi\right) \\ D^{j-1}(\omega) &= \tilde{D}^{j-1}\left(\frac{\omega}{2}\right) + \tilde{D}^{j-1}\left(\frac{\omega}{2} + \pi\right) \end{aligned} \tag{3.107}$$

Finally, $\tilde{C}^{j-1}(\omega)$ and $\tilde{D}^{j-1}(\omega)$ are filtered versions of the input spectrum, $C^j(\omega)$

$$\begin{aligned} \tilde{C}^{j-1}(\omega) &= C^j(\omega)\overline{H(\omega)} \\ \tilde{D}^{j-1}(\omega) &= C^j(\omega)\overline{G(\omega)} \end{aligned} \tag{3.108}$$

The complex conjugates of the filter spectra in (3.108) are due to the digital filters being index-reversed, h_{-k} and g_{-k}. Substituting from (3.108) back to (3.105) gives

$$\begin{aligned} \bar{C}(\omega) \;=\; & \left[H(\omega)\overline{H(\omega)} + G(\omega)\overline{G(\omega)}\right] C^j(\omega) + \\ & \left[H(\omega)\overline{H(\omega+\pi)} + G(\omega)\overline{G(\omega+\pi)}\right] C^j(\omega+\pi) \end{aligned} \tag{3.109}$$

The two conditions for perfect reconstruction emerge from (3.109) [12, 35]

$$|H(\omega)|^2 + |G(\omega)|^2 = 1 \tag{3.110}$$

$$H(\omega)\overline{H(\omega+\pi)} + G(\omega)\overline{G(\omega+\pi)} = 0 \tag{3.111}$$

The formulation of these filter requirements for perfect reconstruction is well known in the field of subband coding [35].

If the relationship between $H(\omega)$ and $G(\omega)$ were constrained such that

$$G(\omega) = e^{-i\omega}\overline{H(\omega+\pi)} \tag{3.112}$$

then the second condition (3.100) is always satisfied [12, 35] and (3.99) becomes

$$|H(\omega)|^2 + |H(\omega+\pi)|^2 = 1 \tag{3.113}$$

These filters are called "quadrature mirror filters (QMF)" and the structure of Figure 3.9 is known as a 2-band QMF [35]. Taking the inverse Fourier Transform of (3.112) gives the relationship between h and g

$$g_k = (-1)^{k+1}h_{1-k} \tag{3.114}$$

Substituting (3.86) and (3.87) into (3.114) gives the relationship between the generating sequences that guarantees perfect reconstruction in a multiresolution analysis

$$q_k = (-1)^{k+1}p_{1-k} \tag{3.115}$$

Assume p_k, a generating sequence for $\phi(x)$, exists such that (3.69) and (3.73) are satisfied. Then, clearly, conditions (3.92) and (3.96) on h_k will also be satisfied. These conditions imply that $\phi_{j,k}$ is an orthonormal basis of V_j and that $\int \phi(x)dx = 1$. Assuming the relationship between h_k and g_k in (3.114), it can be shown by substitution of (3.114) that every condition (3.90)-(3.100) is satisfied and $\phi(x)$ generates an orthonormal multiresolution analysis! The two-scale relation for $\psi(x)$ becomes

$$\psi(x) = \sum_{k=-\infty}^{\infty} (-1)^{k+1}p_{1-k}\phi(2x-k) \tag{3.116}$$

3.7 2-Dimensional DWT

A 2-dimensional multiresolution analysis (MRA) is defined as a sequence of subspaces, $\{V_j^2\}$, which satisfies the conditions in Definition 7, but defined on the Hilbert space $L^2(\Re^2)$ [12]. Assume $\phi_{j,k,l}(x,y) = 2^j\phi(2^jx - k, 2^jy - l)$ is an orthonormal basis of $V_j^2 \subset L^2(\Re^2)$, where $\phi(x,y)$ is the 2-dimensional scaling function that generates the orthonormal MRA, $\{V_j^2\}$. Meyer showed that if $\phi_{j,k,l}(x,y)$ is separable, then V_j^2 is the tensor product of two identical subspaces of $L^2(\Re)$ [12]

$$V_j^2 = V_j \otimes V_j$$

where $V_j \subset L^2(\Re)$. The 2-dimensional, separable scaling function becomes

$$\phi(x,y) = \phi(x) \cdot \phi(y) \tag{3.117}$$

where $\phi(x)$ and $\psi(y)$ generate identical orthonormal multiresolution analyses, $\{V_j\}$, of $L^2(\Re)$ and $\phi_{j,k}(x)$ and $\phi_{j,l}(y)$ form orthonormal bases of $V_j \subset L^2(\Re)$. Just as in the 1-dimensional case, a signal, $f^{j+1}(x,y)$, at scale $j+1$ can be represented by the sum of its projections into orthogonal subspaces at scale j. Given separability, $f^{j+1}(x,y)$ is projected in x onto V_j and W_j and then in y onto V_j and W_j. Since $V_{j+1}^2 = V_{j+1} \otimes V_{j+1}$, and $V_{j+1} = V_j \dot{+} W_j$, then the 2-dimensional, separable projection produces 4 subspaces [12].

$$\begin{aligned} V_{j+1}^2 &= V_{j+1} \otimes V_{j+1} \\ &= (V_j \dot{+} W_j) \otimes (V_j \dot{+} W_j) \\ &= V_j \otimes V_j \dot{+} V_j \otimes W_j \dot{+} W_j \otimes V_j \dot{+} W_j \otimes W_j \end{aligned}$$

where the first subspace is V_j^2 and contains the low resolution approximation, $f^j(x,y)$, and the remaining three subspaces are wavelet subspaces that contain some version of the details projected from $f^{j+1}(x,y)$. The 2-dimensional bases for each of these subspaces is given as follows [12]:

$$\phi_{j,k}(x)\phi_{j,l}(y)$$

$$\phi_{j,k}(x)\psi_{j,l}(y)$$

$$\psi_{j,k}(x)\phi_{j,l}(y)$$

$$\psi_{j,k}(x)\psi_{j,l}(y).$$

The multiresolution decomposition of a 2-dimensional signal is shown in Figure 3.11. From Figure 3.11,

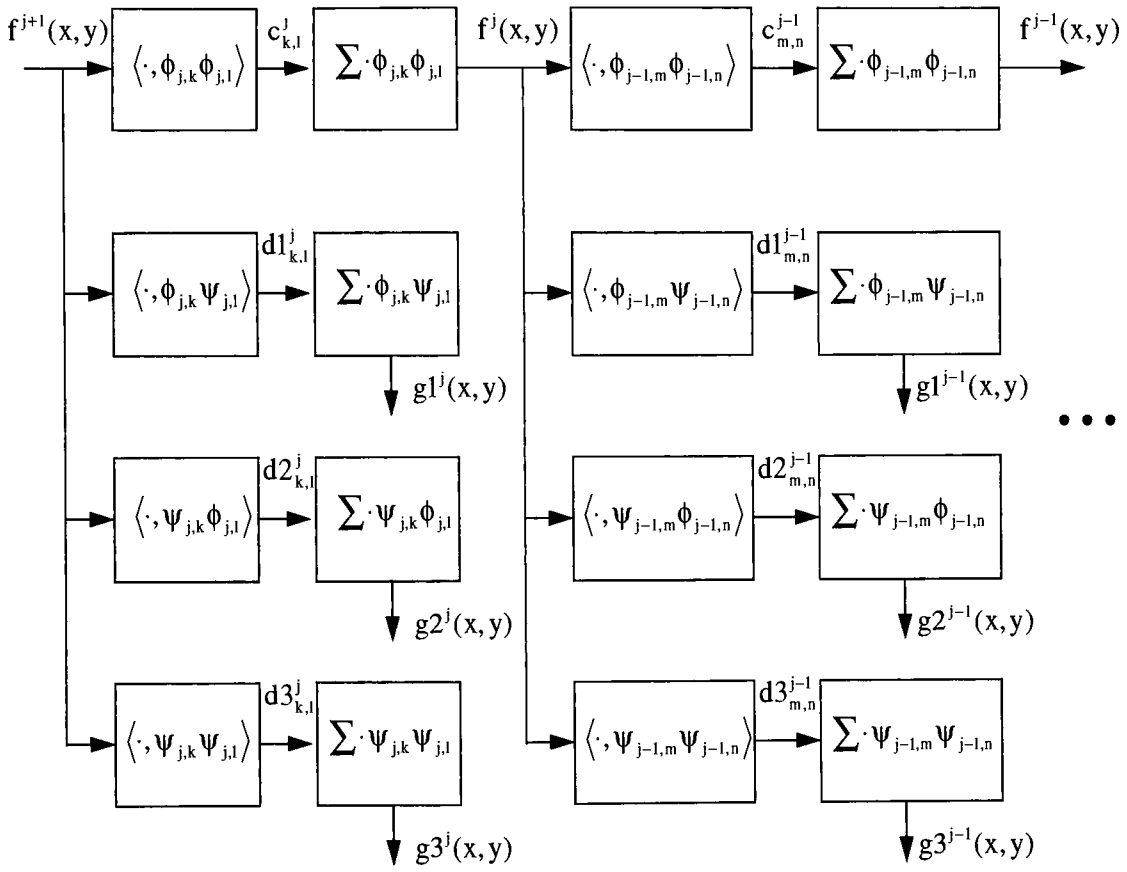

Figure 3.11: 2-D Multiresolution Decomposition

$$\begin{aligned} c^{j-1}_{m,n} &= \langle \mathcal{P}^j f, \phi_{j-1,m}(x)\phi_{j-1n}(y)\rangle \\ &= \langle \sum_{l=-\infty}^{\infty}\sum_{k=-\infty}^{\infty} c^j_{k,l}\phi_{j,k}(x)\phi_{j,l}(y), \phi_{j-1,m}(x)\phi_{j-1,n}(y)\rangle \\ &= \sum_{l=-\infty}^{\infty}\sum_{k=-\infty}^{\infty} c^j_{k,l}\langle \phi_{j,k}(x)\phi_{j,l}(y), \phi_{j-1,m}(x)\phi_{j-1,n}(y)\rangle \end{aligned}$$

$$= \sum_{l=-\infty}^{\infty} \sum_{k=-\infty}^{\infty} c_{k,l}^{j} \langle \phi_{j,k}(x), \phi_{j-1,m}(x) \rangle \langle \phi_{j,l}(y), \phi_{j-1,n}(y) \rangle$$

$$= \sum_{l=-\infty}^{\infty} \sum_{k=-\infty}^{\infty} c_{k,l}^{j} h_{k-2m} h_{l-2n} \tag{3.118}$$

Likewise,

$$d1_{m,n}^{j-1} = \sum_{l=-\infty}^{\infty} \sum_{k=-\infty}^{\infty} c_{k,l}^{j} h_{k-2m} g_{l-2n} \tag{3.119}$$

$$d2_{m,n}^{j-1} = \sum_{l=-\infty}^{\infty} \sum_{k=-\infty}^{\infty} c_{k,l}^{j} g_{k-2m} h_{l-2n} \tag{3.120}$$

$$d3_{m,n}^{j-1} = \sum_{l=-\infty}^{\infty} \sum_{k=-\infty}^{\infty} c_{k,l}^{j} g_{k-2m} g_{l-2n} \tag{3.121}$$

Equations (3.118)-(3.121) constitute the 2-dimensional Discrete Wavelet Transform [12, 23]. The low resolution approximation of the original sequence is found by low pass filtering in both the row and column dimensions. $d1_{m,n}^{j-1}$ is found by low pass filtering the rows and high pass filtering the columns, $d2_{m,n}^{j-1}$ by high pass filtering the rows and low pass filtering the columns, and $d_{m,n}^{j-1}$ by high pass filtering both the rows and columns. Figure 3.12 shows an original 256x256 image and its 4-level multiresolution decomposition computed with the 2-D DWT based on Daubechies' $D4$ wavelet.

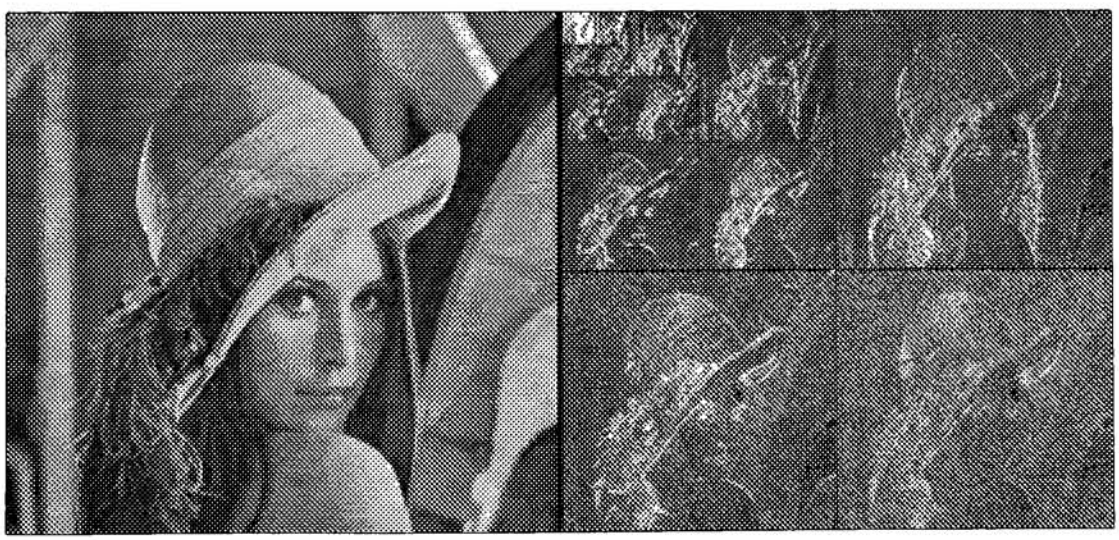

Figure 3.12: Multiresolution Decomposition of Lena Using Daubechies' D4 Wavelet

3.8 Limitations to the MRA and DWT

3.8.1 MRAs

While the MRA construction developed by Mallat and Meyer [24] provides both time and frequency localization of signals containing both high and low frequencies, something the Short Time Fourier Transform (STFT) was unable to do, it does not do a good job of representing all functions in $L^2(\Re)$ [25]. Signals with narrowband, high frequency components are not well represented because of the constant Q feature of the passbands. When the scale parameter, j in $2^{j/2}\psi(2^j x - k)$, increases by 1, the scale doubles as does the bandwidth. The constant Q restriction does not provide independent control over center frequency of a passband and its bandwidth. Mallat and Zheng make provisions for independent control by including a phase modulation term to their time-frequency atom [25]. Wickerhauser generalized Mallat's MRA when they developed the wavelet packet paradigm [36]. In an MRA, a signal is projected into two orthogonal subspaces, V_j and W_j. Subsequent decomposition is done on $f^j(x) \in V_j$. Wickerhauser removed this constraint and allowed the detail signal, $g^j(x) \in W_j$ to be decomposed if it had the dominant energy. The resultant decomposition tree, an example of which is given in Figure 3.13, can take on $O(2^N - 1)$ different configurations where N is the number of levels of the decomposition. Mallat's MRA is only one of those configurations.

For many naturally occuring signals, however, the bandwidth of a signal component is a function of its center frequency. For example, a radar transmitter can transmit a signal with a bandwidth on the order of 10% of its center frequency, in which case, the Q of the transmitter would be 0.10. Before applying wavelets to an application, it is important to determine which class of wavelet is appropriate.

3.8.2 DWT

The discrete wavelet transform implements Mallat's multiresolution with digital filters. The decomposition equations for the low resolution and detail projection coefficients, c_k^j and d_k^j are given as

$$c_k^j = \sum_{m=-\infty}^{\infty} c_m^{j+1} h_{m-2k} \tag{3.122}$$

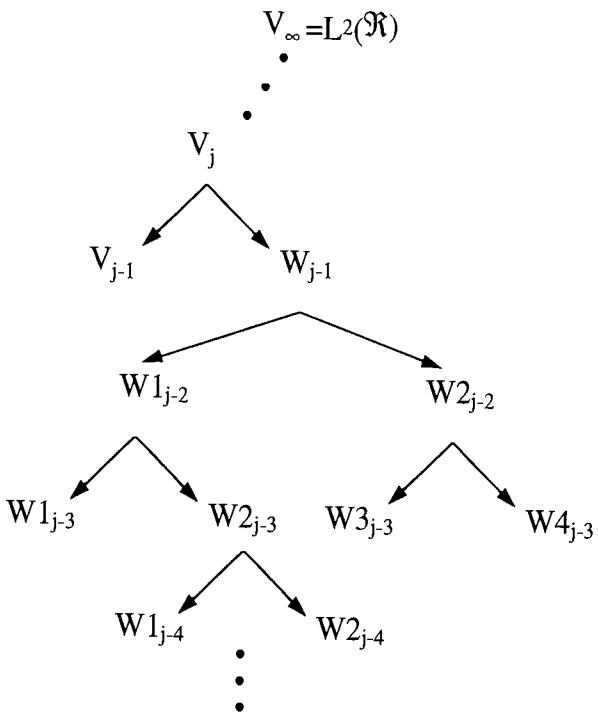

Figure 3.13: Example Wavelet Packet Decomposition

$$d_k^j = \sum_{m=-\infty}^{\infty} c_m^{j+1} g_{m-2k} \tag{3.123}$$

where h and g are low and high pass filters, respectively. Notice, however, that neither (3.122) nor (3.123) are shift invariant. Let the input sequence be shifted by $n \in \mathbb{Z}$, then (3.122) becomes

$$\begin{aligned} \hat{c}_k^j &= \sum_{m=-\infty}^{\infty} c_{m-n}^{j+1} h_{m-2k} \\ &= \sum_{\ell=-\infty}^{\infty} c_\ell^{j+1} h_{\ell-2(k-n/2)} \\ &\neq c_{k-n}^j \end{aligned} \tag{3.124}$$

and likewise for (3.123). The fact that the DWT is shift variant makes it very difficult to use in applications like object detection and pattern recognition because the output of the decomposition is dependent on the input sequence [23].

3.8.3 2-D DWT

The same limitations on the DWT apply to the 2-D DWT. The multiresolution decomposition coefficients of an image are dependent on the input image, making repeatability for a given class of images impossible. Furthermore, the implementation of the 2-D DWT developed in Section 3.7 assumes separable 2-D wavelets and scaling functions. This assumption greatly simplifies the 2-D DWT, but results in an algorithm that is very sensitive to image rotation. This limitation makes the 2-D DWT even less attractive for pattern recognition or object detection.

Chapter 4

Wavelet Design Techniques

The development of wavelet multiresolution analyses provides the necessary framework for designing whole new classes of wavelets. Ingrid Daubechies provided remarkable insight into wavelet design when she published her technique for finding orthonormal wavelet bases with compact support [12]. Others used the mathematical construct provided by an MRA to define scaling functions and their corresponding wavelets that were optimum in some sense. Splines were used to achieve maximum smoothness, projections were used to find wavelets that were somewhat matched to the signal of interest. In each of these cases, however, the design emphasis is on the scaling function, $\phi(x)$ or its generating sequence, h_k, which is to be expected since the MRA is generated by the scaling function. In this chapter, 6 different design techniques will be reviewed in order to provide motivation for the new wavelet design technique presented in Chapter 5.

4.1 Compactly Supported Wavelets

In 1987, Ingrid Daubechies, inspired by Mallat's Discrete Wavelet Transform algorithm, succeeded in constructing orthonormal wavelet bases with compact support in the space domain [14]. Her technique takes advantage of the orthonormality constraints put on the digital quadrature mirror filter (QMF), h_k, which is also the generating sequence for the scaling function, $\phi(x)$, of an MRA. It is easy to see from (5.17) and (5.18) that a finite generating sequence gives rise to a compactly supported scaling function

and wavelet. Assuming h_k is finite in length, $M = 2N-1$, its Fourier Transform becomes a polynomial in $e^{-i\omega k}$,

$$H(\omega) = \sum_{k=0}^{2N-1} h_k e^{-i\omega k}. \tag{4.1}$$

Daubechies added constraints on $H(\omega)$ that would guarantee some degree of smoothness in the result, namely that $H(\omega)$ should have N zeros at $\omega = \pi$, giving $H(\omega)$ the following form,

$$H(\omega) = \left(\frac{1+e^{i\omega}}{2}\right)^N W(\omega). \tag{4.2}$$

Since $H(\omega)$ is a polynomial of degree $2N-1$, Daubechies is essentially dedicating N degrees of freedom in $H(\omega)$ toward guaranteeing smoothness. The remaining task is to find polynomials of the form (4.2) that satisfy the orthonormality condition (3.113). The set of all such polynomials can be found using some rather sophisticated theorems of algebra. Kaiser [19], however, follows a shortcut showing that the solution for $N = 1$, which is the Haar system, actually generates solutions for all $N \geq 2$. For $N = 1$, $h_k = \{1/2, 1/2\}$ giving

$$H(\omega) = \frac{1+e^{i\omega}}{2} = e^{i\frac{\omega}{2}} \cos(\omega/2) \tag{4.3}$$

$$H(\omega+\pi) = \frac{1-e^{i\omega}}{2} = ie^{i\frac{\omega}{2}} \sin(\omega/2). \tag{4.4}$$

For $N \geq 2$, let

$$C(\omega) = \cos(\omega/2) \quad \text{and} \quad S(\omega) = \sin(\omega/2). \tag{4.5}$$

Raising $C^2 + S^2 = 1$ to the power $2N-1$ gives

$$1 = \sum_{k=0}^{2N-1} \binom{2N-1}{k} C^{4N-2-2k} S^{2k} \tag{4.6}$$

where $\binom{M}{k} = M!/k!(M-k)!$ are the binomial coefficients. Kaiser shows that if the polynomial, $\mathcal{H}_N(C)$, consists of the first N terms of (4.6) and $H(\omega)$ can be found such that $|H(\omega)|^2 = \mathcal{H}_N(C)$, then $|H(\omega+\pi)|^2$ is automatically the last N terms of (4.6), thereby satisfying the orthonormality condition in (3.113) [19]. From (4.6), $\mathcal{H}$ can be factored as follows,

$$\mathcal{H} = |H(\omega)|^2 = C^{2N}\mathcal{W}_N(S) = \left|\frac{1+e^{i\omega}}{2}\right|^{2N} \mathcal{W}_N(S) \tag{4.7}$$

where

$$\mathcal{W}_N(S) = \sum_{k=0}^{N-1} \binom{2N-1}{k} C^{2N-2-2k} S^{2k} \tag{4.8}$$

$$= \sum_{k=0}^{N-1} \binom{2N-1}{k} (1-S^2)^{N-1-k} S^{2k}. \tag{4.9}$$

The expression in (4.7) has exactly the form of the squared magnitude of (4.2). So all that is left is finding a polynomial, $W(\omega)$, such that $|W(\omega)|^2 = \mathcal{W}_N(S(\omega))$, which can be done through algebraic manipulation.

An example for $N = 2$ will show the complete process,

$$\mathcal{W}_2(S) = \sum_{k=0}^{1} \binom{3}{k} (1-S^2)^{1-k} S^{2k} \tag{4.10}$$

$$= (1-S^2) + 3S^2 \tag{4.11}$$

$$= 1 + 2S^2 \tag{4.12}$$

$$= 1 + 2\left(\frac{e^{i\omega} - e^{-i\omega}}{i2}\right)^2 \tag{4.13}$$

$$= 2 - \frac{1}{2}\left(e^{i\omega} + e^{-i\omega}\right). \tag{4.14}$$

Since $\mathcal{W}_2(S) = |W(\omega)|^2$ and $W(\omega)$ is a polynomial in $e^{i\omega}$ of order 2, then

$$2 - \frac{1}{2}(e^{i\omega} + e^{-i\omega}) = |a + be^{i\omega}|^2$$

$$= (a^2 + b^2) + ab(e^{i\omega} + e^{-i\omega}) \tag{4.15}$$

which gives $a = \frac{1}{2}(1+\sqrt{3})$ and $b = \frac{1}{2}(1-\sqrt{3})$. Expanding (4.2) gives

$$H(\omega) = \left(\frac{1+e^{i\omega}}{2}\right)(a + be^{i\omega})$$

$$= \frac{1}{4}\left(a + (2a+b)e^{i\omega} + (a+2b)e^{i2\omega} + be^{i3\omega}\right) \tag{4.16}$$

so the 4 coefficients for the QMF filter of Daubechies' D4 system are given by

$$\begin{bmatrix} h_0 \\ h_1 \\ h_2 \\ h_3 \end{bmatrix} = \begin{bmatrix} a \\ 2a+b \\ a+2b \\ b \end{bmatrix} = \frac{1}{8}\begin{bmatrix} 1+\sqrt{3} \\ 3+\sqrt{3} \\ 3-\sqrt{3} \\ 1-\sqrt{3} \end{bmatrix}. \tag{4.17}$$

Once the filter coefficients, h_k, are found, $\phi(x)$ can be found recursively using (5.17) and $\psi(x)$ can be found directly using (5.18) where $g_k = (-1)^{k+1}h_{1-k}$.

This technique is very clever and was considered landmark in the development of orthonormal wavelet bases. However, as can be seen from this entire process, the design is focused on the low pass filter, h_k. Nowhere in this technique are the requirements on the wavelet addressed. After finding the generating sequence, h_k, the scaling function and wavelet are found using (5.17) and (5.18). The wavelet is driven entirely by h_k, and subsequently, $\phi(x)$.

4.2 Wavelets for Signal Representation

Tewfik, Sinha, and Jorgensen [34] developed a technique for finding an orthonormal wavelet with compact support that provides the "best" signal representation of a specified signal over a finite number of scales. In an orthonormal multiresolution analysis (MRA), a signal, $f(x) \in L^2(\Re)$ can be represented by an infinite sum of detail functions, $g^j(x)$, given in (3.28) and (3.29), where the projection operator is the inner product with the orthonormal wavelet basis, $2^{j/2}\psi(2^j x - k)$. Truncating the infinite sum to N scales, say scale j to $j + 1 - N$ gives the following approximation of $f(x)$,

$$\hat{f}(x) = f^{j+1}(x) = \sum_{i=1}^{N} g^{j+1-i}(x) + f^{j+1-N}(x). \tag{4.18}$$

However, since $V_{j+1} = W_j \dot{+} W_{j-1} \dot{+} \ldots \dot{+} W_{j-N+1} \dot{+} V_{j-N+1}$, (4.18) is equivalent to $\hat{f}(x)$ being represented by the orthonormal basis of V_{j+1}, namely $2^{(j+1)/2}\phi(2^{j+1}x - k)$, where $\phi(x)$ is the scaling function. So, (4.18) can be rewritten as

$$\hat{f}(x) = \sum_{k=-\infty}^{\infty} a_k 2^{\frac{j+1}{2}} \phi(2^{j+1}x - k) \tag{4.19}$$

which in the frequency domain is given as

$$\hat{F}(\omega) = 2^{-\frac{j}{2}} A(2^{-j}\omega)\Phi(2^{-j}\omega) \tag{4.20}$$

where $A(\omega)$ is the Fourier transform of a_k and therefore 2π periodic. The L^2 error norm between the signal and its approximation is given in the frequency domain as

$$\left\| F(\omega) - 2^{-\frac{j}{2}} A(2^{-j}\omega)\Phi(2^{-j}\omega) \right\| = \left\| 2^{\frac{j}{2}} F(2^j\omega) - A(\omega)\Phi(\omega) \right\|. \tag{4.21}$$

Tewfik, et. al., assuming compactly supported wavelets, parameterize the generating sequence, h_k, using Daubechies' polynomial factoring "trick" and develop an upper bound to the error in (4.21) where the bound is in terms of h_k only. Once the upper bound is given, they use constrained optimization techniques to solve for the finite length h_k that minimizes the upper error bound on the signal representation. Once again, as in Daubechies' technique, the design emphasis is on h_k, the generating sequence of the scaling function. No design criteria are put on the wavelet, whatsoever. This comes about because as shown in (4.19), a finite wavelet decomposition can be recast as a projection of the signal into the next higher approximation subspace, V_{j+1}, and the only contributor to the approximation accuracy is the scaling function.

Gopinath, Odegard and Burrus [18] expanded the work of Tewfik, et. al., by assuming bandlimited wavelets. This additional condition simplified the upper bound of the error norm (4.21) giving way to a much simpler numerical solution. However, Gopinath, et. al., likewise acknowledge the importance of the scaling function in their approach when they state "the approximation at resolution J depends only on the scaling function, and not on the corresponding wavelets"[18].

4.3 Entropy-Based Best Basis Selection

Coifman and Wickerhauser [11] developed a technique for finding the "best" basis for a given signal using orthonormal wavelets. They create a library of known orthonormal wavelet bases, $\mathcal{B}$. The best basis is that family of wavelets from $\mathcal{B}$ that minimizes the entropy of the discrete decomposition. Given a vector, f_k, the N-level discrete decomposition consists of N detail vectors, g_k^j, for $j = 1, 2, \ldots N$. The entropy of the decomposition is defined as [11]

$$\epsilon = -\sum_j \|g^j\|^2 \ln \|g^j\|^2. \tag{4.22}$$

However, because the search of all possible orthonormal bases in a complete library is too computationally intensive, Coifman and Wickerhauser restrict the library to only rapidly computable orthonormal bases, like the local trigonometric basis and the Haar basis[11]. The basis calculated is only "best" in the context of their previously designed library.

4.4 Matching Pursuit with Time-Frequency Dictionaries

Mallat and Zheng [25] and Chen and Donoho [9] identified a need to generalize the orthonormal wavelet decomposition work of Mallat [23]. Mallat and Zheng point out that a single wavelet basis is not flexible enough to represent a complicated non-stationary signal, primarily those with narrow band high-frequency support [25]. They say that it is much like a person trying to communicate with a very limited vocabulary. When the need for a word arises that is not in the vocabulary, many other words are needed to compensate for the lack of the right word. They go on to say that it is difficult to detect a pattern from its projection coefficients because the information is spread out over the whole basis. Each of these limitations will be specifically addressed in the design approach of Chapter 5.

In order to increase the flexibility in signal representation, Mallat, et. al., construct a dictionary of time-frequency atoms of the form,

$$g_\gamma(x) = \frac{1}{\sqrt{a}} g\left(\frac{x-b}{a}\right) e^{i\xi x} \tag{4.23}$$

where $\|g\| = 1$, $\int g(x)dx \neq 0$ and $g(0) \neq 0$. Notice that (4.23) looks very much like the wavelet expression given by Morlet and Grossman, except that it includes a phase modulation term. This term can be used to translate the frequency spectrum of $g_\gamma(x)$ up and down the frequency axis, thereby allowing a narrowband spectrum to reside at high frequencies.

Mallat and Zheng show that the dictionary consisting of the time-frequency atoms of (4.23) is complete, that is, that the closed linear span of the dictionary vectors is $L^2(\Re)$. The objective is to find the best representation of a signal using the vectors in the dictionary. Given a signal, $f \in L^2(\Re)$, its first order representation is given by

$$f = \langle f, g_{\gamma_0} \rangle g_{\gamma_0} + Rf \tag{4.24}$$

where g_{γ_0} is the time frequency atom such that $|\langle f, g_{\gamma_0} \rangle|^2$ is a maximum. The first term of (4.24) represents the orthogonal projection of f onto the space spanned by g_{γ_0}. Therefore, $\langle f, g_{\gamma_0} \rangle g_{\gamma_0} \perp Rf$ and

$$\begin{aligned} \|f\|^2 &= \|\langle f, g_{\gamma_0} \rangle g_{\gamma_0}\|^2 + \|Rf\|^2 \\ &= |\langle f, g_{\gamma_0} \rangle|^2 + \|Rf\|^2 \end{aligned} \tag{4.25}$$

since $\|g_{\gamma_0}\| = 1$. Now the process can be repeated for Rf,

$$Rf = \langle Rf, g_{\gamma_1} \rangle g_{\gamma_1} + R^1 f \tag{4.26}$$

where the energy decomposition of f is now

$$\|f\|^2 = |\langle f, g_{\gamma_0} \rangle|^2 + |\langle f, g_{\gamma_1} \rangle|^2 + \|R^1 f\|^2. \tag{4.27}$$

Each decomposition of the residual is done by finding the time-frequency atom, g_γ that maximizes the energy of the projection coefficients, thereby assuring rapid convergence. In applications like pattern recognition, signal reconstruction and enhancement, the atoms chosen and their corresponding projection coefficients can be used to characterize or represent the signal f.

However, the representation is only as good as the collection of atoms in its dictionary. Each g_γ must either be designed or discovered before ever proceeding with the adaptive algorithm. Furthermore, the algorithm will do best if the atoms in the dictionary look like the signal under analysis or its components.

4.5 Multiresolution Analysis-type Wavelets

Abry and Aldroubi [2] developed an algorithm for designing wavelets for semi-orthogonal multiresolution analyses. In a semi-orthongonal MRA, the wavelet vector spaces, W_j, are orthogonal to one another, but $\psi_{j,k}$ does not form an orthonormal basis of W_j, that is,

$$\langle \psi_{j,k}, \psi_{\ell,m} \rangle = \delta_{j,\ell} \cdot \rho_{k,m} \tag{4.28}$$

where $\psi_{j,k} = 2^{j/2}\psi(2^j x - k)$ and $\rho_{k,m} \neq \delta_{k,m}$. Just as a non-orthogonal scaling function can be orthogonalized using (3.42), Abry and Aldroubi showed that an orthogonal scaling function can be de-orthogonalized by an admissible discrete sequence, such that the result generates the same MRA as the original scaling function.

Let $\phi_\perp(x)$ be an orthonormal scaling function that generates the MRA, $\{V_j\}$. Let

$$\hat{\phi}(x) = \sum_{k=-\infty}^{\infty} a_k \phi_\perp(x - k) \tag{4.29}$$

be a linear combination of the orthonormal basis of V_0. Then, $\hat{\phi}(x)$ generates the same MRA, $\{V_j\}$, which can be easily shown in the frequency domain [2]. The Fourier transform of (4.29) gives

$$\hat{\Phi}(\omega) = A(\omega)\Phi_{\perp}(\omega). \tag{4.30}$$

Notice that from (3.42), $|A(\omega)|$ must by necessity be the square root of the Poisson summation of $\hat{\Phi}(\omega)$, that is,

$$|A(\omega)| = \left(\sum_{k=-\infty}^{\infty} |\hat{\Phi}(\omega + 2\pi k)|^2 \right)^{\frac{1}{2}}. \tag{4.31}$$

Since $\phi_{\perp}(x)$ generates an MRA, it must satisfy its 2-scale relation, (3.88), which in the frequency domain is given by

$$\Phi_{\perp}(\omega) = H\left(\frac{\omega}{2}\right)\Phi_{\perp}\left(\frac{\omega}{2}\right). \tag{4.32}$$

Substituting (4.30) into (4.32) gives

$$\begin{aligned} \hat{\Phi}(\omega) &= \frac{H\left(\frac{\omega}{2}\right)A(\omega)}{A\left(\frac{\omega}{2}\right)}\hat{\Phi}\left(\frac{\omega}{2}\right) \\ &= \hat{H}\left(\frac{\omega}{2}\right)\hat{\Phi}\left(\frac{\omega}{2}\right) \end{aligned} \tag{4.33}$$

where $\hat{H}(\omega)$ is 2π periodic and $0 < A \leq A(\omega) \leq B < \infty$ is the admissibility condition on the sequence, a_k [2]. Since $\hat{\phi}(x)$ satisfies its 2-scale relation, it too generates the same MRA as $\phi_{\perp}(x)$. The new 2-scale relation is given as

$$\hat{\phi}(x) = \sum_{k=-\infty}^{\infty} \hat{h}_k \hat{\phi}(2x - k) \tag{4.34}$$

where $\hat{h}_k$ is the inverse Fourier transform of $\hat{H}(\omega)$ in (4.33).

The same approach can be applied to the wavelet basis of W_j. Let $\psi_{\perp}(x - k)$ be the orthonormal basis of W_0 and let a new wavelet be constructed in W_0 by a linear combination of $\psi_{\perp}(x - k)$, then,

$$\hat{\psi}(x) = \sum_{k=-\infty}^{\infty} b_k \psi_{\perp}(x - k) \tag{4.35}$$

given in the frequency domain as

$$\hat{\Psi}(\omega) = B(\omega)\Psi_{\perp}(\omega). \tag{4.36}$$

Since $\psi_\perp(x)$ satisfies its 2-scale relation (3.89) given in the frequency domain by

$$\Psi_\perp(\omega) = G\left(\frac{\omega}{2}\right)\Phi_\perp\left(\frac{\omega}{2}\right), \tag{4.37}$$

then substituting (4.36) into (4.37) gives [2]

$$\begin{aligned}\hat{\Psi}(\omega) &= B(\omega)G\left(\frac{\omega}{2}\right)\Phi_\perp\left(\frac{\omega}{2}\right) \\ &= \hat{G}\left(\frac{\omega}{2}\right)\Phi_\perp\left(\frac{\omega}{2}\right)\end{aligned} \tag{4.38}$$

where $\hat{G}(\omega) = B(\omega)G(\omega/2)$ is the Fourier transform of the new generating sequence, $\hat{g}_k$. The new 2-scale relation for $\hat{\psi}(x)$ is therefore given as

$$\hat{\psi}(x) = \sum_{k=-\infty}^{\infty} \hat{g}_k \phi_\perp(2x-k) \tag{4.39}$$

where $\psi(x)$ is expressed as a linear combination of the orthonormal basis of V_1. However, $\psi(x)$ can also be expressed as a linear combination of any basis of V_1. Substituting for $\Phi_\perp(\omega)$ in (4.38) using (4.30) gives

$$\begin{aligned}\hat{\Psi}(\omega) &= \frac{B(\omega)G\left(\frac{\omega}{2}\right)}{A\left(\frac{\omega}{2}\right)}\hat{\Phi}\left(\frac{\omega}{2}\right) \\ &= \hat{G}^1\left(\frac{\omega}{2}\right)\hat{\Phi}\left(\frac{\omega}{2}\right)\end{aligned} \tag{4.40}$$

The new 2-scale relation for $\hat{\psi}(x)$ in terms of $\hat{\phi}(x)$ is given as

$$\hat{\psi}(x) = \sum_{k=-\infty}^{\infty} \hat{g}_k^1 \hat{\phi}(2x-k) \tag{4.41}$$

where $\hat{g}_k^1$ is the inverse Fourier transform of $\hat{G}^1(\omega) = B(2\omega)G(\omega)/A(\omega)$ [2].

While $\hat{\phi}$ and $\hat{\psi}$ are not orthonormal, the new generating sequences, $\hat{h}$ and $\hat{g}$, can still be used for *synthesis* in the DWT algorithm of Chapter 3. However, the *analysis* filters, $\tilde{h}$ and $\tilde{g}$, must be found from the duals of $\hat{\phi}(x)$ and $\hat{\psi}(x)$, respectively. The Fourier transforms of the duals, $\tilde{\phi}$ and $\tilde{\psi}$ are given as

$$\tilde{\Phi}(\omega) = \frac{\hat{\Phi}(\omega)}{\sum_{k=-\infty}^{\infty}|\hat{\Phi}(\omega+2\pi k)|^2} \tag{4.42}$$

$$\tilde{\Psi}(\omega) = \frac{\hat{\Psi}(\omega)}{\sum_{k=-\infty}^{\infty}|\hat{\Psi}(\omega+2\pi k)|^2} \tag{4.43}$$

so that

$$\langle \hat{\phi}_{j,k}, \tilde{\phi}_{j,m} \rangle = \delta_{k,m} \tag{4.44}$$

$$\langle \hat{\psi}_{j,k}, \tilde{\psi}_{j,m} \rangle = \delta_{k,m}. \tag{4.45}$$

Notice that (4.42) and (4.43) have the same form as (4.30) and (4.36) where

$$A(\omega) = \frac{1}{\sum_{k=-\infty}^{\infty} |\Phi(\omega + 2\pi k)|^2} \tag{4.46}$$

$$B(\omega) = \frac{1}{\sum_{k=-\infty}^{\infty} |\Psi(\omega + 2\pi k)|^2}. \tag{4.47}$$

The analysis filters, $\tilde{h}$ and $\tilde{g}$, can now be found using the same technique as described above.

In order to use the relationships given above to design matching wavelets, one must be able to find the appropriate discrete sequence, b_k. Abry and Aldroubi find b_k by projecting the desired signal, $f(x)$ into W_0. The resulting approximation is given as

$$\hat{f}(x) = \sum_{k=-\infty}^{\infty} b_k \hat{\psi}(x - k) \tag{4.48}$$

where the discrete sequence, b_k are simply the projection coefficients. One drawback to this algorithm for finding matched wavelets, is that the MRA and therefore $\phi_\perp$ and $\psi_\perp$ must already exist. Furthermore, the quality of the match will depend on how much the desired signal "looks" like the wavelet basis in the first place. There is still a need to match an orthonormal wavelet directly to a desired signal, with no presuppositions on its shape.

4.6 Biorthogonal Wavelets: The Lifting Scheme

Sweldens [32] developed a scheme for characterizing all biorthogonal filter sets that are derivable from any existing biorthogonal filter set. A biorthogonal scaling function, $\phi(x)$, generates an MRA $\{V_j\}$ and has as its associated wavelet, $\psi(x)$. The dual scaling function, $\tilde{\phi}(x)$ generates a different MRA, $\{\tilde{V}_j\}$, and has as its associated wavelet, $\tilde{\psi}(x)$ such that,

$$\langle \tilde{\phi}_{j,k}, \psi_{j,\ell} \rangle = \langle \phi_{j,k}, \tilde{\psi}_{j,\ell} \rangle = 0 \tag{4.49}$$

$$\langle \tilde{\phi}_{j,k}, \phi_{j,\ell} \rangle = \langle \tilde{\psi}_{j,k}, \psi_{j,\ell} \rangle = \delta_{k,\ell}. \tag{4.50}$$

Each of the functions, ϕ, ψ, $\tilde{\phi}$, and $\tilde{\psi}$ satisfy their own 2-scale relation of the form (3.88) and (3.89) where the respective generating sequences, h, g, $\tilde{h}$, and $\tilde{g}$, are related by the following expressions,

$$\tilde{G}(\omega) = e^{-i\omega}\overline{H(\omega + \pi)} \tag{4.51}$$

$$G(\omega) = e^{-i\omega}\overline{\tilde{H}(\omega + \pi)} \tag{4.52}$$

where $H(\omega)$, $G(\omega)$, $\tilde{H}(\omega)$, and $\tilde{G}(\omega)$ are the Fourier transforms of h_k, g_k, $\tilde{h}_k$, and $\tilde{g}_k$, respectively. Furthermore, in order to guarantee perfect reconstruction,

$$\overline{H(\omega)}\tilde{H}(\omega) + \overline{H(\omega + \pi)}\tilde{H}(\omega + \pi) = 1. \tag{4.53}$$

Sweldens proves that for a fixed ϕ and its associated h, if there are two finite dual filters, $\tilde{h}$ and $\tilde{h}^0$, both biorthogonal to h, then the two dual filters are related by the following frequency domain expression:

$$\tilde{H}(\omega) = \tilde{H}^0(\omega) + e^{-i\omega}\overline{H(\omega + \pi)S(2\omega)} \tag{4.54}$$

where $S(\omega)$ is a trigonometric polynomial [32]. Sweldens goes on to prove the converse, that if one of the dual filters is biorthogonal to h and they are related by (4.54), then the other is biorthogonal to h as well.

Therefore, (4.54) can be used to design new biorthogonal filters from existing ones where the degrees of freedom in the design reside in the trigonometric polynomial, $S(\omega)$. The design technique given in the following theorem is called the "Lifting Scheme" because it lifts the properties of one pair of biorthogonal filters in order to find another [32].

Theorem 3 (Lifting Scheme) *[32] Take an initial set of biorthogonal filters* $\{h, \tilde{h}^0, g^0, \tilde{g}\}$. *Then a new set of biorthogonal filters* $\{h, \tilde{h}, g, \tilde{g}\}$ *can be found by*

$$\tilde{H}(\omega) = \tilde{H}^0(\omega) + \tilde{G}(\omega)\overline{S(2\omega)} \tag{4.55}$$

$$\tilde{G}(\omega) = G^0(\omega) - H(\omega)S(2\omega). \tag{4.56}$$

The proof of this theorem can be checked quite easily. Since $\{h, \tilde{h}^0, g^0, \tilde{g}\}$ are a biorthogonal set of filters, they must satisfy (4.51), (4.52) and (4.53). Substituting for $\tilde{h}^0$ and g^0 in (4.52) and (4.53) using (4.55) and (4.56) gives expressions for $\{h, \tilde{h}, g, \tilde{g}\}$ that satisfy (4.51)–(4.53).

Theorem 3 can be applied to a wavelet by substituting (4.55) and (4.56) into the 2-scale relations for the wavelet in the frequency domain,

$$\begin{aligned}
\Psi(\omega) &= G\left(\frac{\omega}{2}\right)\Phi\left(\frac{\omega}{2}\right) \\
&= \left[G^0\left(\frac{\omega}{2}\right) - S(\omega)H\left(\frac{\omega}{2}\right)\right]\Phi\left(\frac{\omega}{2}\right) \\
&= G^0\left(\frac{\omega}{2}\right)\Phi\left(\frac{\omega}{2}\right) - S(\omega)H\left(\frac{\omega}{2}\right)\Phi\left(\frac{\omega}{2}\right) \\
&= G^0\left(\frac{\omega}{2}\right)\Phi\left(\frac{\omega}{2}\right) - S(\omega)\Phi(\omega)
\end{aligned} \tag{4.57}$$

which in the space domain is given as

$$\psi(x) = 2\sum_{k=-\infty}^{\infty} g_k^0 \phi(2x-k) - \sum_{k=-\infty}^{\infty} s_k \phi(x-k). \tag{4.58}$$

This expression for $\psi(x)$ can be used to find the optimal s_k with respect to the error between $\psi(x)$ and a desired signal, $f(x)$. Once again, however, one must have a pre-defined biorthogonal filter set before proceeding with the adaptive design. Furthermore, for a set of biorthogonal filters, the family of filters that can be "lifted" is not complete, so the choice of biorthogonal filters from which one starts is very important.

Chapter 5

Matching a Wavelet to a Signal

Using the mathematical construct of the orthonormal multiresolution analysis (MRA), an algorithm for finding a wavelet matched to a desired signal will be developed. The technique performs the matching in the frequency domain on the magnitude and phase independently of one another. This technique is different from the techniques outlined in Chapter 4 because it presumes nothing about an existing MRA, or existing wavelets. Instead, it assumes the wavelets to be bandlimited, and uses the *conditions* on an orthonormal MRA and the desired signal itself to find the "closest" orthonormal wavelet. However, once the algorithm is developed for the orthonormal MRA case, it will be shown that the bandlimit conditions can be relaxed so that the matched wavelet no longer generates an orthonormal MRA, but rather a frame, thereby providing much more flexibility in its application.

5.1 Motivation: Signal Detection

Wavelet transforms applied to multiresolution analyses of signals produce outputs similar in theory to those of matched filters[33]. In order to maximize the output of the matched filter bank, it is necessary to design a wavelet that "matches" the signal of interest. This approach can be justified by applying matched filter theory to the wavelet decomposition equations. The projection equation for the detail functions, given in (3.30), is an inner product integral and can be rewritten in the frequency domain by

way of Parseval's Identity:[10]

$$d_k^j = \langle f(x), \psi_{j,k} \rangle = \langle F(\omega), \Psi_{j,k}(2^j\omega) \rangle \tag{5.1}$$

where $\Psi_{j,k}(2^j\omega) = 2^{\frac{j}{2}} e^{-i2^j\omega k}\Psi(2^j\omega)$, is the Fourier transform of $\psi_{j,k}(x)$. The energy of d_k^j at a particular scale, j_0, and translation, k_0, is given by its squared magnitude

$$|d_{k_0}^{j_0}|^2 = |\langle F(\omega), \Psi_{j_0,k_0}(2^{j_0}\omega) \rangle|^2. \tag{5.2}$$

Applying Schwarz' inequality to the right side of (5.2) gives

$$|\langle F(\omega), \Psi_{j_0,k_0}(2^{j_0}\omega) \rangle|^2 \leq \langle F(\omega), F(\omega) \rangle \langle \Psi_{j_0,k_0}(2^{j_0}\omega), \Psi_{j_0,k_0}(2^{j_0}\omega) \rangle \tag{5.3}$$

where the equality holds for

$$F(\omega) = K\Psi_{j_0,k_0}(2^{j_0}\omega). \tag{5.4}$$

Therefore, $|d_{k_0}^{j_0}|^2$ is maximized when $f(x) = K\psi_{j_0,k_0}$. Rewriting (5.4) in terms of amplitude and phase gives

$$|F(\omega)|e^{i\theta_F(\omega)} = K2^{\frac{j_0}{2}} \left|\Psi\left(2^{j_0}\omega\right)\right| e^{i(\theta_\Psi(2^{j_0}\omega) - 2^{j_0}\omega k_0)} \tag{5.5}$$

where $\theta_F(\omega)$ and $\theta_\Psi(\omega)$ are the phase of $F(\omega)$ and $\Psi(\omega)$, respectively. If $f(x)$ matches exactly with an orthonormal wavelet, then $d_k^j = \delta_{k,k_0} \cdot \delta_{j,j_0}$ and the decomposition produces only 1 coefficient at (j_0, k_0)[33]. As the match moves away from being perfect, the decomposition begins to distribute the energy about (j_0, k_0) which according to (5.2) and (5.3) is still the maximum. Given the condition for a maximum projection coefficient at (j_0, k_0) in (5.5), the problem at hand is to develop a method for matching the complex spectrum of the wavelet to that of the desired signal while maintaining the conditions for an orthonormal MRA. However, because the conditions for orthonormality are on the spectrum amplitude (Poisson summation) only, the algorithm matches the spectrum amplitudes and group delays independently. While this approach is not ideal from an optimization standpoint, it will be shown that it still leads to good matching wavelets.

A difficulty in matching the wavelet spectrum directly to that of the desired signal is that the conditions on an orthonormal MRA are not if and only if conditions. For instance, if $\phi_{j,k}$ is orthonormal and

generates an MRA, then $\psi_{j,k}$ is also orthonormal. The converse is not true[13][24]. Therefore, in developing the matching algorithm it is necessary to propagate the conditions for an orthonormal MRA from the 2-scale sequence and scaling function to the wavelet, match the wavelet to the desired signal under those conditions, and then calculate the scaling function and 2-scale sequence always guaranteeing that the conditions for an orthonormal MRA are satisfied.

5.2 Orthonormal MRAs

The detailed development of orthonormal wavelet bases and multiresolution analyses (MRAs) in Chapter 3 will be summarized here for convenience. Recall that in an orthonormal MRA, a signal, $f(x) \in V_{-1}$, is decomposed into a series of detail functions, $\{g_j(x)\}$ $j = \{0, 1, \ldots, J\}$, and a residual low resolution approximation, $f_J(x)$, such that

$$f(x) = \sum_{j=0}^{J} g_j(x) + f_J(x). \tag{5.6}$$

The decomposition is done by projecting $f^{j-1}(x)$ onto two orthogonal subspaces, V_j and W_j, where $V_{j-1} = V_j \dot{+} W_j$ and $(\dot{+})$ is the direct sum operator. The projection produces $f^j(x) \in V_j$, a low resolution approximation of $f(x)$, and $g^j(x) \in W_j$, the detail lost in going from $f^{j-1}(x)$ to $f^j(x)$. The orthonormal bases of W_j and V_j are given by $\psi_{j,k} = 2^{-j/2}\psi(2^{-j}x - k)$ and $\phi_{j,k} = 2^{-j/2}\phi(2^{-j}x - k)$, respectively; $\psi(x)$ is the mother wavelet and $\phi(x)$ is the scaling function where

$$\int \psi(x)dx = 0 \Longleftrightarrow \Psi(0) = 0 \tag{5.7}$$

$$\int \phi(x)dx = 1 \Longleftrightarrow \Phi(0) = 1 \tag{5.8}$$

and $\Phi(\omega)$ and $\Psi(\omega)$ are the Fourier Transform of $\phi(x)$ and $\psi(x)$, respectively. The projection equations are given as

$$g_j(x) = \sum_{k=-\infty}^{\infty} d_k^j 2^{-\frac{j}{2}} \psi(2^{-j}x - k) \tag{5.9}$$

$$d_k^j = \langle f_{j-1}(x), \psi_{j,k} \rangle \tag{5.10}$$

$$f_j(x) = \sum_{k=-\infty}^{\infty} c_k^j 2^{-\frac{j}{2}} \phi(2^{-j}x - k) \tag{5.11}$$

$$c_k^j = \langle f_{j-1}(x), \phi_{j,k} \rangle \tag{5.12}$$

where d_k^j and c_k^j are the projection coefficients and $\langle \cdot, \cdot \rangle$ is the L^2 inner product. The nested sequence of subspaces, $\{V_j\}$, constitutes the multiresolution analysis.

In order for the MRA to be orthonormal: 1) $\psi_{j,k}$ and $\phi_{j,k}$ must be orthonormal bases of W_j and V_j, respectively; 2) $W_j \perp W_k$, for $j \neq k$; and 3) $W_j \perp V_j$, which leads to the following conditions on ψ and ϕ [10][20]:

$$\langle \phi_{j,k}, \phi_{j,m} \rangle = \delta_{k,m} \tag{5.13}$$

$$\langle \phi_{j,k}, \psi_{j,m} \rangle = 0 \tag{5.14}$$

$$\langle \psi_{j,k}, \psi_{\ell,m} \rangle = \delta_{j,\ell} \cdot \delta_{k,m}. \tag{5.15}$$

The Fourier transform of (5.13) gives the Poisson summation, which is 1 for all ω when the integer translates of $\phi(x)$ are orthonormal,

$$\sum_{m=-\infty}^{\infty} |\Phi(\omega + 2\pi m)|^2 = 1. \tag{5.16}$$

Since $\phi(x) \in V_0 \subset V_{-1}$ and $\psi(x) \in W_0 \subset V_{-1}$, they can be represented as a linear combination of the basis of V_{-1}:

$$\phi(x) = 2 \sum_{k=-\infty}^{\infty} h_k \phi(2x - k) \tag{5.17}$$

$$\psi(x) = 2 \sum_{k=-\infty}^{\infty} g_k \phi(2x - k) \tag{5.18}$$

given in the frequency domain by

$$\Phi(\omega) = H\left(\frac{\omega}{2}\right) \Phi\left(\frac{\omega}{2}\right) \tag{5.19}$$

$$\Psi(\omega) = G\left(\frac{\omega}{2}\right) \Phi\left(\frac{\omega}{2}\right). \tag{5.20}$$

For orthonormal MRAs, the sequences h_k and g_k in (5.17) and (5.18) are quadrature mirror filters (QMF) and have the following properties [23][35]:

$$|H(\omega)|^2 + |G(\omega)|^2 = 1 \tag{5.21}$$

$$H(\omega)\overline{H(\omega + \pi)} + G(\omega)\overline{G(\omega + \pi)} = 0 \tag{5.22}$$

where $H(\omega)$ and $G(\omega)$ are the Fourier transforms of h_k and g_k, respectively, and are therefore both 2π-periodic.

5.3 Matching a Wavelet to a Signal

5.3.1 Finding the scaling function from a wavelet

Before developing the algorithm for finding the matched wavelet, a means of deriving the scaling function from the mother wavelet must be derived [7, 8]. Finding the wavelet from the scaling function is simple using (5.18), however, it is not invertible. In order to derive an expression for $|\Phi|$ in terms of $|\Psi|$, the following conditions are required [20]:

$$g_k = (-1)^k h_{1-k} \tag{5.23}$$

$$\Phi(0) = 1 \tag{5.24}$$

$$\langle \phi_{j,k}, \phi_{j,m} \rangle = \delta_{k,m} \tag{5.25}$$

$$\phi(x) = 2 \sum_{k=-\infty}^{\infty} h_k \phi(2x - k). \tag{5.26}$$

Condition (5.23) simply guarantees (5.22) to be satisfied always. Conditions (5.24)-(5.26) are required for $\phi(x)$ to generate an orthonormal MRA, thereby satisfying equations (5.13)-(5.22)[20].

Substituting (5.19) and (5.20) into (5.21) gives a relationship between $|\Phi(\omega)|$ and $\Psi(\omega)|$ in the context of an MRA [13]:

$$|\Phi(\omega)|^2 = |\Psi(2\omega)|^2 + |\Phi(2\omega)|^2. \tag{5.27}$$

Since the matching algorithm is performed on sampled data (in the frequency domain), there is a need to develop an equation for finding the sampled scaling function spectrum from the sampled wavelet spectrum.

Theorem 4 (Finding $|\Phi(k)|$ from $|\Psi(k)|$) *In an orthonormal MRA, let $\Phi(n\Delta\omega)$ and $\Psi(n\Delta\omega)$ be the sampled scaling function and wavelet spectra, respectively, with sample spacing $\Delta\omega = \pi/2^\ell$. Any sample of $|\Phi|$ at $\omega = n\pi/2^\ell$ can be expressed by the following recursive equation:*

$$\left|\Phi\left(\frac{\pi n}{2^\ell}\right)\right|^2 = \left|\Phi\left(\frac{\pi n}{2^{\ell-1}}\right)\right|^2 + \left|\Psi\left(\frac{\pi n}{2^{\ell-1}}\right)\right|^2 \qquad \text{for } n \neq 0 \tag{5.28}$$

which leads to the following closed form solution

$$\left|\Phi\left(\frac{\pi n}{2^\ell}\right)\right|^2 = \sum_{p=0}^{\ell} \left|\Psi\left(\frac{2\pi n}{2^p}\right)\right|^2 \qquad \text{for } n \neq 0. \tag{5.29}$$

Furthermore, (5.28) implies

$$|\Psi(4\pi k)| = 0 \qquad \textit{for all } k \in \mathbb{Z}. \tag{5.30}$$

Proof. Substituting $\omega = \pi n$ in (5.27) gives

$$|\Phi(\pi n)|^2 = |\Phi(2\pi n)|^2 + |\Psi(2\pi n)|^2. \tag{5.31}$$

However, since $\sum |\Phi(\omega + 2\pi n)|^2 = 1$ for orthonormal MRAs, and $\Phi(0) = 1$, and $\Psi(0) = 0$ then

$$|\Phi(2\pi n)| = \begin{cases} 1 & \text{for } n = 0 \\ 0 & \text{for } n \neq 0 \end{cases} \tag{5.32}$$

and (5.31) can be rewritten as

$$|\Phi(\pi n)| = \begin{cases} 1 & \text{for } n = 0 \\ |\Psi(2\pi n)| & \text{for } n \neq 0 \end{cases}. \tag{5.33}$$

So, at integer multiples of π, $|\Phi|$ can be computed directly from values of $|\Psi|$. Furthermore, (5.32) and (5.33) imply $|\Psi(4\pi n)| = 0$. Substituting for $\omega = \pi n/2$ in (5.27) gives

$$\left|\Phi\left(\frac{\pi n}{2}\right)\right|^2 = |\Phi(\pi n)|^2 + |\Psi(\pi n)|^2 \qquad \text{for } n \neq 0. \tag{5.34}$$

At integer multiples of $\pi/2$, $|\Phi|$ can be computed from values of $|\Psi|$ and the previously calculated values of $|\Phi|$. Repeated substitutions leads to the following closed form solution:

$$\left|\Phi\left(\frac{\pi n}{2^\ell}\right)\right|^2 = \sum_{p=0}^{\ell} \left|\Psi\left(\frac{2\pi n}{2^p}\right)\right|^2 \qquad \text{for } n \neq 0. \tag{5.35}$$

If $|\Psi(k\Delta\omega_\Psi)|$ has a sample spacing of $\Delta\omega_\Psi = 2\pi/2^M$, then by (5.29), $|\Phi(k\Delta\omega_\phi)|$ has a minimum sample spacing of $\Delta\omega_\Psi = 2\pi/2^{M+1}$ and ℓ can take on values of

$$\ell = \{0, 1, \ldots, M\}. \tag{5.36}$$

□

Interestingly, as $\ell \to \infty$, equation (5.29) approaches Daubechies' result for continuous ω [13],

$$|\Phi(\omega)|^2 = \sum_{p=0}^{\infty} |\Psi(2^{p+1}\omega)|^2 \qquad \text{for } \omega \neq 0. \tag{5.37}$$

However, the beauty of (5.29) over (5.37) is that the discrete form yields an exact result for a discrete spectrum with a finite number of recursive steps.

5.3.2 Properties of the wavelet spectrum amplitude

The next step is to derive constraints on $|\Psi|$ that are necessary and sufficient to guarantee $\phi_{j,k}$ is an orthonormal basis of V_j[7, 8].

Theorem 5 (Guaranteeing Orthonormality) *The following condition on $|\Psi(\omega)|$ is both necessary and sufficient to guarantee that $\langle \phi_{j,k}, \phi_{j,m} \rangle = \delta_{k,m}$, where $\phi_{j,k}$ is derived from $|\Phi(\omega)|$:*

$$\sum_{m=-\infty}^{\infty} \sum_{n=0}^{\infty} \left| \Psi\left((2^{n+1}\omega + 2\pi m) \right) \right|^2 = 1. \tag{5.38}$$

Proof. See Appendix A.

While (5.29) and (5.38) provide a method for deriving an orthonormal function, $\phi(x)$, from a given wavelet, there is no guarantee that $\phi(x)$ generates an MRA[13][24]. The only condition remaining to be incorporated is the 2-scale relation in (5.26) [8]. In order for $\phi(x)$ to generate an MRA, it must satisfy its 2-scale relation [12][13][24], which given in the frequency domain is

$$\Phi(\omega) = H\left(\frac{\omega}{2}\right) \Phi\left(\frac{\omega}{2}\right). \tag{5.39}$$

Repeated substitution of this recursive equation gives

$$\Phi(\omega) = H\left(\frac{\omega}{2}\right) H\left(\frac{\omega}{4}\right) H\left(\frac{\omega}{8}\right) \cdots \tag{5.40}$$

where $H(\omega)$ is the Fourier transform of the discrete signal, h_k, and is therefore, 2π-periodic. Equation (5.40) indicates that there must be a certain structure in ϕ in order for it to be a scaling function. Incorporating the infinite product into the conditions developed thus far would be very difficult. A simple way to guarantee that (5.40) is satisfied is to assume $\Phi(\omega)$ is bandlimited [8]. However, one is not free to choose any bandlimits.

Theorem 6 (Bandlimited Φ) *In a multiresolution analysis, the spectrum of a bandlimited scaling function, $\Phi(\omega)$, has maximum support given by*

$$|\omega| \leq \frac{4\pi}{3}. \tag{5.41}$$

Proof. See Appendix B.

From (5.20), it is clear that a bandlimited scaling function that generates an orthonormal MRA gives rise to a bandlimited wavelet.

Corollary 7 (Bandlimited Ψ) *In an orthonormal MRA with a bandlimited scaling function, the corresponding orthonormal wavelet has a maximum bandlimit of*

$$\frac{2\pi}{3} \leq |\omega| \leq \frac{8\pi}{3}. \tag{5.42}$$

Proof. See Appendix C.

It is interesting to note that the bandlimits derived above are identical to those of Meyer's wavelet[26]. However, what has been derived here are the maximum bandlimits for not only Meyer's wavelet but any bandlimited, orthonormal wavelet.

In order to complete the groundwork for the spectrum amplitude matching algorithm, a set of equations for sampled spectra, similar to Theorem 5 and Corollary 7 is needed.

Theorem 8 (Guaranteeing an Orthonormal MRA) *Let $Y(k) = |\Psi(k\Delta\omega)|^2$, $k \in \mathbb{Z}$, where $\Delta\omega = 2\pi/2^M$. The necessary and sufficient condition on Y to guarantee that $|\Phi(n)|$, found in Theorem 4, generates an orthonormal MRA is given as follows:*

$$\sum_{m=-\infty}^{\infty} \sum_{p=0}^{\ell} Y\left(\frac{2^M}{2^p}(n + 2^{\ell+1}m)\right) = 1 \tag{5.43}$$

$$2^{M-1}/3 < \left|\frac{2^M}{2^p}(n + 2^{\ell+1}m)\right| < 2^{M+2}/3 \qquad \ell = \{0, 1, \ldots, M\}. \tag{5.44}$$

Proof. See Appendix D.

Because the wavelets being designed are assumed to be real, the magnitude of the wavelet spectrum is even, $|\Psi(\omega)| = |\Psi(-\omega)|$, and only the spectra for positive frequency indices, k, in the passband need be matched. The conditions in Theorem 8 for $k > 0$ generate a set of L linear equality constraints in $Y(k)$ of the form

$$\sum_{i=1}^{L} \alpha_{ik} Y(k) = 1 \qquad \text{for } k = \{\lceil 2^M/3 \rceil, \ldots, \lfloor 2^{M+2}/3 \rfloor\} \tag{5.45}$$

where $\alpha_{ik} \in \{0, 1, 2\}$. Condition (5.45) can be expressed in vector notation as

$$\mathbf{AY} = \mathbf{1} \tag{5.46}$$

where $\mathbf{A}$ is a $L \times 2^M$ matrix given by

$$\mathbf{A} = \{\alpha_{ij} \in \{0, 1, 2\}; i = 1, \ldots, L; j = 1, \ldots, 2^M\} \tag{5.47}$$

and $\mathbf{1}$ is a $L \times 1$ vector given by

$$\mathbf{1}^T = \{1 \quad 1 \quad \ldots \quad 1\}. \tag{5.48}$$

5.3.3 Matching Spectrum Amplitudes

By virtue of the limits given in (5.42), the desired signal must be dilated in such a way that the energy in this passband is a maximum. This dilated spectrum, $F(\omega)$, is the starting point for the matching algorithm.

Theorem 9 (Matched Wavelet Amplitude) *Let* $\mathbf{W}$ *and* $\mathbf{Y}$ *be vectors containing the samples of* $|F(k\Delta\omega)|^2$ *and* $|\Psi(k\Delta\omega)|^2$, *respectively, in the passband:*

$$\mathbf{W} = \left\{|F(k\Delta\omega)|^2;\, k = \left\lceil 2^M/3 \right\rceil, \ldots, \left\lfloor 2^{M+2}/3 \right\rfloor\right\} \tag{5.49}$$

$$\mathbf{Y} = \left\{|\Psi(k\Delta\omega)|^2;\, k = \left\lceil 2^M/3 \right\rceil, \ldots, \left\lfloor 2^{M+2}/3 \right\rfloor\right\} \tag{5.50}$$

where $F(\omega)$ *is the spectrum of the dilated signal being matched and* $\Psi(\omega)$ *is the matched wavelet spectrum. If the error to be minimized is given by*

$$E = \frac{(\frac{1}{a}\mathbf{W} - \mathbf{Y})^T(\frac{1}{a}\mathbf{W} - \mathbf{Y})}{\frac{1}{a^2}\mathbf{W}^T\mathbf{W}} \tag{5.51}$$

then the optimal wavelet power spectrum is given by the following expression

$$\mathbf{Y} = \frac{1}{a}\mathbf{W} + \mathbf{A}^T(\mathbf{A}\mathbf{A}^T)^{-1}(\mathbf{1} - \frac{1}{a}\mathbf{A}\mathbf{W}) \tag{5.52}$$

where

$$a = \frac{\mathbf{1}^T(\mathbf{A}\mathbf{A}^T)^{-1}\mathbf{A}\mathbf{W}}{\mathbf{1}^T(\mathbf{A}\mathbf{A}^T)^{-1}\mathbf{1}} \tag{5.53}$$

and $(\mathbf{A}\mathbf{A}^T)$ *is full rank. The match error is given by*

$$E = \frac{(\mathbf{1} - \frac{1}{a}\mathbf{A}\mathbf{W})^T(\mathbf{A}\mathbf{A}^T)^{-1}(\mathbf{1} - \frac{1}{a}\mathbf{A}\mathbf{W})}{\frac{1}{a^2}\mathbf{W}^T\mathbf{W}}. \tag{5.54}$$

The resultant wavelet is orthonormal, and the scaling function it generates by way of (5.29) generates an orthonormal MRA.

Proof. See Appendix E.

Notice that the error, E, in (5.54) has the form of a Mahalonobis distance, where $(\mathbf{W}^T\mathbf{W}/a^2)\mathbf{A}\mathbf{A}^T$ acts like a covariance matrix [28]. This implies that the solution is "closest" to the desired signal spectrum where the distance measure is given in (5.51). The error in the match is a function of the deviation, or distance, of $\mathbf{AW}$ from $\mathbf{1}$. If $\mathbf{AW}$ is already $\mathbf{1}$, then the Poisson summation of $F(\omega)$ is 1, $f(x)$ is an orthonormal wavelet and $\phi(x)$, calculated in (5.29), generates an orthonormal MRA. As $F(\omega)$ moves away from being orthonormal, $\mathbf{AW}$ moves away from $\mathbf{1}$ and the error of the match increases. However, the resultant wavelet is still the closest [minimum distance as defined by (5.51)] orthonormal wavelet to $f(x)$.

Note: This amplitude matching algorithm produces a sampled wavelet that in the discrete domain satisfies all the properties of an orthonormal wavelet. While the Poisson summation for the resultant scaling function and wavelet are shown to be 1 *at the samples of* ω*, there can be nothing said about the values of the Poisson summation between the discrete samples. Therefore, the resultant wavelet spectrum from Theorem 9 is a discrete approximation to a continuous orthonormal wavelet*

The first half of the problem posed by (5.5) has been solved, that of finding the optimal wavelet spectrum amplitude with respect to the input spectrum. The next two sections develop the algorithm for matching the wavelet phase to that of the desired signal.

5.3.4 Properties of the wavelet spectrum phase

It would be convenient to simply set the phase of Ψ to the phase of the desired signal spectrum, F, thereby cancelling the complex exponentials in (5.5). However, just as in the previous section where it was shown that Ψ has specific constraints on its amplitude, here it will be shown that Ψ has specific

constraints on the structure of its phase as well [8]. By repeated substitutions of the equations in (5.19) and (5.20) and the Fourier Transform of (5.23), $G(\omega) = e^{-i\omega}\overline{H(\omega+\pi)}$, one gets the following infinite products [10][12][23],

$$\Phi(\omega) = \prod_{m=1}^{\infty} H\left(\frac{\omega}{2^m}\right) \tag{5.55}$$

$$\Psi(\omega) = e^{-i\frac{\omega}{2}}\overline{H\left(\frac{\omega}{2}+\pi\right)}\prod_{m=2}^{\infty} H\left(\frac{\omega}{2^m}\right) \tag{5.56}$$

where $H(\omega)$ is 2π-periodic. Taking the phase of both sides gives

$$\theta_\Phi(\omega) = \sum_{m=1}^{\infty} \theta_H\left(\frac{\omega}{2^m}\right) \tag{5.57}$$

$$\theta_\Psi(\omega) = -\frac{\omega}{2} - \theta_H\left(\frac{\omega}{2}+\pi\right) + \sum_{m=2}^{\infty} \theta_H\left(\frac{\omega}{2^m}\right) \tag{5.58}$$

where θ_Φ, θ_Ψ, and θ_H are the phases of Φ, Ψ, and H, respectively, and $\theta_H(\omega)$ is 2π-periodic. The derivatives of (5.57) and (5.58) give the negative of their group delays.

$$\Lambda_\Phi(\omega) = \sum_{m=1}^{\infty} 2^{-m}\lambda\left(\frac{\omega}{2^m}\right) \tag{5.59}$$

$$\Lambda_\Psi(\omega) = -\frac{1}{2} - \frac{1}{2}\lambda\left(\frac{\omega}{2}+\pi\right) + \sum_{m=2}^{\infty} 2^{-m}\lambda\left(\frac{\omega}{2^m}\right) \tag{5.60}$$

where $\Lambda_\Phi(\omega) = d\theta_\Phi(\omega)/d\omega$ and $\Lambda_\Psi = d\theta_\Psi(\omega)/d\omega$, and $\lambda(\omega) = d\theta_H(\omega)/d\omega$ is 2π-periodic. Equation (5.60) can be simplified further by letting $\Gamma_\Psi(\omega) = \Lambda_\Psi + 1/2$ so that

$$\Gamma_\Psi(\omega) = -\frac{1}{2}\lambda\left(\frac{\omega}{2}+\pi\right) + \sum_{m=2}^{\infty} 2^{-m}\lambda\left(\frac{\omega}{2^m}\right). \tag{5.61}$$

The wavelet's group delay, $\Gamma_\Psi(\omega)$, will be matched to the group delay of the desired signal, $\Gamma_F(\omega)$. Before proceeding, it is important to note some of the properties of the group delays of Φ, Ψ and H.

Theorem 10 (Properties of Λ_Φ, Λ_Ψ and λ) *Let $\Lambda_\Phi(\omega) = d\theta_\Phi(\omega)/d\omega$ and $\Lambda_\Psi(\omega) = d\theta_\Psi(\omega)/d\omega$, where $\theta_\Phi(\omega)$ and $\theta_\Psi(\omega)$ are the phase functions of $\Phi(\omega)$ and $\Psi(\omega)$, respectively. Let $\lambda(\omega) = d\theta_H(\omega)/d\omega$ where $\theta_H(\omega)$ is the 2π-periodic phase of $H(\omega)$. Then $\Lambda_\Phi(\omega)$, $\Lambda_\Psi(\omega)$ and $\lambda(\omega)$ have the following properties:*

$$\Lambda_\Phi(\omega) = \Lambda_\Phi(-\omega) \tag{5.62}$$

$$\Lambda_\Psi(\omega) = \Lambda_\Psi(-\omega) \tag{5.63}$$

$$\lambda(\omega) = \lambda(-\omega) \tag{5.64}$$

$$\int_{-\infty}^{\infty} \Lambda_\Phi(\omega)d\omega = \frac{1}{2\pi}\int_{-\pi}^{\pi} \lambda(\omega)d\omega = \overline{\lambda} \quad \textit{where } \overline{\lambda} \in \mathbb{Z} \tag{5.65}$$

$$\int_{-\infty}^{\infty} \Lambda_\Psi(\omega)d\omega = -\frac{1}{2} \tag{5.66}$$

and therefore,

$$\int_{-\infty}^{\infty} \Gamma_\Psi(\omega)d\omega = 0. \tag{5.67}$$

Proof. See Appendix F.

The mean group delay of a signal provides information about the translation properities of that signal. For instance, the mean group delay of H, $\overline{\lambda}$, can take on values of $\overline{\lambda} = \pm m$ for $m \in \mathbb{Z}$, since h_k can only shift in unit increments. Likewise, $\phi(x)$ can only shift by unit increments, since its mean group delay is also $\overline{\lambda}$. However, $\psi(x)$ is fixed on the x-axis since its mean group delay is a constant and independent of $\overline{\lambda}$, that is, shifts in h_k. These same shifting relationships between $\phi(x)$ and $\psi(x)$ can be derived from (5.17) and (5.18).

Matching the group delay of a desired signal to the group delay of a wavelet given in (5.61) cannot be done in the same manner as the amplitude matching since there are additional periodicity constraints on $\lambda(\omega)$. Furthermore, there is still the problem of finding the phase of Φ from the phase of Ψ. To solve both problems, one period of $\lambda(\omega)$ is modeled as a polynomial of order R [8]. Because $\lambda(\omega)$ is an even function (Theorem 10), the polynomial has only even exponents

$$\lambda_T(\omega) = \sum_{r=0}^{R/2} c_r \omega^{2r} \Pi(\frac{\omega}{2\pi}) \tag{5.68}$$

where c_r are the coefficients of the polynomial and $\Pi(\omega)$ is the "rect" function defined as

$$\Pi(\omega) = \begin{cases} 1 & -\frac{1}{2} \leq \omega < \frac{1}{2} \\ 0 & \text{elsewhere.} \end{cases} . \tag{5.69}$$

Now express $\lambda(\omega)$ as

$$\lambda(\omega) \quad = \quad \sum_{k=-\infty}^{\infty} \lambda_T(\omega - 2\pi k)$$

$$= \sum_{k=-\infty}^{\infty} \sum_{r=0}^{R/2} c_r(\omega - 2\pi k)^{2r} \Pi(\frac{\omega - 2\pi k}{2\pi}). \tag{5.70}$$

Like the amplitude matching algorithm, the phase matching algorithm is developed for discrete samples of the spectrum. Let $\Delta\omega = 2\pi/T$, and N be the number of samples in $F(n\Delta\omega)$. Equation (5.70) can be rewritten in discrete form as

$$\lambda(n) = \sum_{r=0}^{R/2} c_r \sum_{k=-P/2}^{P/2-1} (n - kT)^{2r} \Pi(\frac{n - kT}{T}) \tag{5.71}$$

where $P = N/T$ is the number of periods over N points and $-N/2 \leq n < N/2$. The discrete form for $\lambda(n)$ can now be written in vector notation as

$$\lambda = \mathbf{B}\mathbf{c} \tag{5.72}$$

where λ is a $N \times 1$ vector, $\mathbf{B}$ is a $N \times (R/2+1)$ matrix and $\mathbf{c}$ is a $(R/2+1) \times 1$ vector. The elements of $\mathbf{B}$ are given as

$$b_{n,r} = \sum_{k=-P/2}^{P/2-1} (n - kT)^{2r} \Pi(\frac{n - kT}{T}). \tag{5.73}$$

Substituting (5.72) into (5.59)–(5.61) gives a matrix equation for $\mathbf{\Lambda}_\Phi$, $\mathbf{\Lambda}_\Psi$, $\mathbf{\Gamma}_\Psi$,

$$\mathbf{\Lambda}_\Phi = \mathbf{D}_\Phi \mathbf{c} \tag{5.74}$$

$$\mathbf{\Lambda}_\Psi = -\frac{\Delta\omega}{2} + \mathbf{D}_\Psi \mathbf{c} \tag{5.75}$$

and

$$\mathbf{\Gamma}_\Psi = \mathbf{D}_\Psi \mathbf{c} \tag{5.76}$$

where

$$\mathbf{D}_\Phi = \sum_{m=1}^{\infty} 2^{-m} \mathbf{B}_{\frac{q}{2^m}} \tag{5.77}$$

and

$$\mathbf{D}_\Psi = -\frac{1}{2}\mathbf{B}_{\frac{q+T}{2}} + \sum_{m=2}^{\infty} 2^{-m} \mathbf{B}_{\frac{q}{2^m}} \tag{5.78}$$

and the elements of $\mathbf{B}_{\frac{q+T}{2}}$ and $\mathbf{B}_{\frac{q}{2^m}}$ are given in (5.73) where $n = (q+T)/2$ and $n = q/2^m$, respectively.

5.3.5 Matching Spectrum Phase

In this section, the expression for $\mathbf{\Gamma}_\Psi$ will be derived such that it is closest to the desired signal's group delay, $\mathbf{\Gamma}_F$, in a least squares sense and yet has the structure of (5.76) and (5.78). Let γ be the unweighted error to be minimized,

$$\gamma = \sum_{n=-N/2}^{N/2-1} (\Gamma_F(n) - \Gamma_\Psi(n))^2. \tag{5.79}$$

Since the wavelet phase need only match that of the desired signal in the passband, weight the error function by a normalized weighting function. Let $\Omega(n) = Y(n)/\sum Y(n)$, where $Y(n)$ are the elements of $\mathbf{Y}$ derived in Theorem 9. The weighted error function becomes

$$\begin{aligned} \gamma_\Omega &= \sum_{n=-N/2}^{N/2-1} [\Omega(n)(\Gamma_F(n) - \Gamma_\Psi(n))]^2 \\ &= \sum_{n=-N/2}^{N/2-1} \left[\Omega(n)(\Gamma_F(n) - \sum_{r=0}^{R/2} c_r d_{n,r})\right]^2 \end{aligned} \tag{5.80}$$

where $\{d_{n,r}\}$ are the elements of $\mathbf{D}_\Psi$ in (5.78). Rewriting (5.80) in vector notation gives

$$\gamma = (\bar{\mathbf{\Gamma}}_F - \bar{\mathbf{D}}_\Psi \mathbf{c})^T (\bar{\mathbf{\Gamma}}_F - \bar{\mathbf{D}}_\Psi \mathbf{c}) \tag{5.81}$$

where the elements of $\bar{\mathbf{\Gamma}}_F$ are the non-zero values of $\{\Omega(n)\Gamma_F(n)\}$ and the elements of $\bar{\mathbf{D}}_\Psi$ are the corresponding non-zero values of $\{\Omega(n)d_{n,r}\}$. The vector, $\hat{\mathbf{c}}$, which minimizes γ is found by setting $\nabla_c \gamma = 0$, giving

$$\hat{\mathbf{c}} = (\bar{\mathbf{D}}_\Psi^T \bar{\mathbf{D}}_\Psi)^{-1} \bar{\mathbf{D}}_\Psi^T \bar{\mathbf{\Gamma}}_F \tag{5.82}$$

where $\bar{\mathbf{D}}_\Psi^T \bar{\mathbf{D}}_\Psi$ is full rank. It follows that the group delay of the wavelet can be found by substituting (5.82) into (5.76),

$$\mathbf{\Gamma}_\Psi = \mathbf{D}_\Psi \hat{\mathbf{c}}. \tag{5.83}$$

Since $\hat{\mathbf{c}}$ in (5.82) gives the best estimate of $\mathbf{c}$, it can be substituted into (5.72), (5.75) and (5.74) to calculate the best estimates of λ, $\mathbf{\Lambda}_\Psi$ and $\mathbf{\Lambda}_\Phi$,

$$\lambda = \mathbf{B}\hat{\mathbf{c}} \tag{5.84}$$

$$\mathbf{\Lambda}_\Psi = \left(\mathbf{D}_\Psi \hat{\mathbf{c}} - \overline{\mathbf{D}_\Psi \hat{\mathbf{c}}}\right) - \frac{\Delta\omega}{2} \tag{5.85}$$

$$\mathbf{\Lambda}_\Phi = \mathbf{D}_\Phi \hat{\mathbf{c}} - \overline{\mathbf{D}_\Phi \hat{\mathbf{c}}} \tag{5.86}$$

where $\overline{\mathbf{D}_\Psi \hat{\mathbf{c}}}$ and $\overline{\mathbf{D}_\Phi \hat{\mathbf{c}}}$ are the means of $\mathbf{D}_\Psi \hat{\mathbf{c}}$ and $\mathbf{D}_\Phi \hat{\mathbf{c}}$, respectively. The means in (5.85) and (5.86) are subtracted so that $\mathbf{\Lambda}_\Psi$ and $\mathbf{\Lambda}_\Phi$ have the properties of Theorem 10. Both $\mathbf{\Lambda}_\Psi$ and $\mathbf{\Lambda}_\Phi$ can be summed to obtain the discrete phases of Φ and Ψ that when combined with the magnitudes from Theorem 9 give the full estimate of $\Phi(n\Delta\omega)$ and $\Psi(n\Delta\omega)$ which satisfy all conditions for an orthonormal MRA. The QMF filters, h and g, corresponding to the matched wavelet and its scaling function can be found using (5.19) and (5.20) and the inverse Fourier Transform. A flow chart of the complete algorithm, including both the amplitude and phase matching algorithms, is given in Figure 5.1.

5.4 Generating Matched Wavelet Frames

The wavelet design algorithm of Section 5.3 is based on the conditions for an orthonormal MRA and as a result, finds wavelets such that their associated scaling functions generate an orthonormal MRA. The condition in Section 5.3 that guarantees an MRA is the bandlimit condition on $\Phi(\omega)$ given in Theorem 6, which leads to the the bandlimit conditions on $\Psi(\omega)$ of Corollary 7. It is important to note that the matching algorithm given in Sections 5.3.3–5.3.5 does not depend on the specific bandlimits, but only the fact that they exist (that $\psi(x)$ is bandlimited).

This section shows that if the bandlimits of the wavelet spectrum are expanded beyond that of Corollary 7 and if $b \in \Re$, then the matching algorithm generates a dyadic wavelet. It will also be shown that if $b = nb_0$, that is, sampled with sample spacing b_0, then the resultant wavelet generates a frame of $L^2(\Re)$ and there is redundancy in the decomposition of the desired signal using the matched wavelet.

Theorem 11 (Matched Dyadic Wavelet) *Let $F(\omega)$ be the spectrum of an input signal. Let $\Psi(\omega)$ be the spectrum of a bandlimited wavelet such that $\Psi(\omega) \neq 0$ for $2\pi\alpha \leq |\omega| \leq 2\pi\beta$ and $\alpha < 1/3$, $\beta > 4/3$. Furthermore, let $\mathbf{W}$ and $\mathbf{Y}$ be vectors containing the samples of $|F(k\Delta\omega)|^2$ and $|\Psi(k\Delta\omega)|^2$, respectively, in the passband:*

$$\mathbf{W} = \left\{ |F(k\Delta\omega)|^2;\, k = \left\lceil 2^M \alpha \right\rceil, \ldots, \left\lfloor 2^M \beta \right\rfloor \right\} \tag{5.87}$$

$$\mathbf{Y} = \left\{ |\Psi(k\Delta\omega)|^2;\, k = \left\lceil 2^M \alpha \right\rceil, \ldots, \left\lfloor 2^M \beta \right\rfloor \right\}. \tag{5.88}$$

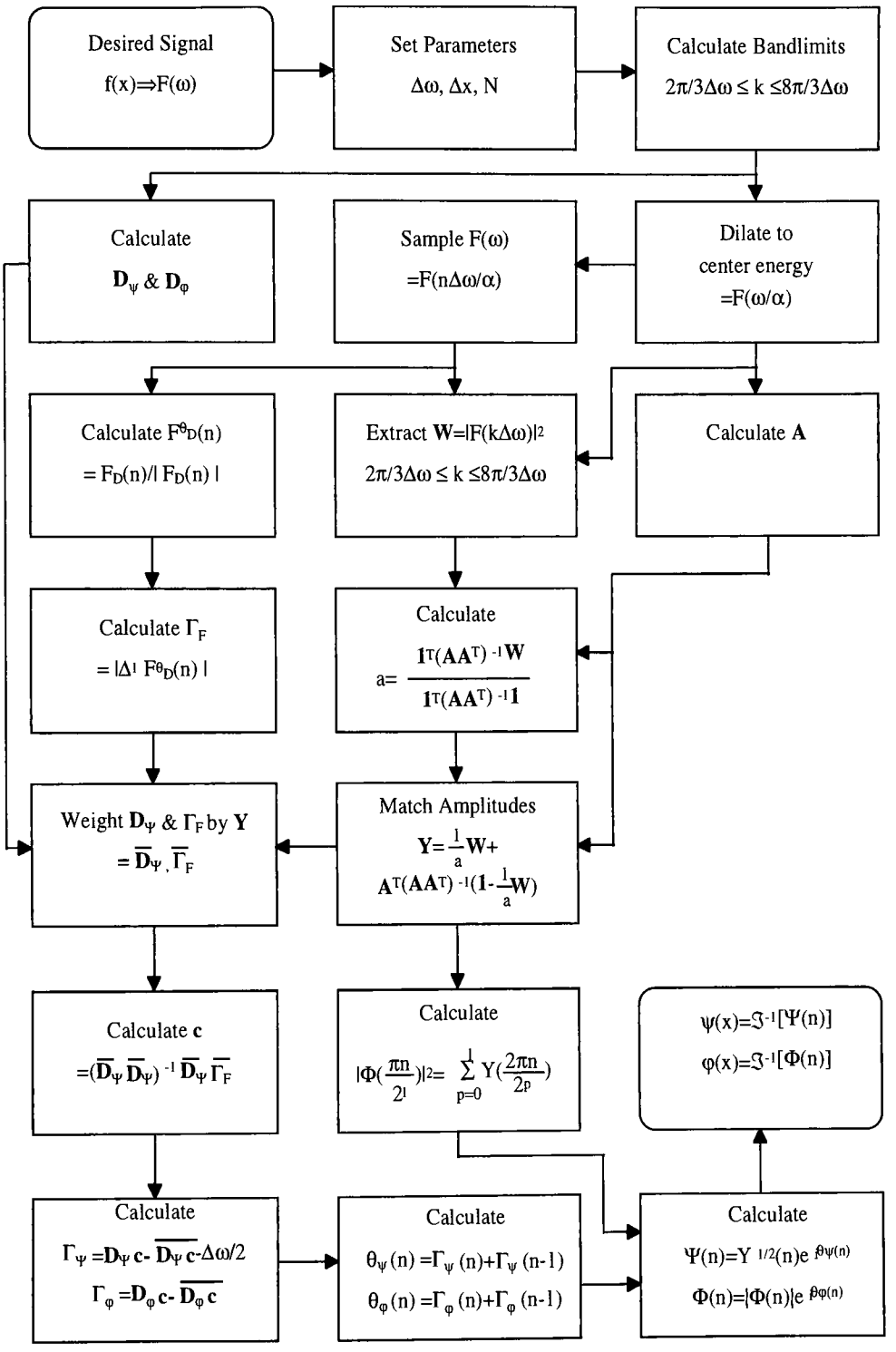

Figure 5.1: Algorithm Flow Chart

Then the power spectrum of the optimal matched wavelet is calculated using the algorithm in (5.51)–(5.54) of Theorem 9. Furthermore, the resultant wavelet, given by,

$$\Psi(k\Delta\omega) = \sqrt{Y(k)}e^{i\theta_F(k\Delta\omega)} \tag{5.89}$$

where $\theta_F(\omega)$ is the phase of $F(\omega)$, is a dyadic wavelet satisfying the stability condition,

$$0 < A \leq Z(\xi) = \sum_{j=-\infty}^{\infty} \left|\Psi\left(2^j\xi\right)\right|^2 \leq B < \infty \tag{5.90}$$

and $A = B = 1$.

Proof.

While $\Psi(\omega)$ does not satisfy the bandlimits of Theorem 7, it does satisfy (5.37) given in discrete form in (5.35), where $\Phi(\omega)$ is the Fourier Transform of some function, $\phi(x)$ (no longer a scaling function), and as specified, $\Phi(0) = 1$. Substituting $\omega = \xi/2^\ell$ in (5.37) gives

$$\begin{aligned} \left|\Phi\left(\frac{\xi}{2^\ell}\right)\right|^2 &= \sum_{j=0}^{\infty} \left|\Psi\left(2^{j+1-\ell}\xi\right)\right|^2 \\ &= \sum_{j=1-\ell}^{\infty} \left|\Psi\left(2^j\xi\right)\right|^2. \end{aligned} \tag{5.91}$$

Taking the limit of both sides as $\ell \to \infty$ gives

$$\begin{aligned} \lim_{\ell\to\infty} \left|\Phi\left(\frac{\xi}{2^\ell}\right)\right|^2 &= \sum_{j=-\infty}^{\infty} \left|\Psi\left(2^j\xi\right)\right|^2 \\ |\Phi(0)|^2 &= \\ 1 &= \end{aligned} \tag{5.92}$$

which satisfies the stability condition,

$$0 < A \leq \sum_{j=-\infty}^{\infty} \left|\Psi\left(2^j\xi\right)\right|^2 \leq B < \infty \tag{5.93}$$

where $A = B = 1$.□

It is worth noting that while the matched wavelet derived with Theorem 11 does not have an associated scaling function and is not associated with an MRA, it still must satisfy its Poisson summation. Therefore, integer translates of the matched dyadic wavelets are orthonormal. The violation of the MRA construct is due to the dyadic wavelets being non-orthonormal with wavelets on a different scale, that is,

$$\langle \psi_{j,k}, \psi_{\ell,m} \rangle = \rho_{j,\ell} \cdot \delta_{k,m} \tag{5.94}$$

where $\rho_{j,\ell} \neq \delta_{j,\ell}$.

The algorithm in this theorem is identical to that of Theorem 9 with two exceptions: 1) the bandlimits on $\Psi(\omega)$ exceed those required by Theorem 7; and 2) the phase of the resultant wavelet is simply the phase of the desired signal. When the bandlimits are constrained to those given in Theorem 7, the resultant wavelet from the amplitude matching algorithm is an orthonormal wavelet whose associated scaling function generates an orthonormal MRA. If the bandlimits exceed those of Theorem 7, then the matched wavelet satisfies the stability condition (5.90) and is therefore a dyadic wavelet. Because the resultant wavelet has no associated scaling function, it does not have to exhibit the phase structure required of wavelets in an orthonormal MRA and can therefore, be any function. In order to maximize the matched filter output, the phase of the wavelet is set to that of the desired signal.

Decomposition/reconstruction of a signal using a dyadic wavelet requires the shift paramter, b, to be continuous. In practice, b is discrete. Kaiser [19] (Theorem 6.1) proves that bandlimited wavelets, critically sampled in b generate frames of $L^2(\Re)$.

Theorem 12 (Bandlimited Wavelets and Frames) *Let $\psi(x)$ be a real valued, bandlimited wavelet and $\Psi(\xi)$ be its Fourier Transform. Then the family of wavelets,*

$$\psi_{b_0,j,n} = 2^{-\frac{j}{2}}\psi(2^{-j}x - nb_0) \tag{5.95}$$

is a frame of $L^2(\Re)$ where b_0 is the sample rate parameter that satisfies the Nyquist criteria. The wavelet transform is given by

$$\begin{aligned} W_f(2^j, n2^j b_0) &= \langle f, \psi_{b_0,j,n}\rangle \\ &= \int_{-\infty}^{\infty} f(x)2^{-\frac{j}{2}}\psi(2^{-j}x - nb_0)dx. \end{aligned} \tag{5.96}$$

The Inverse Wavelet Transform is given by

$$f(x) = b_0 \sum_j \sum_n W_f(2^j, n2^j b_0)2^{-\frac{j}{2}}\tilde{\psi}\left(2^{-j}x - nb_0\right) \tag{5.97}$$

where $\tilde{\psi}(x)$ is the dual of $\psi(x)$ and its Fourier Transform is given by

$$\tilde{\Psi}(\xi) = \frac{\Psi(\xi)}{\sum_j |\Psi\left(2^j\xi\right)|^2} \tag{5.98}$$

and

$$0 < A \leq \sum_j \left|\Psi\left(2^j\xi\right)\right|^2 \leq B < \infty. \tag{5.99}$$

Proof

Let $\psi(x)$ be a real-valued, bandlimited wavelet, then it must satisfy (3.6)–(3.9). Because $\Psi(\xi)$ has finite support in ξ, the right side of (3.9), where $a = 2^j$, can be represented by its Fourier series expansion,

$$2^{\frac{j}{2}}\overline{\Psi(2^j\xi)}F(\xi) = 2^j b_0 \sum_n c_n(j) e^{-i2\pi\xi n 2^j b_0} \tag{5.100}$$

where

$$\begin{aligned} c_n(j) &= \int_{-\infty}^{\infty} F(\xi) 2^{\frac{j}{2}} \overline{\Psi\left(2^j\xi\right)} e^{i2\pi\xi n 2^j b_0} d\xi \\ &= W_f(2^j, n2^j b_0) \end{aligned} \tag{5.101}$$

which can be shown by letting $a = 2^j$ and $b = n2^j b_0$ in (3.8). Substituting (5.101) into (5.100) gives

$$2^{\frac{j}{2}}\overline{\Psi(2^j\xi)}F(\xi) = 2^j b_0 \sum_n W_f(2^j, n2^j b_0) e^{-i2\pi\xi n 2^j b_0}. \tag{5.102}$$

Multiplying both sides by $2^{-j/2}\Psi(2^j\xi)$ and summing over j gives

$$\sum_j \left|\Psi\left(2^j\xi\right)\right|^2 F(\xi) = b_0 \sum_j \sum_n W_f(2^j, n2^j b_0) 2^{\frac{j}{2}} \Psi\left(2^j\xi\right) e^{-i2\pi\xi n 2^j b_0}. \tag{5.103}$$

Again, let $Y(\xi) = \sum_j |\Psi(2^j\xi)|^2$ where $0 < A \leq Y(\xi) \leq B \leq \infty$, then

$$\begin{aligned} F(\xi) &= b_0 \sum_j \sum_n W_f(2^j, n2^j b_0) 2^{\frac{j}{2}} Y^{-1}(\xi) \Psi\left(2^j\xi\right) e^{-i2\pi\xi n 2^j b_0} \\ &= b_0 \sum_j \sum_n W_f(2^j, n2^j b_0) 2^{\frac{j}{2}} \tilde{\Psi}\left(2^j\xi\right) e^{-i2\pi\xi n 2^j b_0}. \end{aligned} \tag{5.104}$$

Taking the inverse Fourier Transform of (5.104) gives the expression for the inverse Wavelet Transform with discrete scale and shift,

$$f(x) = b_0 \sum_j \sum_n W_f(2^j, n2^j b_0) 2^{-\frac{j}{2}} \tilde{\psi}\left(2^{-j}x - nb_0\right) \tag{5.105}$$

where

$$\tilde{\Psi}(\xi) = \frac{\Psi(\xi)}{\sum_j \left|\Psi\left(2^j\xi\right)\right|^2}. \tag{5.106}$$

□

Chapter 6

Examples

In this chapter, several examples are given that demonstrate the performance of both the orthonormal and dyadic wavelet matching algorithms.

6.1 Orthonormal Wavelets

The performance of both the magnitude and phase matching algorithms will be demonstrated with several examples. In each of the following examples, $N = 512$, and $\Delta\omega = 2\pi/16$ so that $M = 4$. In each of the figures shown, the input signal is a dotted line and the matched signal is a solid line. With $M = 4$, the non-zero frequency indices in (5.45) are $k = \{6, 7, \ldots, 21\}$. The equality constraints in (5.43) and (5.44) of Theorem 8 generate $L = 11$ equations and 16 unknowns represented by the $\mathbf{A}$ matrix in Figure 6.1. Recall that (5.43) was derived by constructing $|\Phi(k\Delta\omega)|^2$ from the sum of repeated dilations $|\Psi(k\Delta\omega)|^2$then replicating that sum every 2π and summing giving the Poisson summation for Φ, which should be 1 everywhere. This process is illustrated in Figure 6.2, taking into account the bandlimits of (5.44) and solving for $|\Phi(k\Delta\omega/2)|^2$ instead of $|\Phi(k\Delta\omega)|^2$. Dilating $|\Psi(k\Delta\omega/2)|^2$ gives back $|\Psi(k\Delta\omega)|^2$ which is the first row of Figure 6.2. Dilating again produces the second row and so on. The pattern exhibited in the first 5 rows of Figure 6.2 exist for negative frequency indices as well. Now, replicating that structure by 4π (since we have just constructed $|\Phi(k\Delta\omega/2)|^2$) is done by shifting and centering it about $k = 32$, since $\Delta\omega = \pi/8$, which produces the structure to the lower right of Figure 6.2.

$$\begin{bmatrix}
1 & 0 & 0 & 0 & 0 & 0 & 1 & 0 & 0 & 0 & 0 & 0 & 0 & 0 & 0 & 0 \\
0 & 1 & 0 & 0 & 0 & 0 & 0 & 0 & 1 & 0 & 0 & 0 & 0 & 0 & 0 & 0 \\
0 & 0 & 1 & 0 & 0 & 0 & 0 & 0 & 0 & 0 & 1 & 0 & 0 & 0 & 0 & 0 \\
0 & 0 & 0 & 1 & 0 & 0 & 0 & 0 & 0 & 0 & 0 & 0 & 1 & 0 & 0 & 0 \\
0 & 0 & 0 & 0 & 1 & 0 & 0 & 0 & 0 & 0 & 0 & 0 & 0 & 0 & 1 & 0 \\
0 & 0 & 0 & 0 & 0 & 1 & 0 & 0 & 0 & 0 & 0 & 0 & 0 & 0 & 0 & 1 \\
0 & 0 & 0 & 0 & 0 & 0 & 1 & 0 & 0 & 0 & 0 & 0 & 0 & 0 & 1 & 0 \\
0 & 0 & 0 & 0 & 0 & 0 & 0 & 1 & 0 & 0 & 0 & 0 & 0 & 1 & 0 & 0 \\
0 & 0 & 0 & 0 & 0 & 0 & 0 & 0 & 1 & 0 & 0 & 0 & 1 & 0 & 0 & 0 \\
0 & 0 & 0 & 0 & 0 & 0 & 0 & 0 & 0 & 1 & 0 & 1 & 0 & 0 & 0 & 0 \\
0 & 0 & 0 & 0 & 0 & 0 & 0 & 0 & 0 & 0 & 2 & 0 & 0 & 0 & 0 & 0
\end{bmatrix}$$

Figure 6.1: Constraint Matrix - A for $2\pi/3 \leq \omega \leq 8\pi/3$

These values were the negative frequency values of the original structure. The positive frequency values reside on the opposite side of $k = 32$. Replicating any further in either the positive or negative direction would not produce any additional overlap. Therefore, the complete, unique set of 11 independent equations (enclosed in the dotted box in Figure 6.2) can now be obtained from columns $k = 6, \ldots, 16$, by adding columnwise and remembering that the sum for any column must be 1. The coefficients of these 11 equations, 16 unknowns are represented in the condition matrix **A**.

6.1.1 Meyer's Wavelet

Meyer's wavelet is a bandlimited wavelet that forms an orthonormal basis of $L^2(\Re)$. If it is used as the desired signal, the matching algorithm should produce Meyer's wavelet exactly. Since the wavelet is real and symmetric, there is no need to match the phase. Meyer's wavelet, shown in Figure 6.3, is defined in the frequency domain as [10, 13]:

$$|\Psi_m(\omega)| = \begin{cases} 0 & |\omega| \leq \frac{2\pi}{3} \text{ or } |\omega| \geq \frac{8\pi}{3} \\ \sin\frac{\pi}{2}v\left(\frac{3|\omega|}{2\pi} - 1\right) & \frac{2\pi}{3} \leq |\omega| \leq \frac{4\pi}{3} \\ \cos\frac{\pi}{2}v\left(\frac{3|\omega|}{4\pi} - 1\right) & \frac{4\pi}{3} \leq |\omega| \leq \frac{8\pi}{3} \end{cases} \tag{6.1}$$

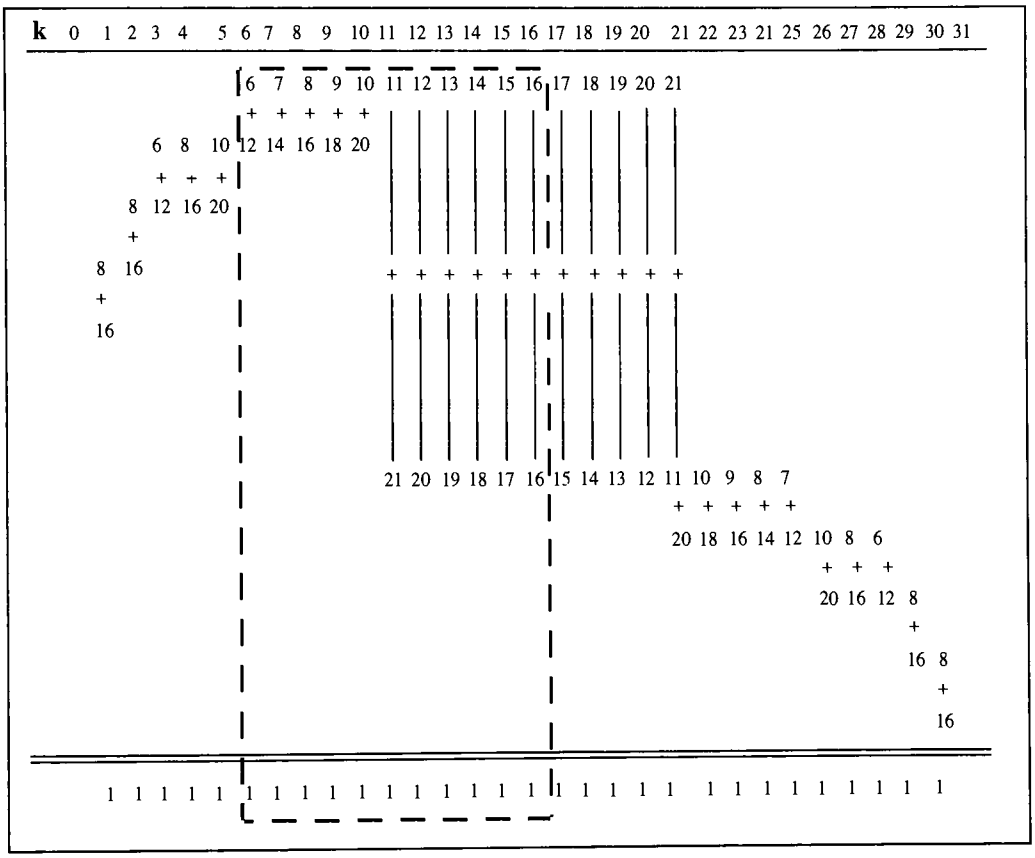

Figure 6.2: Construction of the constraint matrix A

where

$$v(\gamma) = \begin{cases} 0 & \gamma \leq 0 \\ \gamma & 0 \leq \gamma \leq 1 \\ 1 & \gamma \geq 1 \end{cases} . \tag{6.2}$$

The matched wavelet spectrum in the passband is shown in Figure 6.4. The scaling parameter, a, and

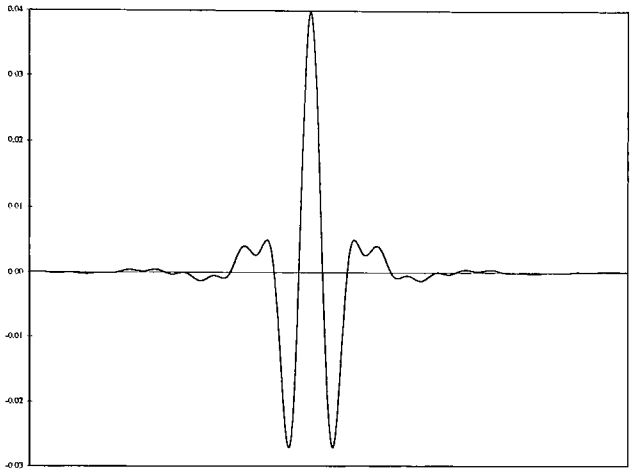

Figure 6.3: Meyer's wavelet

the match error were found to be 1 and 0, respectively, since $\mathbf{AW} = \mathbf{1}$ in (5.53). The scaling function associated with Meyer's wavelet , calculated using (5.35) is shown in Figure 6.5.

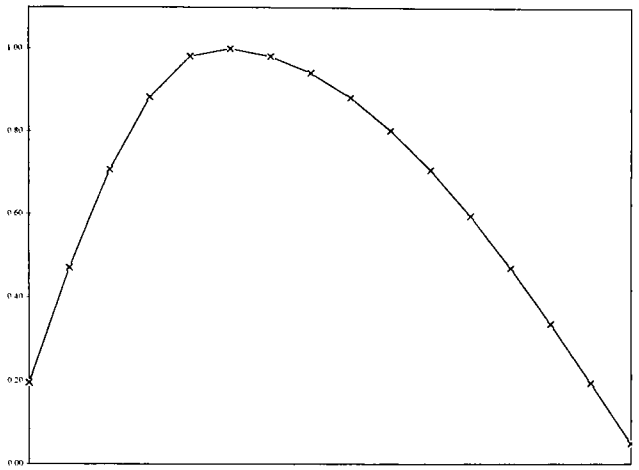

Figure 6.4: Amplitude Match in the passband - Meyer

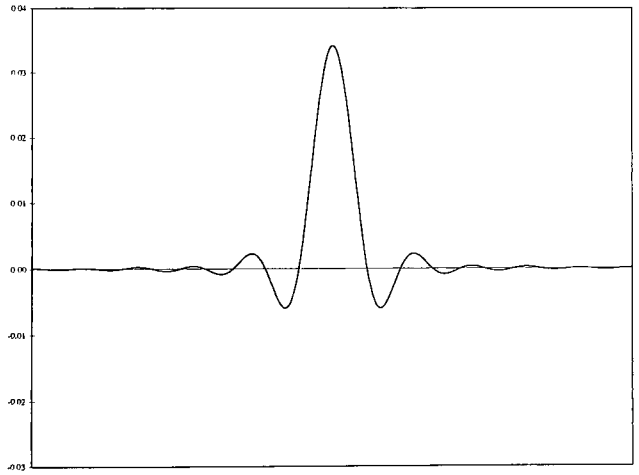

Figure 6.5: Meyer's scaling function

6.1.2 Gabor's Wavelet

Gabor's or Morlet's wavelet is also real and symmetric, but does not generate an orthonormal basis of $L^2(\Re)$. Gabor's wavelet is a modulated gaussian given by [13]:

$$f_G(x) = Ke^{\left(\frac{x}{\alpha}\right)^2} \cos(\omega_0 x) \tag{6.3}$$

and in the frequency domain as

$$\Psi(\omega) = K\alpha \left[e^{-\alpha(\omega-\omega_0)^2} + e^{-\alpha(\omega+\omega_0)^2}\right]. \tag{6.4}$$

The parameters, K, α, and ω_0 were chosen so that $\|\psi_G(x)\| = 1$ and $\Psi_G(\omega)$ was centered in the passband of the matching algorithm. Figure 6.6 shows the Gabor wavelet and Figure 6.7 shows its frequency spectrum along with its Poisson summation. The Gabor wavelet is clearly not orthonormal. Figure 6.8

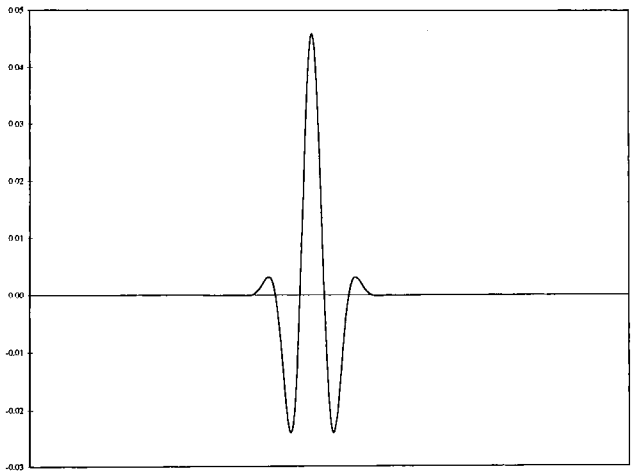

Figure 6.6: Gabor's wavelet

shows the results of the amplitude match in the passband. The scaling parameter, $a = 0.9552$ and the match error was 0.0179. The resultant wavelet and scaling function spectra with their Poisson summations are shown in Figures 6.9 and 6.10, respectively. They are both orthonormal. The matched wavelet and the desired signal are shown in Figure 6.11 and the corresponding scaling function in Figure 6.12.

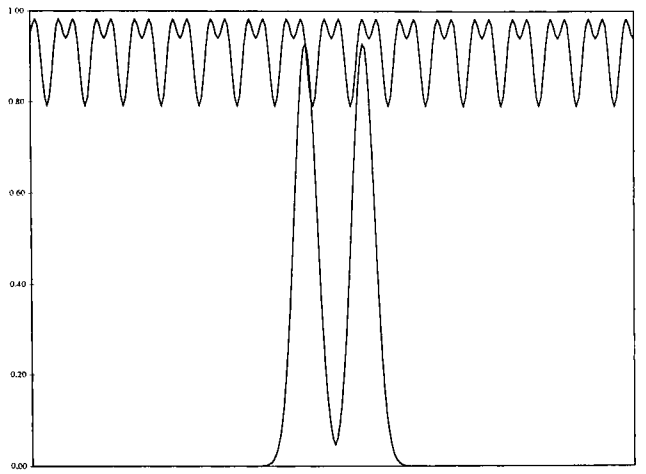

Figure 6.7: Gabor's spectrum and poisson summation

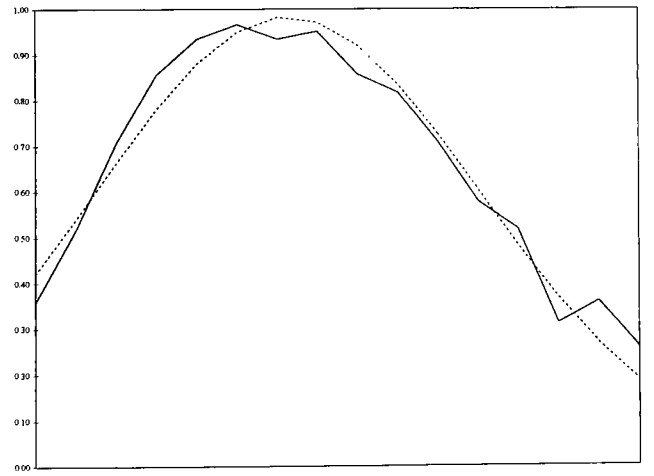

Figure 6.8: Amplitude match in the passband - Gabor's wavelet

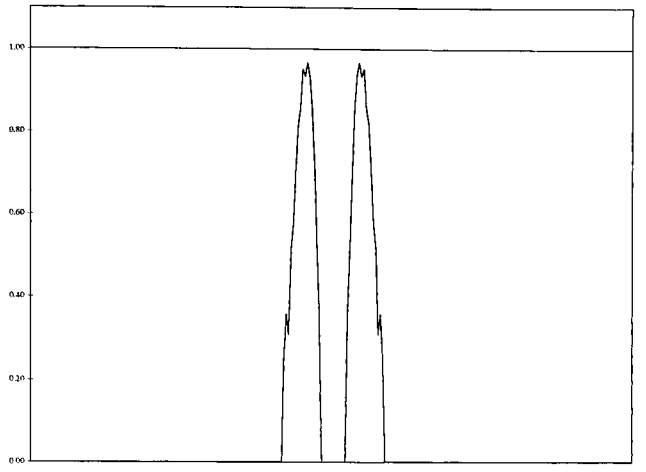

Figure 6.9: Matched wavelet spectrum and poisson summation - Gabor

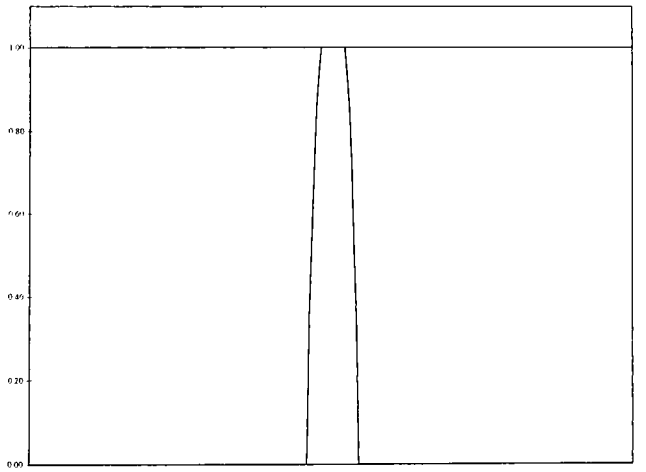

Figure 6.10: Scaling function spectrum and poisson summation - Gabor

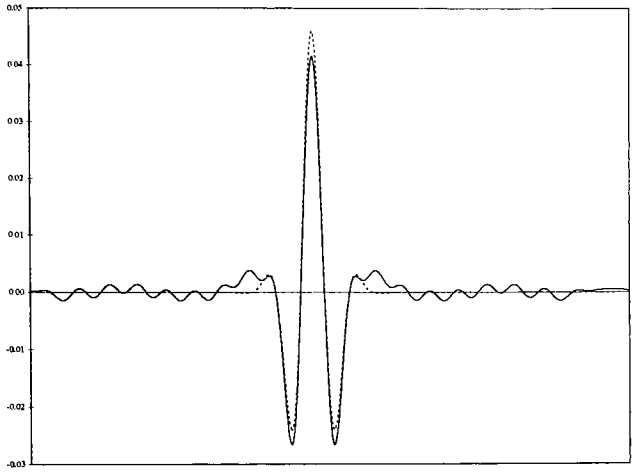

Figure 6.11: Matched wavelet vs Gabor's wavelet

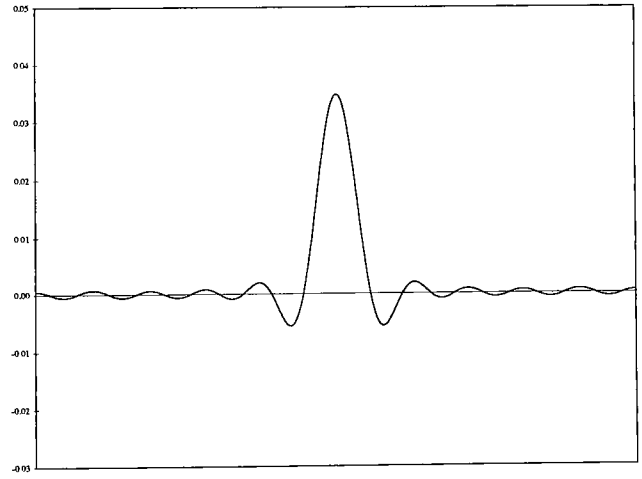

Figure 6.12: Scaling function - Gabor

6.1.3 Daubechies' D4 wavelet

Daubechies' D4 wavelet and scaling function are shown in Figure 6.13. Let the desired signal be the D4

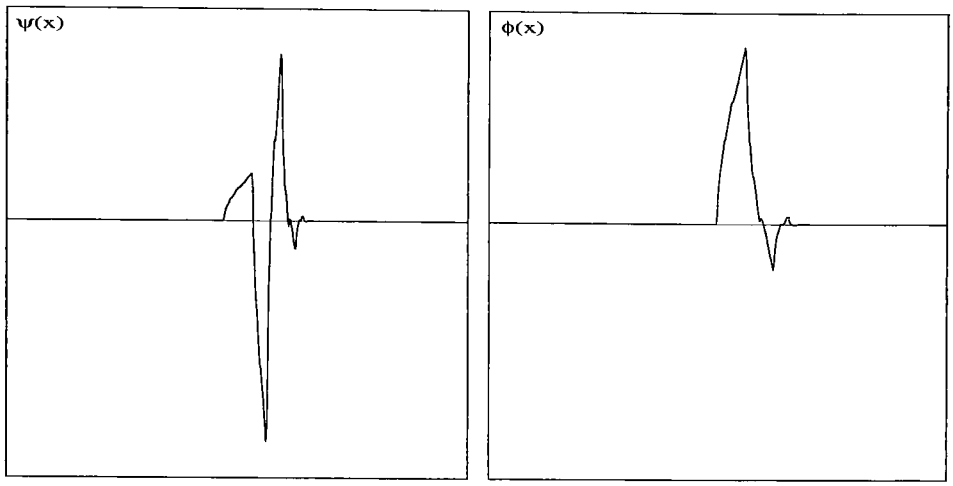

Figure 6.13: Daubechies' D4 Wavelet and Scaling Function

wavelet, given by $f_D(x)$. The desired signal power spectrum, $\{W(n)|n = -256, \ldots, 255\}$, is given as

$$W(n) = \begin{cases} |F_D(n\Delta\omega)|^2 & \text{for } |n| = \{6, 7, \ldots, 21\} \\ 0 & \text{for } |n| \neq \{6, 7, \ldots, 21\} \end{cases} \tag{6.5}$$

where $F_D(\omega)$ is the Fourier Transform of $f_D(x)$. The truncated spectrum is shown in Figure 6.14 along with its Poisson summation. Notice that the Poisson summation is no longer 1 everywhere, due to truncation. $Y(k)$ is found using (5.52) and (5.53) where $a = 0.9124$ and $\mathbf{W} = \{W(k)|k = 6, 7, \ldots, 21\}$. The results of the match in the passband are shown in Figure 6.15. The full matched wavelet spectrum is constructed by reflecting $Y(k)$ onto the negative axis, and taking its square root. The matched wavelet spectrum and its Poisson summation are shown in Figure 6.16. The wavelet is clearly orthonormal. The scaling function magnitude spectrum is calculated using (5.28) and is shown in Figure 6.17 along with its Poisson summation. The scaling function is orthonormal as well. Because we have chosen the bandlimits of Theorem 7, we are guaranteed that the resultant scaling function generates an orthonormal MRA. If we were to stop here, we would have a *symmetric* wavelet that comes closest to $f_D(x)$ and its

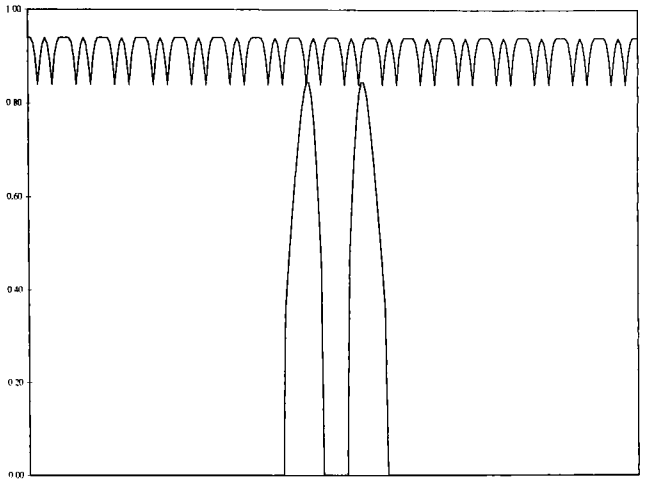

Figure 6.14: Truncated Spectrum and Poisson Summation - D4

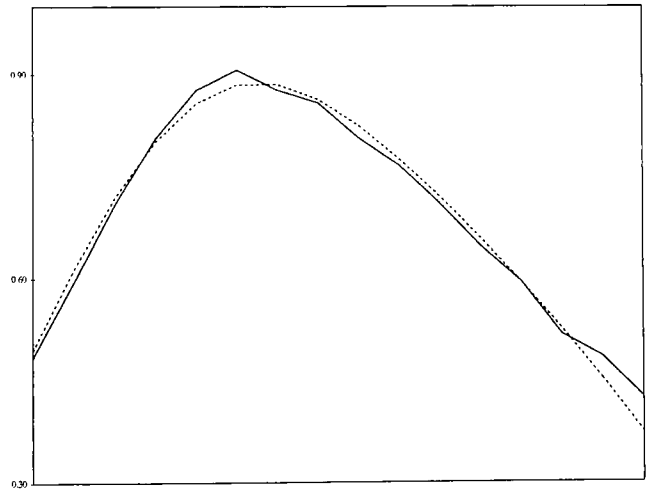

Figure 6.15: Amplitude Match in the passband - D4

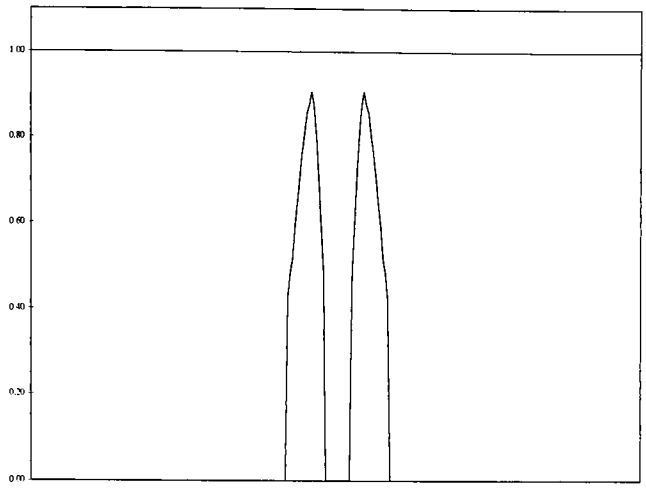

Figure 6.16: Matched Wavelet Spectrum and Poisson Sum. - D4

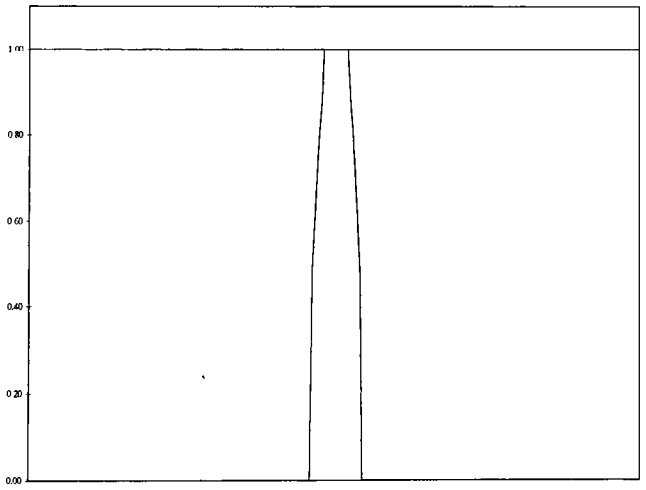

Figure 6.17: Scaling Function Spectrum and Poisson Sum. - D4

associated scaling function. The asymmetry in the D4 wavelet is caused by the structure in its phase. The first step in finding the matched phase is to find the group delay of the desired signal, $\mathbf{\Lambda}_F$, which is done using the following process:

1. Calculate $F_D^{\theta}(n\Delta\omega) = F_D(n\Delta\omega)/|F_D(n\Delta\omega)|$.
2. Interpolate across samples of $F_D^{\theta}(n\Delta\omega)$ where $|F_D(n\Delta\omega)| = 0$.
3. $\mathbf{\Lambda}_F = |\Delta^1 F_D^{\theta}(n\Delta\omega)|$ where Δ^1 is the first difference operator.

Note: This procedure eliminates the need to unwrap 2π phase jumps caused by the tan^{-1} operator. However, this procedure also generates a group delay that could have come from one of four phases, θ_F, $-\theta_F$, $\theta_F + \pi$, and $-\theta_F + \pi$. The matched wavelet is calcluated for each of these possible phases and then the one closest to the desired signal is chosen.

Next, the matrix $\mathbf{D}_{\Psi}$ from (5.78) is calculated. In these examples, $N = 512$ and $R = 16$, making $\mathbf{D}_{\Psi}$ a 512×9 matrix. The polynomial coefficient vector, $\hat{\mathbf{c}}$, is calculated using (5.82) where $\bar{\mathbf{D}}_{\Psi}$ and $\bar{\mathbf{\Gamma}}_F$ are weighted by the normalized matched spectrum, $\mathbf{Y}$, calculated above. Figure 6.18 shows $\mathbf{\Lambda}_F$ and $\mathbf{\Lambda}_{\Psi}$. They match very closely since $\mathbf{\Lambda}_F$ is the group delay of a known orthonormal wavelet

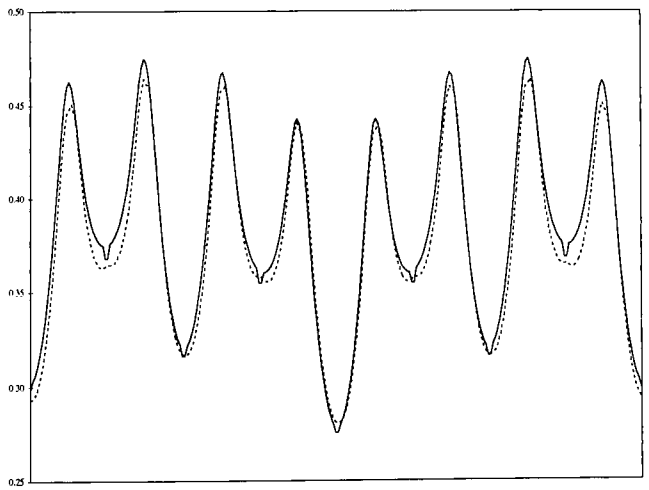

Figure 6.18: Matched Wavelet Group Delay vs desired - D4

and therefore *must* have the proper structure. The group delay of the scaling function, shown in Fig-

k	h(k)	k	h(k)	k	h(k)
-8	-0.0082	-2	-0.0055	3	-0.0407
-7	0.0256	-1	0.3515	4	0.0338
-6	-0.0085	0	0.5554	5	-0.0202
-5	-0.0173	1	0.2281	6	-0.0037
-4	0.0298	2	-0.0957	7	0.0253
-3	-0.0322				

Table 6.1: $h(k)$ for ψ matched to f_D

ure 6.19 with the group delay of the D4 scaling function, is calculated using (5.77) and (5.86). The

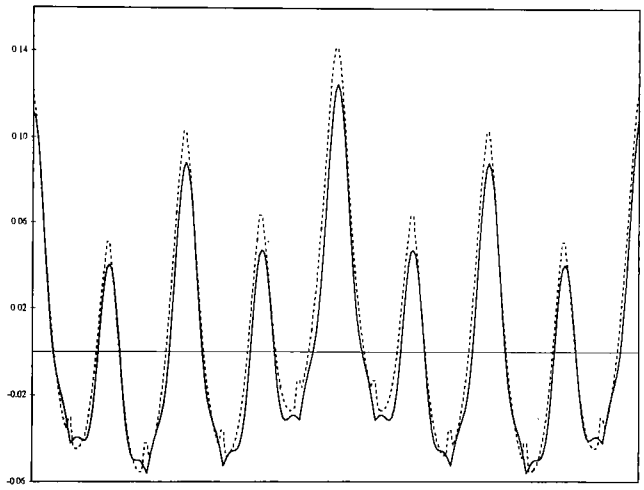

Figure 6.19: Scaling Function Group Delays: Derived vs Truth - D4

matched wavelet and scaling function phase is found by integrating (or summing) $\Lambda_\Psi(n)$ and $\Lambda_\Phi(n)$. The matched wavelet and its associated scaling function, shown in Figure 6.20, are each found by taking the inverse Fourier Transform of their complex spectra. The inner product of f_D with its matched wavelet, ψ, gives $\{\ldots\ 0.0082\ -0.0202\ 0.9963\ 0.0292\ 0.0072\ \ldots\}$. The resultant QMF filters, h and g, are shown in Figure 6.21 and the middle 16 values of h are given in Table 6.1.

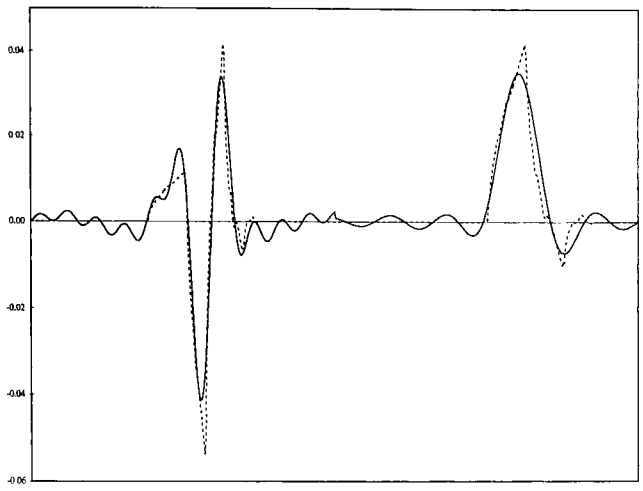

Figure 6.20: Matched Wavelet and Scaling Function vs desired - D4

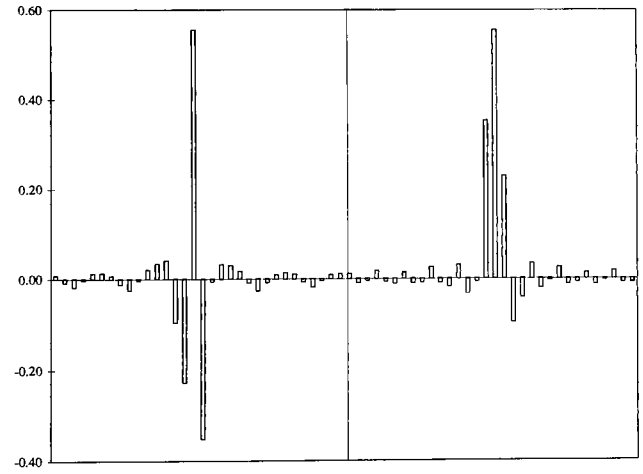

Figure 6.21: QMF filters g(k) and h(k) - D4

6.1.4 Transient signal

The next example is a transient sinusoid given by the following equation

$$f_T(x) = xe^{\alpha x}\cos(2\pi f_0 x)u(x) \tag{6.6}$$

where $u(x)$ is the unit-step function. The transient signal in this example was constructed by setting $\alpha = 2.0$ and $f_0 = 0.8$, and dilating it such that its spectrum, $F_T(\omega)$, had maximum energy in the passband, $2\pi/3 \leq |\omega| \leq 8\pi/3$. Figure 6.22 shows the transient signal and Figure 6.23, its spectrum amplitude and Poisson summation. The transient signal is clearly non-orthonormal. Following the same sequence of

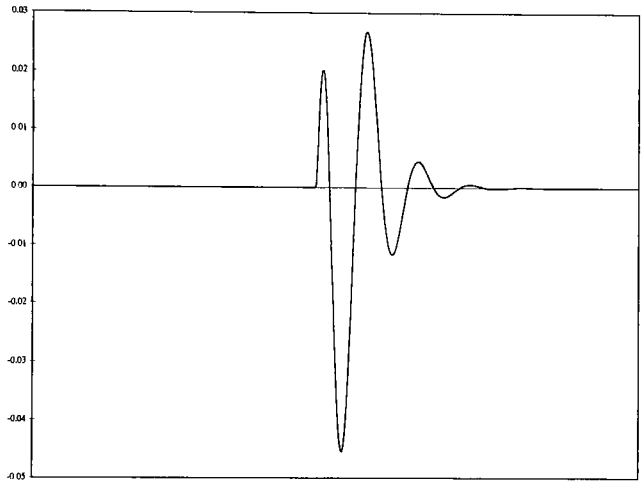

Figure 6.22: Transient Signal

steps described above for the D4 wavelet, the asymmetric wavelet that best matches $f_T(x)$ is derived. Figure 6.24 shows the result of matching the wavelet in the positive passband, where $a = 1.0348$. The full matched wavelet and scaling function spectra along with their Poisson summations are shown in Figures 6.25 and 6.26. The group delays of the desired signal, $\mathbf{\Lambda}_F$, and the matched wavelet, $\mathbf{\Lambda}_\Psi$, are shown in Figure 6.27. Since $f_T(x)$ is not a wavelet, its phase shouldn't have the required structure. However, notice that the matched wavelet group delay does have the required structure *and* matches the desired group delay very well in the passband. The matched wavelet and its associated scaling function are shown in Figures 6.28 and 6.29. The inner product of f_T with its matched wavelet, ψ gives $\{\ldots$ –

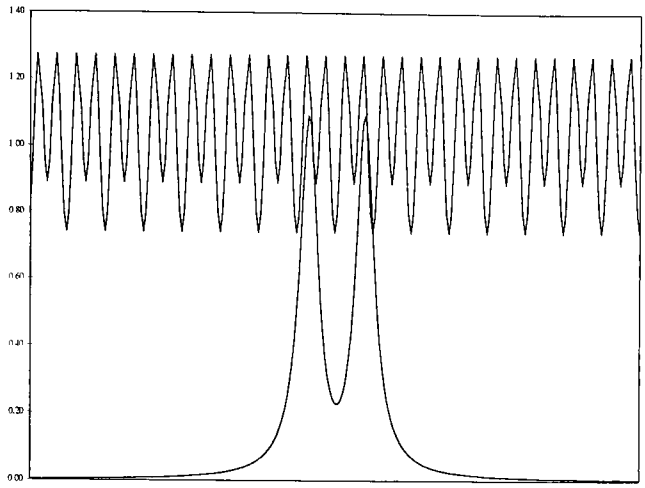

Figure 6.23: Desired Signal Spectrum and Poisson Sum - transient

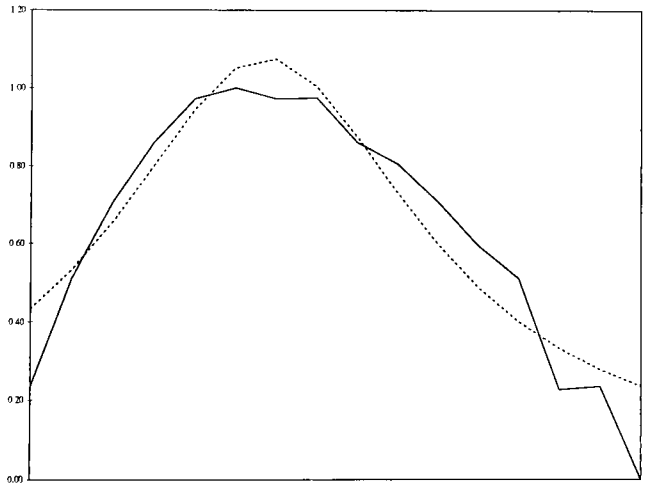

Figure 6.24: Amplitude Match in the passband - transient

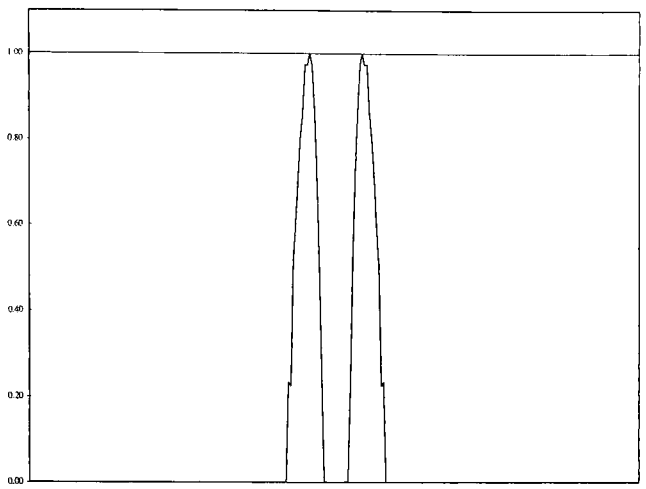

Figure 6.25: Matched Wavelet Spectrum and Poisson Sum - transient

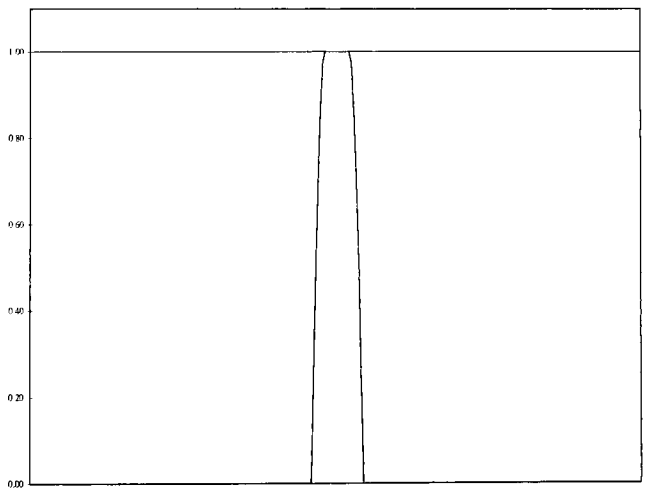

Figure 6.26: Scaling Function Spectrum and Poisson Sum - transient

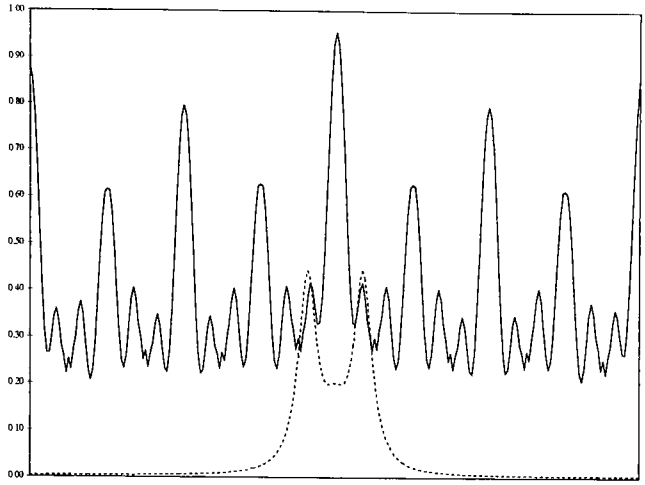

Figure 6.27: Matched Wavelet Group Delay vs desired - transient

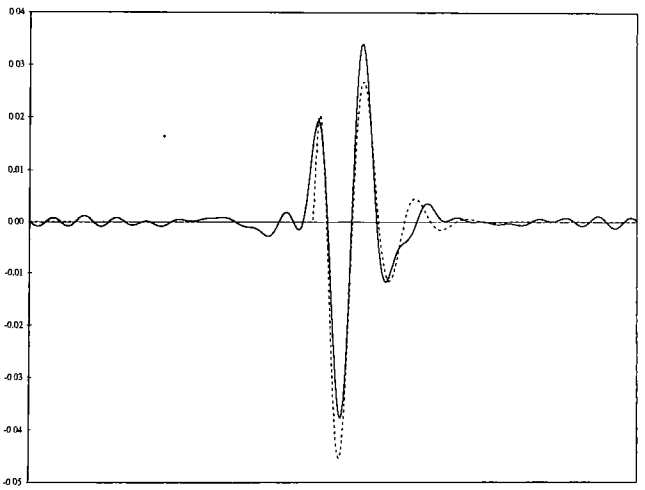

Figure 6.28: Matched Wavelet vs desired signal - transient

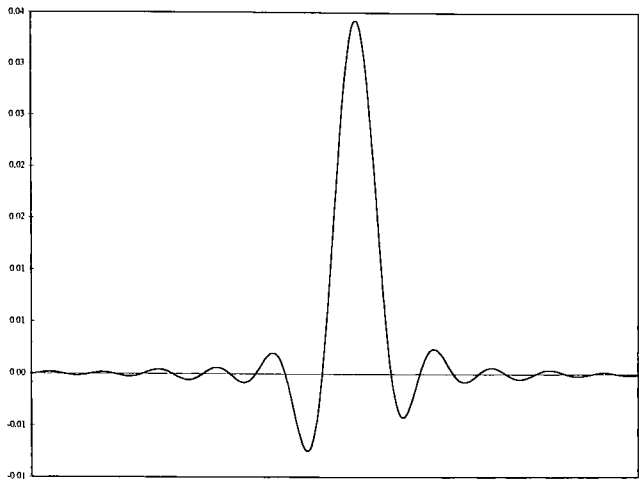

Figure 6.29: Scaling Function - transient

$0.0062 \ -0.0015 \ 0.9834 \ -0.0412 \ -0.0935 \ \ldots\}$. Eventhough f_T is not bandlimited, its correlation with the matched wavelet still produces a value very near 1.0, with very little spread in translation. The resultant QMF filters, h and g, are shown in Figure 6.30 and the middle 16 values of the QMF filter, h, are given in Table 6.2.

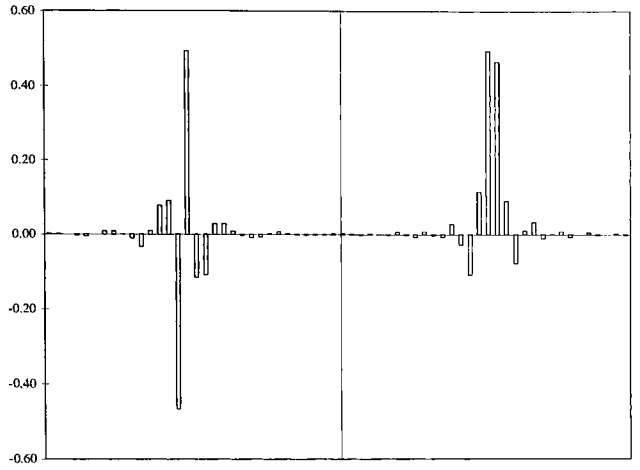

Figure 6.30: QMF filters g(k) and h(k) - transient

k	h(k)	k	h(k)	k	h(k)
-8	0.0087	-2	0.1152	3	0.0100
-7	-0.0032	-1	0.4931	4	0.0326
-6	-0.0078	0	0.4653	5	-0.0114
-5	0.0284	1	0.0901	6	-0.0006
-4	-0.0281	2	-0.0774	7	0.0078
-3	-0.1088				

Table 6.2: $h(k)$ for ψ matched to f_T

6.2 Dyadic Wavelets

This section gives some examples of optimally matched dyadic wavelets using the algorithm in Theorem 11. For each example, $N = 512$ and $\Delta\omega = 2\pi/16$ so that $M = 4$ as in the previous section. The bandlimits will be $0 < |\omega| < 4\pi$ which gives a constraint matrix, A, that is a 16×32 matrix shown in Figure 6.31. The frequency indices in (5.45) are $k = \{1, 2, \ldots, 32\}$.

$$
\begin{bmatrix}
1&1&0&1&0&0&0&1&0&0&0&0&0&0&0&1&0&0&0&0&0&0&0&0&0&0&0&0&0&1&1\\
0&1&0&1&0&0&0&1&0&0&0&0&0&0&0&1&0&0&0&0&0&0&0&0&0&0&0&0&1&0&1\\
0&0&1&0&0&1&0&0&0&0&0&1&0&0&0&0&0&0&0&0&0&0&0&1&0&0&0&0&1&0&0&0\\
0&0&0&1&0&0&0&1&0&0&0&0&0&0&0&1&0&0&0&0&0&0&0&0&0&0&0&1&0&0&0&1\\
0&0&0&0&1&0&0&0&0&1&0&0&0&0&0&0&0&0&1&0&0&0&0&0&0&1&0&0&0&0&0&0\\
0&0&0&0&0&1&0&0&0&0&0&1&0&0&0&0&0&0&0&0&0&0&1&0&1&0&0&0&0&0&0&0\\
0&0&0&0&0&0&1&0&0&0&0&0&0&1&0&0&0&0&0&0&0&0&0&1&0&0&1&0&0&0&0&0\\
0&0&0&0&0&0&0&1&0&0&0&0&0&0&1&0&0&0&0&0&0&0&0&0&1&0&0&0&0&0&0&1\\
0&0&0&0&0&0&0&0&1&0&0&0&0&0&0&0&1&0&0&0&0&1&0&0&0&0&0&0&0&0&0&0\\
0&0&0&0&0&0&0&0&0&1&0&0&0&0&0&0&0&0&1&0&1&0&0&0&0&0&0&0&0&0&0&0\\
0&0&0&0&0&0&0&0&0&0&1&0&0&0&0&0&0&0&0&1&1&0&0&0&0&0&0&0&0&0&0&0\\
0&0&0&0&0&0&0&0&0&0&0&1&0&0&0&0&0&0&0&1&0&0&0&1&0&0&0&0&0&0&0&0\\
0&0&0&0&0&0&0&0&0&0&0&0&1&0&0&0&0&0&1&0&0&0&0&0&1&0&0&0&0&0&0&0\\
0&0&0&0&0&0&0&0&0&0&0&0&0&1&0&0&0&1&0&0&0&0&0&0&0&1&0&0&0&0&0&0\\
0&0&0&0&0&0&0&0&0&0&0&0&0&0&1&0&1&0&0&0&0&0&0&0&0&0&1&0&0&0&0&0\\
0&0&0&0&0&0&0&0&0&0&0&0&0&0&0&2&0&0&0&0&0&0&0&0&0&0&0&0&0&0&0&2
\end{bmatrix}
$$

Figure 6.31: Constraint Matrix - A for $0 < \omega < 4\pi$

6.2.1 Gabor's Wavelet

Gabor's wavelet, $f_G(x)$, defined by (6.3), is dilated so that a maximum amount of its energy in the frequency domain is contained in the expanded passband represented by the constraint matrix, A (Figure 6.31). The result of the amplitude match is shown in Figure 6.32. Notice that there were samples that were driven to 0 by the inequality constraint, $Y(k) > 0$. As the passband increases, the spectrum of the desired signal becomes closer to 0, and there is a higher chance that the optimal solution would drive the sample to be negative. The inequality constraint is invoked to set that value to 0, thereby making the solution sub-optimal. Because $f_G(x)$ is real and symmetric, there is no phase to apply to $\psi(x)$. The resultant dyadic wavelet is shown in Figure 6.33 along with $f_G(x)$. The excessive ringing at the edges

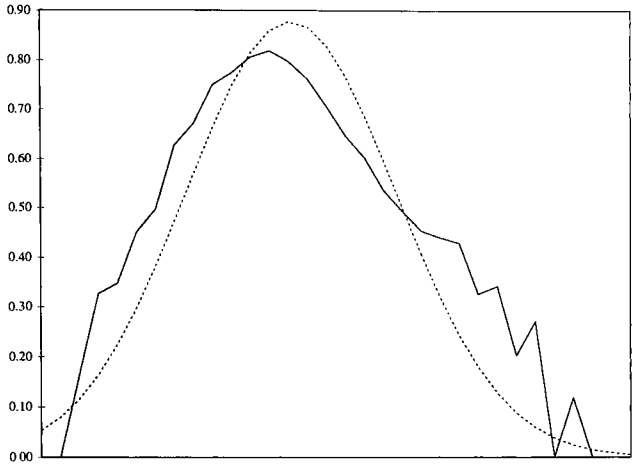

Figure 6.32: Amplitude Match in the extended passband - Gabor

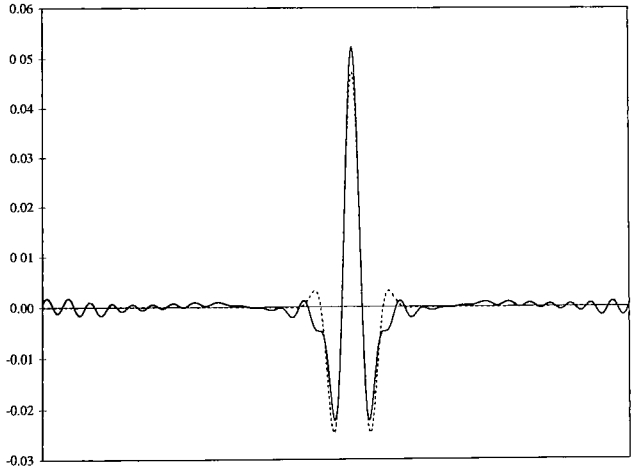

Figure 6.33: Matched Dyadic Wavelet vs Gabor's wavelet

is due to the spikes in the spectrum match caused by the inequality constraints. Figure 6.34 shows the amplitude spectrum of the matched dyadic wavelet along with its Poisson summation. The algorithm of

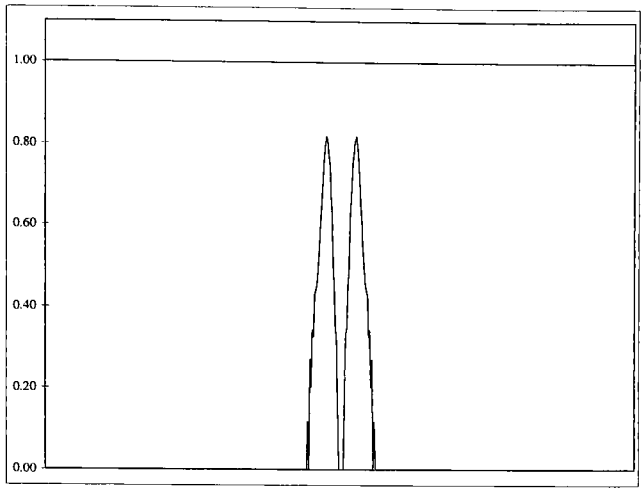

Figure 6.34: Matched Dyadic wavelet spectrum and poisson summation - Gabor

Theorem 11, like Theorem 9 guarantees the Poisson summation of the resultant wavelet to be 1. This implies that integer translates of the matched *dyadic* wavelet is orthonormal!

6.2.2 Daubechies' Wavelet

Daubechies' wavelet, shown in Figure 6.13, is the last example for the dyadic matching algorithm. The algorithm should perform better than in Section 6.1 because the extended bandlimits should produce less truncation. Figure 6.35 shows the result of the amplitude match in the passband and Figure 6.36 shows the wavelet spectrum and Poisson summation, which is 1 everywhere, as expected. Figure 6.37 shows the resultant matched dyadic wavelet along with Daubechies' D4 wavelet.

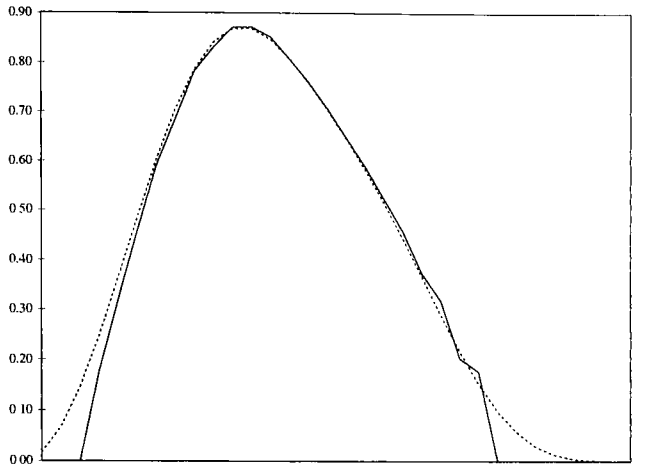

Figure 6.35: Amplitude Match in the extended passband - D4

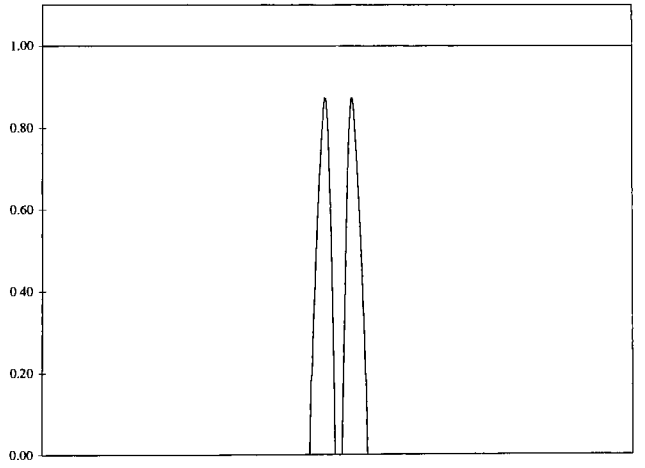

Figure 6.36: Matched Dyadic wavelet spectrum and poisson summation - D4

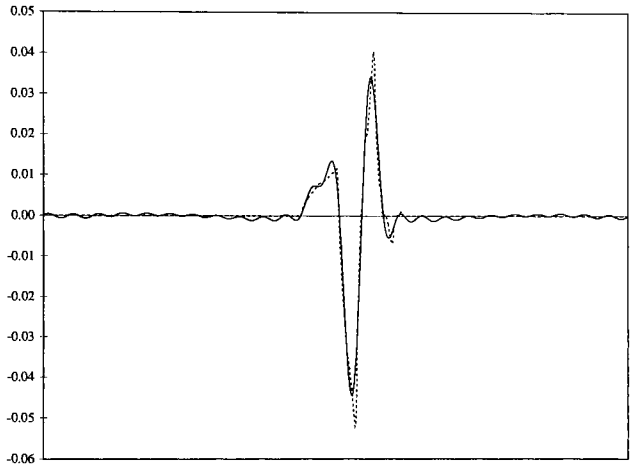

Figure 6.37: Matched Dyadic Wavelet vs D4 wavelet

Chapter 7

Applications to Image Object Detection

In this chapter, the matched wavelet algorithm is used to detect and identify an object in an image. The approach does not use the 2-D Discrete Wavelet Transform because of its shift variance and lack of rotation sensitivity (see Chapter 3.8). Instead, the 2-dimensional object is transformed into a series of 1-dimensional vectors using the sampled Radon Transform [15]. The matched wavelets for each of the 1-D vectors is calculated and used to detect the object, and determine the aspect ratio, scale, and angle of rotation. Further application of the matched wavelet algorithm on the object details provides additional feature vectors that can be used for more detailed identification.

This chapter is divided into four sections, the first two provide background on the Radon Transform and image reconstruction using backprojection and the projection slice theorem. Section 7.3 contains an introduction to the Wavelet Radon Transform and Section 7.4 develops the detection algorithm and gives results.

7.1 The Radon Transform

The Radon Transform was developed by its namesake, Johann Radon, in his 1917 paper entitled "On the determination of functions from their integrals along certain manifolds" [29]. The Radon Transform allows one to represent a 2-dimensional function, $f(x, y)$, by an infinite series of 1-dimensional projec-

tions that cover the x–y plane. The standard form of the Radon Transform is as follows:

$$q_\theta(\rho) = \mathcal{R}f = \int_L f(x,y)d\sigma \tag{7.1}$$

where q is the Radon Transform of f, $\mathcal{R}$ is the Radon Transform operator, and L is the line defined by

$$\rho = x\cos\theta + y\sin\theta \tag{7.2}$$

for $\rho \in \Re$ and $0 \leq \theta \leq \pi$. As shown in Figure 7.1 the Radon Transform is formed by rotating the coordinate axis through some continuous angle, θ, and integrating along the new vertical axis (σ–axis). The resultant transform is a function of both the new horizontal axis, ρ, and the angle of rotation, θ. Using the coordinate transformation equations for a rotated coordinate frame gives the following form

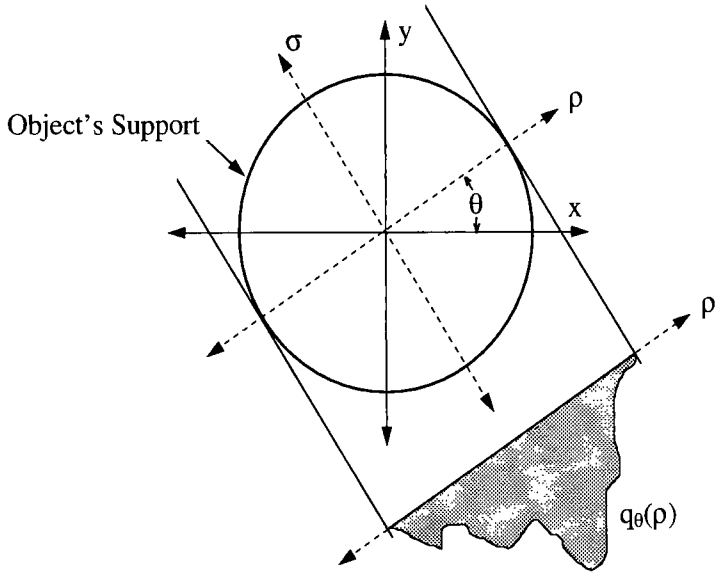

Figure 7.1: Projection geometry for tomographic processing

of the Radon Transform,

$$q_\theta(\rho) = \mathcal{R}f = \int_L f(\rho\cos\theta - \sigma\sin\theta, \rho\sin\theta + \sigma\cos\theta)d\sigma. \tag{7.3}$$

Figure 7.2 shows an image of a 2-D rectangle function and its Radon Transform. Notice that at 0°, the Radon Transform is a "rect" function whose width is equal to the width of the rectangular object. Like-

wise, at 90°, the Radon Transform is a "rect" function whose width is the same as the height of the rectangular object. The Radon Transform is taken for $0 \leq \theta < \pi$ because the projections for $\pi \leq \theta < 2\pi$

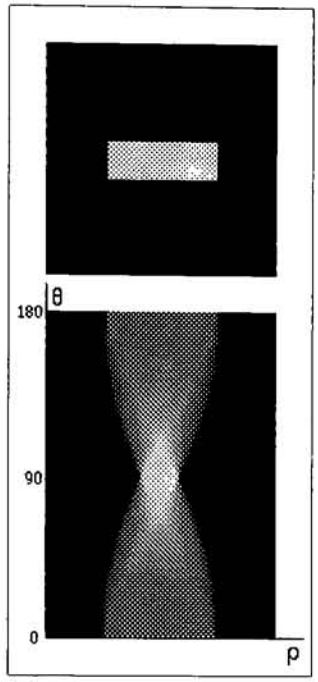

Figure 7.2: Radon Transform of a rectangle image

contain redundant information. The symmetry relationship between projections taken from an angle $0 \leq \theta < \pi$ and an angle rotated an additional π radians is given as

$$q_{\theta+\pi}(\rho) = q_{\theta}(-\rho). \tag{7.4}$$

This relationship can be seen graphically in Figure 7.1. A projection taken 180° from the angle shown will produce a projection that is simply flipped along its horizontal axis.

When θ is sampled with sample spacing $\Delta\theta$, the resultant transform is referred to as the Sampled Radon Transform [15]. The Radon Transform in Figure 7.2 is actually a Sampled Radon Transform because it was constructed with $\Delta\theta = 1°$.

7.2 Image Reconstruction and Backprojection

Although the basic formulas for inversion of the Radon Transform were worked out as early as 1917 [29], very little if any effort was devoted to implementing the inversion in a practical situation prior to the pioneer work in radio astronomy by Bracewell [4][15]. The practical problem with the inversion formulas derived by Radon is that they require $f(x, y)$ to be a continuous function and the Radon Transform to be constructed from *all* lines in the x–y plane [15].

7.2.1 Reconstruction by direct Fourier Methods

Bracewell [4] derived the relationship between the 2-D Fourier Transform of $f(x, y)$ and the 1-D Fourier Transform of $q_\theta(\rho)$ with respect to ρ. The relationship is given as

$$\begin{aligned} F_\theta(\eta, \zeta) &= F_\theta(\omega_x \cos\theta + \omega_y \sin\theta, 0) \\ &= F(\eta\cos\theta - \zeta\sin\theta, \eta\sin\theta + \zeta\cos\theta) \\ &= Q_\theta(\eta) = \int_{-\infty}^{\infty} q_\theta(\rho) e^{-i2\pi\eta\rho} d\rho \end{aligned} \tag{7.5}$$

where η and ζ are the spatial frequency variables as shown in Figure 7.3, and F_θ is F rotated through θ. The result, later referred to as the Projection Slice Theorem, states that the 1-D Fourier Transform of the Radon Transform for a fixed θ is equal to a slice through the 2-D Fourier Transform of $f(x, y)$ at an angle θ (Figure 7.3) [15]. Using the Projection Slice Theorem, one could approximate $F(\omega_x, \omega_y)$ given enough projections by forming a superposition of the Fourier Transform of each projection in the Sampled Radon Transform [5], given as

$$\hat{F}(\omega_x, \omega_y) = \mathcal{I}\left[\sum_i F_{\theta_i}(\eta)\right] \tag{7.6}$$

where $F_{\theta_i}(\eta)$ is the Fourier Transform of the projection taken at $\theta = \theta_i$ and $\mathcal{I}$ is an interpolation operator that resamples the data onto a cartesian grid. However, in practice, there is a finite number of projections and the sample spacing in the frequency domain is nonuniform, which causes spatially variant errors after interpolation. Several standard techniques have been developed to alleviate the non-uniform

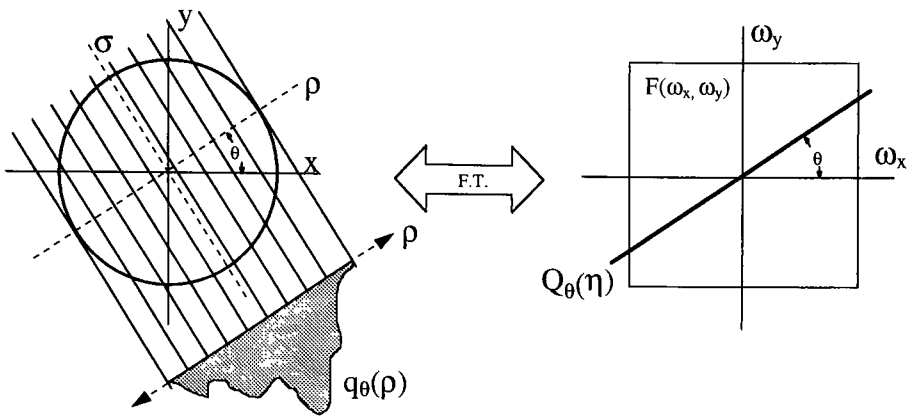

Figure 7.3: Projection Slice Theorem

sampling problem. Bracewell and others, however, developed a space domain solution, called backprojection, that works around the non-uniform sample grid in the Fourier domain.

7.2.2 Reconstruction by backprojection

Instead of constructing $\hat{F}$ as in (7.6) and then taking the inverse Fourier Transform, one could take the inverse Fourier Transform of $F_{\theta_i}(\eta, 0)$ first, and sum the results, given as

$$\hat{f}(x, y) = \int_0^{\pi} q_\theta(x \cos\theta + y \sin\theta) d\theta. \tag{7.7}$$

The inverse Fourier Transform of a slice in the frequency domain at angle, θ, is a 2-D "ridge" whose cross section through the angle θ is $\check{f}_\theta(\rho)$ and whose values are constant perpendicular to its cross section [5], as shown in Figure 7.4. The inverse Fourier Transform of a slice is referred to as a backprojection, since it is a 1-D function smeared, or replicated back along its perpendicular axis. The superposition of all backprojections forms a layergram and gives a coarse approximation of the original function, $f(x, y)$. However, the impulse response of the layergram is not a delta function. In fact, its transfer function converges to $H(\eta, \theta) = 1/\eta$ (polar notation) as $\Delta\theta \to 0$. Therefore, before taking the inverse Fourier Transform of the slice, it is necessary to multiply it by the ramp function, $r(\eta) = |\eta|$, where $-\eta_N \leq$

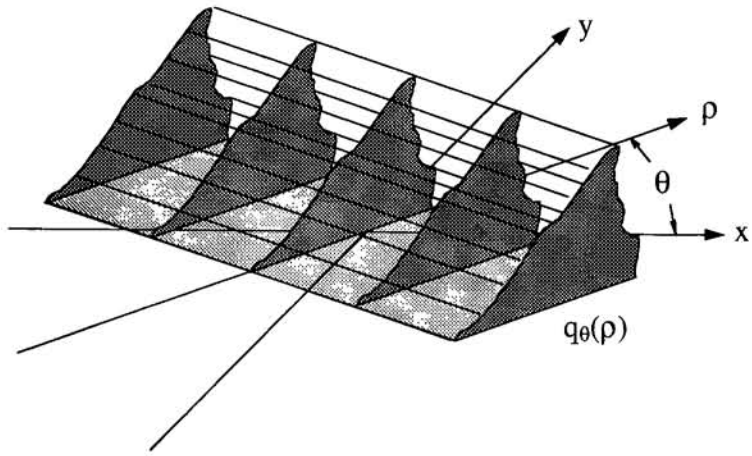

Figure 7.4: Backprojection of $q_\theta(\rho)$

$\eta \leq \eta_N$ and η_N is the Nyquist frequency. The complete modified or filtered backprojection algorithm for image reconstruction is shown in Figure 7.5. The algorithm developed over the next two sections builds off of and modifies the backprojection algorithm presented above.

7.3 The Wavelet Radon Transform

Let Figure 7.6 represent a typical collection geometry for the projection analysis described above. A 2-D image, $f(x, y)$, is represented by 8 projections, denoted as $q_i(\rho)$, taken at equal angle intervals, where the angle at which the projection is taken is $\theta_i = (i-1)\Delta\theta$, where $\Delta\theta = \pi/8$ and $i = 1, 2, \ldots, 8$. Taking the continuous wavelet transform (CWT) of each projection gives the Wavelet Radon Transform. Since in practice, the input signals are discrete signals, the CWT is approximated using matrix multiplication. Appendix G gives the specific implementation of the CWT on sampled data. Each projection can now be analyzed by way of its wavelet transform for object detection and identification. For example, assume a 512×512 image consists of a uniform background and a rectangular object of width 10 and height 30 as shown in Figure 7.7. Figure 7.8 shows its 8 projections. The projections have different frequency content (some are wider, some are narrower), which can be determined by way of its Wavelet Radon

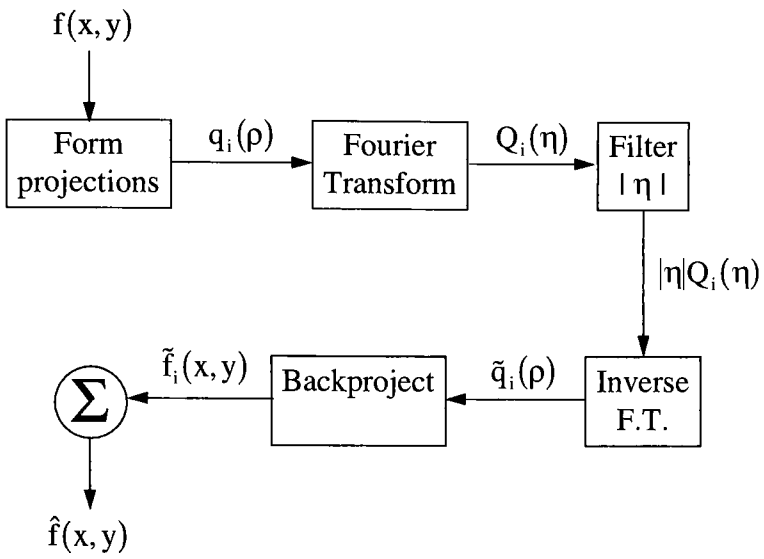

Figure 7.5: Image Reconstruction using the Backprojection Algorithm

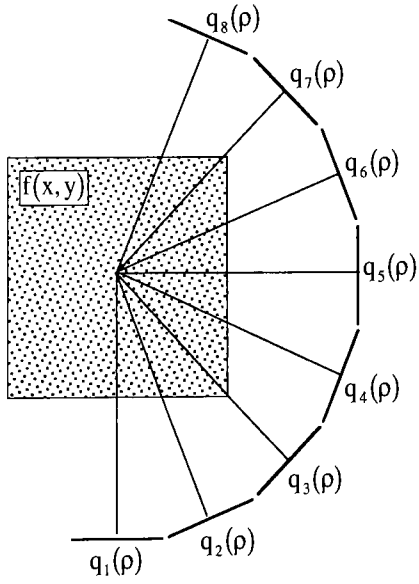

Figure 7.6: Geometry for the Wavelet Radon Transform

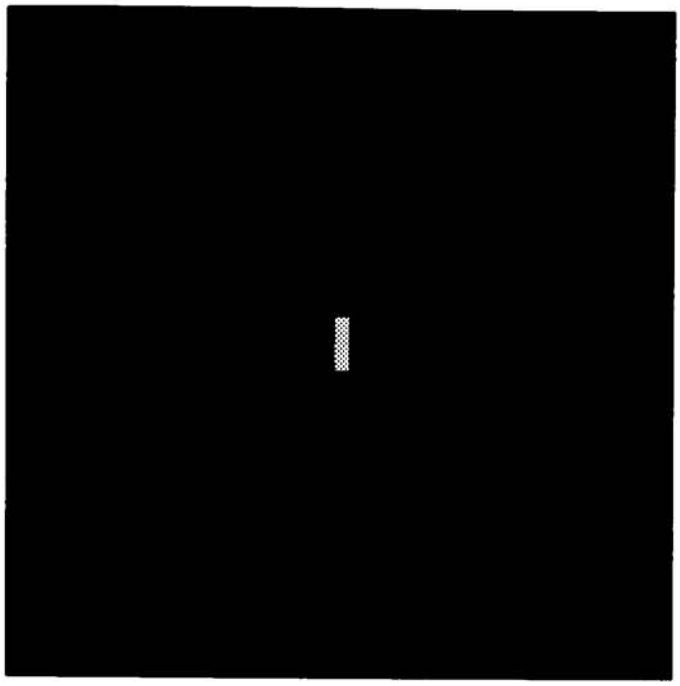

Figure 7.7: Image of a rectangular object

Transform, shown in Figure 7.9. Let the wavelet transform of $q_i(\rho)$ be denoted as $W_q^i(a,b)$, where a and b are the scale and shift parameters, respectively. In Figure 7.9, $W_q^1(a,b)$ is displayed at the top while $W_q^8(a,b)$ is at the bottom, and for each wavelet transform, scale increases downward. Notice that the peak in $W_q^1(a,b)$ occurs at very small scale and as i increases, the peak moves to larger scales until it resides at the maximum scale at $i = 5$ which corresponds to 90°. The trajectory of the peak contains information about the aspect ratio of the object and will be used in the next section as a feature vector for identifying objects in an image.

The obvious skew in the CWTs in Figure 7.9 is due to the $e^{i\omega/2}$ phase term that is required of an orthonormal wavelet (see Section 5.3.4). The phase term causes the wavelet to be centered about $x = 1/2$ and as the wavelet is dilated, the location of its center shifts, which causes the skew in the wavelet tranform.

Notice also in Figure 7.9 that at very small scales, the wavelet evokes a response from the edges of the rectangle functions in the projections. This is especially noticeable in projections 3-7. The response

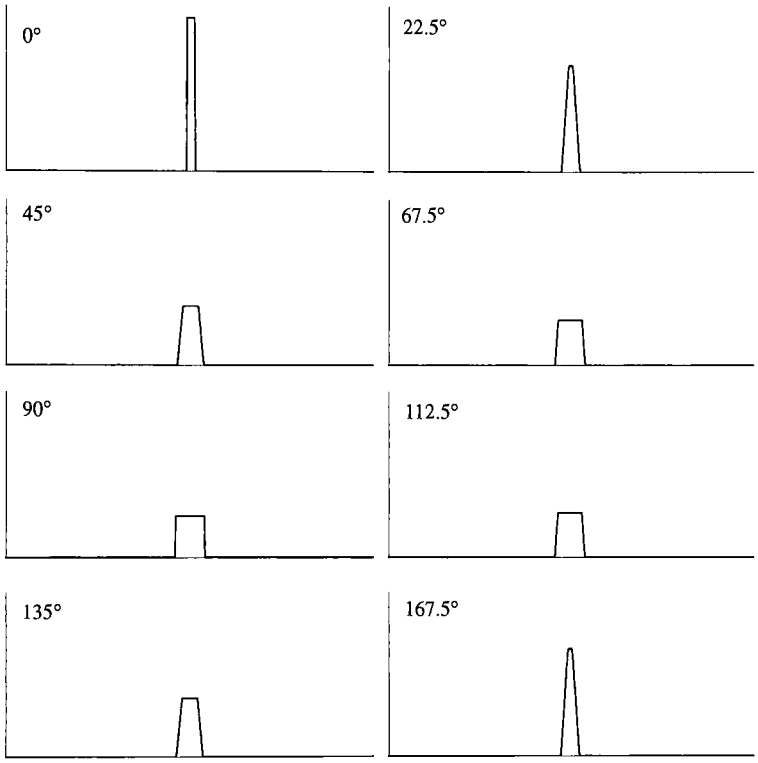

Figure 7.8: Projections of rectangle image at 8 equally spaced angular intervals

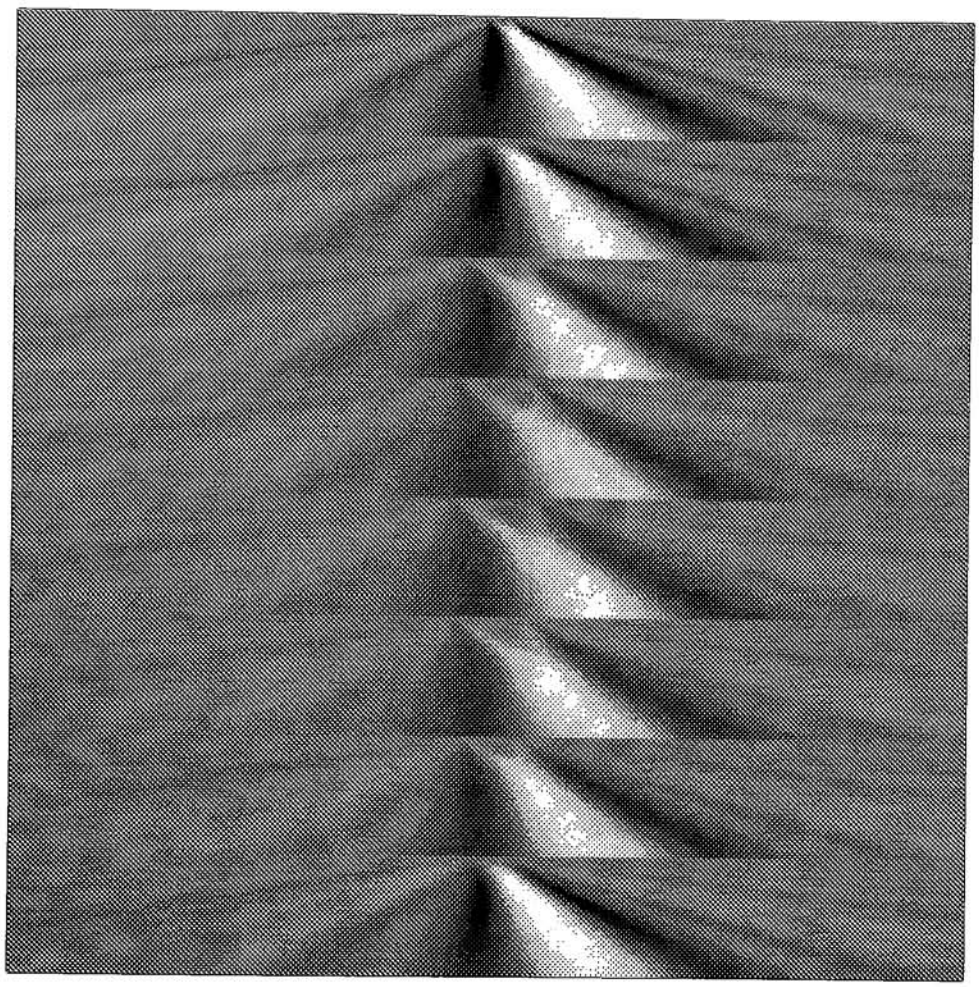

Figure 7.9: Wavelet Radon Transform of rectangle image using the D4 wavelet

from each edge (which is high frequency content or small scale) moves toward the center as the scale increases until the two intersect at the peak of the wavelet transform. At this scale, the wavelet is matched to the scale of the entire object, not just the edges. Because the peak of the wavelet transform is important in analyzing the object, it is necessary that the peak be maximized, which can be done with the matched wavelet algorithm of Chapter 5.

7.4 Matched Wavelets and Object Detection

The Wavelet Radon Transform is a useful tool for analyzing objects in an image where rotation, scale, and position are unknown. As shown in Section 5.1, the wavelet transform is much like a matched filter and therefore, the response in the Wavelet Radon Transform is maximized when the wavelets match the projections under analysis. For that reason, the wavelet matching algorithm of Chapter 5 will be used to find the optimal wavelets for each projection of the image object.

Because the optimal wavelets are bandlimited, they can match only one segment of a signal's frequency spectrum at any given time. The matching algorithm uses the maximum energy criterion for choosing which segment to match. This limitation is resolved by making multiple passes over the projections. After each pass, a residual detail signal is created by taking the difference between the original projection and the detected signals. A second pass is executed with the residual detail signals as input.

7.4.1 Training on a Known Object

Given an input image containing a known object, it is necessary to train the detection algorithm on that given object. Figure 7.10 shows the training procedure. This training procedure provides a set of matched wavelets for two passes and a maximum scale vector that provides aspect ratio, location, and rotation information. Once these functions and parameter values are obtained, they can be used as truth data to detect and identify an unknown object. The following paragraphs provide the step by step procedure for training the algorithm on a specific object.

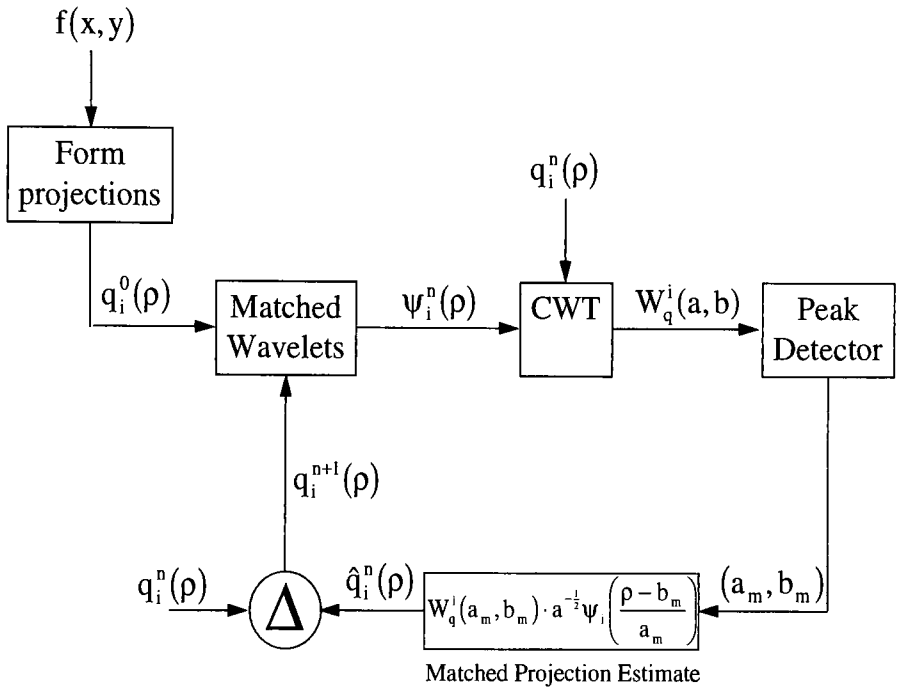

Figure 7.10: Training Procedure for Object Detection

Training step 1

The first step creates 8 1-D signals, $q_i^0(\rho)$ for $i = \{1, 2, \ldots, 8\}$, using the Sampled Radon Transform where $\Delta\theta = \pi/8$. The superscript on $q_i^0(\rho)$ indicates that these projections are the original projections that are input to the first pass of the detection algorithm. The training image is shown in Figure 7.11. It

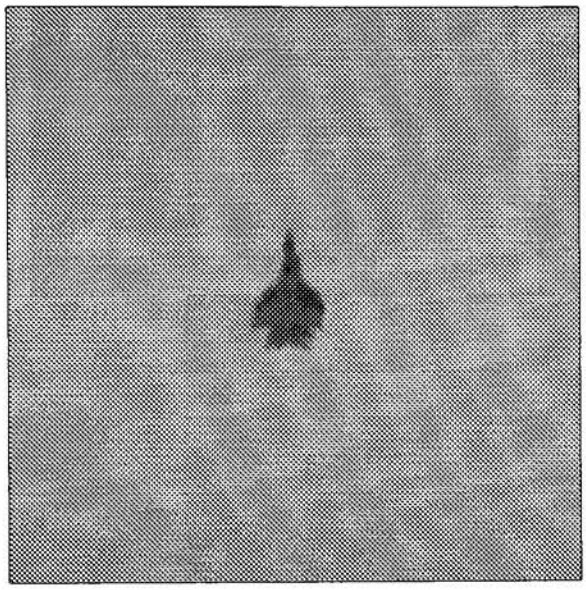

Figure 7.11: Training image of fighter aircraft

consists of a fighter aircraft against a uniform background. Its 8 projections are shown in Figure 7.12.

Training step 2

Each projection is input to the matched wavelet algorithm of Chapter 5 which creates a set of 8 matched wavelets, $\psi_i^0(\rho)$, where the superscript refers to pass 0. The first step of the matching algorithm dilates the signal such that there is a maximum amount of energy in the wavelet passband. Because the first pass will primarily find the low pass energy, the wavelet matching algorithm is set such that the passband is narrow, $2\pi/3 \leq |\omega| \leq 8\pi/3$, which are the bandlimits for orthonormal wavelets. Because the matched wavelets from pass 0 will be used to determine the rotation of the object, it is necessary that they be symmetric in order to handle the symmetry relationship given in (7.4). For this reason, the phase matching algorithm will not be used in order to guarantee symmetric matched wavelets. The resultant matched

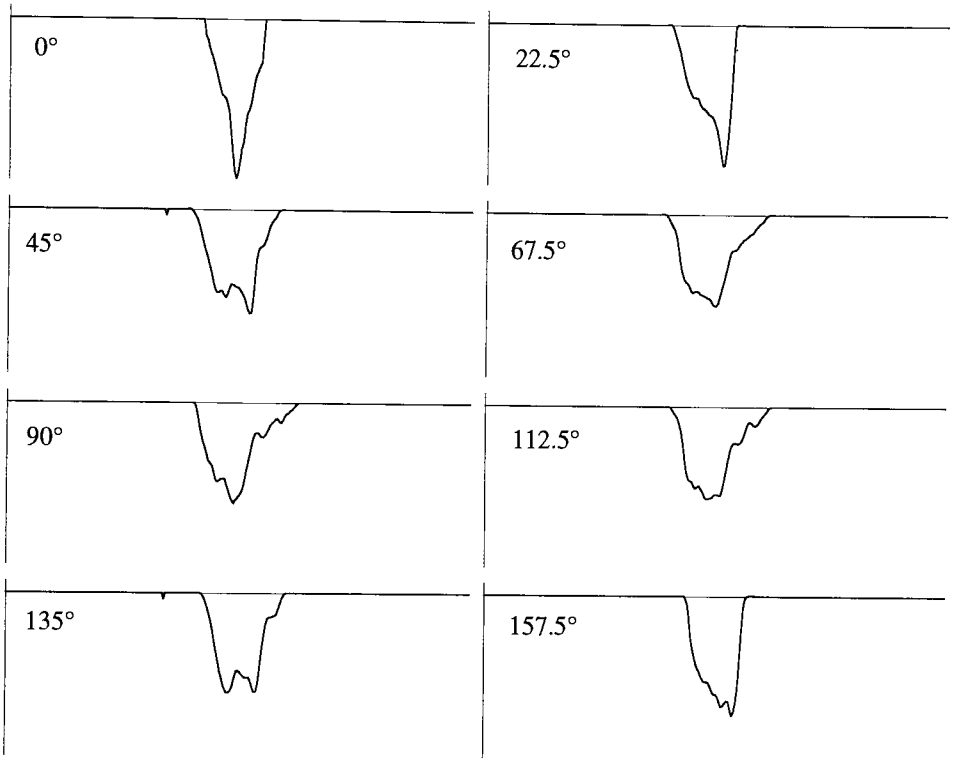

Figure 7.12: Projections of fighter aircraft taken at 8 equally spaced angles

wavelets are shown in Figure 7.13 along with the dilated projections. Notice that although each matched

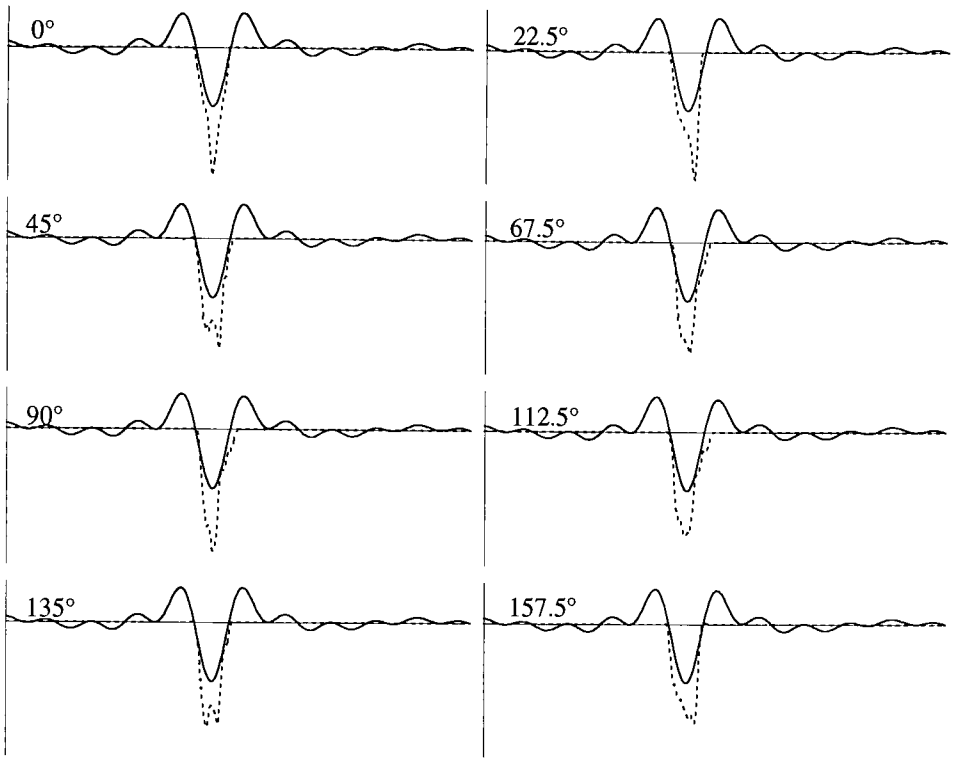

Figure 7.13: Dilated projections and their associated matched wavelets - pass 0

wavelet has zero mean, the matching algorithm found wavelets that behave like low pass filters, since only the main lobe of the wavelet overlays the projection. Furthermore, the matched wavelets for each projection are identical, since each is trying to detect the low frequency content. Therefore, the main lobe of each matched wavelet provides information about the position of each projection and hence, the object. A mask function, $m_i(\rho)$, for each projection is created by truncating the matched wavelet outside its main lobe and setting all non-zero values to 1. This mask function will be used later to filter out spurious data not coincident with the object.

Training step 3

The next step is to take the Wavelet Radon Transform, shown in Figure 7.14, using the matched wavelets as the transform operators. As in Figure 7.9, the CWT of the projection at 0° is at the top and the scale

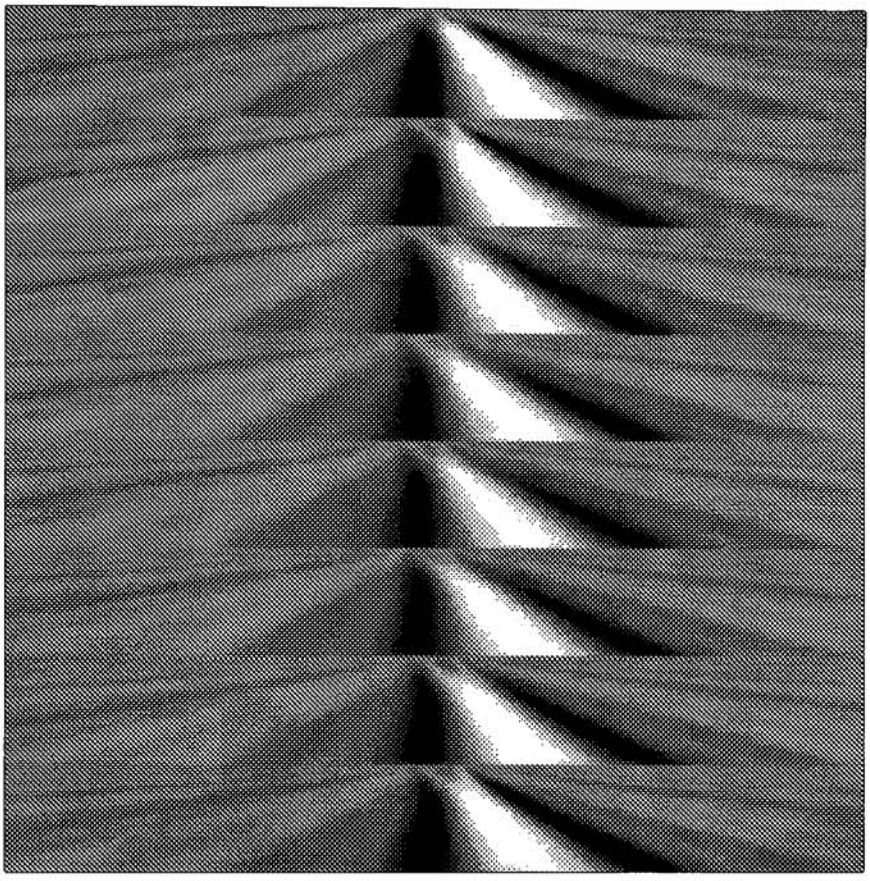

Figure 7.14: Wavelet Radon Transform of jet aircraft projections - pass 0

parameter, a, increases downward for each CWT. The horizontal axis is the shift parameter, b.

Training step 4

Information regarding the aspect ratio of the object can be extracted from the maximum scale vector, which consists of the scales at which the peak occurs in each CWT in the Wavelet Radon Transform, that is,

$$\mathbf{a}_{max} = \{a^i_{max} | W^i_q(a^i_{max}, b) \geq W^i_q(a, b), i \in \{1, 2, \ldots, 8\}, \quad \forall (a, b) \in \Re\} \tag{7.8}$$

where $W_q^i(a,b)$ is the Wavelet Transform of projection $q_i(\rho)$. Because of the nature of the Wavelet Radon Transform, $\mathbf{a}_{max}$ is scale and shift invariant and rotation invariant to 8 levels. The maximum scale vector, $\mathbf{a}_{max}$, for the fighter aircraft is

$$\mathbf{a}_{max} = \begin{bmatrix} 28 \\ 32 \\ 39 \\ 42 \\ 43 \\ 41 \\ 37 \\ 31 \end{bmatrix}. \tag{7.9}$$

Notice that the scale moves from low to high and back to low again. That is because the aircraft is longer than it is wide. Projection 0 (0°) represents the width of the aircraft and projection 5 (90°) represents the length. Because the width is smaller than the length, the match in the CWT represented by the peak will occur at lower a.

At this point, the benefits of using matched wavelets over standard, pre-designed wavelets can be demonstrated. The peak values from the Wavelet Radon Transform (WRT) found in Training step 3 were compared to those obtained from the WRT of the same projections, but using Meyer's wavelet. Figure 7.15 shows that the matched wavelets consistently produce higher peaks in the CWTs of each projection.

Training step 5

Now that the first level of training is complete, a set of residual detail signals can be constructed from the results of pass 0. The wavelet operator associated with the peak of the CWT in pass 0 is used as truth for the information detected in the first pass. Assume the peak in $W_q^i(a,b)$ occurs at (a_m, b_m). Then the estimate of the projection information matched in pass 0 is given as

$$\hat{q}_i^0(\rho) = W_q^i(a_m, b_m)\, a_m^{-\frac{1}{2}} \psi_i^0\left(\frac{\rho - b_m}{a_m}\right) m_i(\rho) \tag{7.10}$$

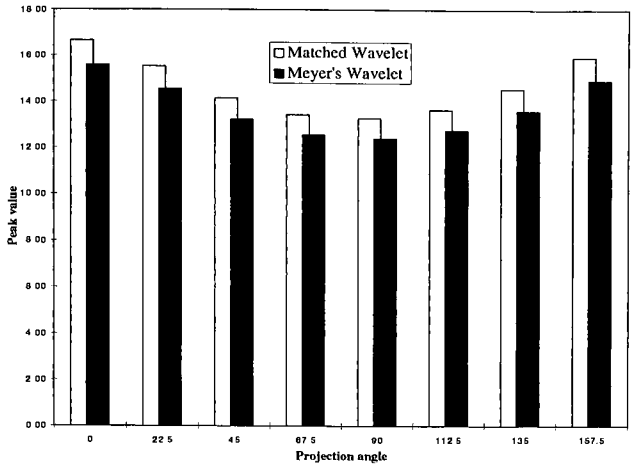

Figure 7.15: Peak values from the WRT - matched wavelets vs Meyer's wavelet

where $m_i(\rho)$ is the mask function calculated in Step 2 above. The residual detail signals are given as

$$q_i^1(\rho) = q_i^0(\rho) - \hat{q}_i^0(\rho). \tag{7.11}$$

Figure 7.16 shows each projection, $q_i(\rho)$, and its estimate, $\hat{q}_i^1(\rho)$.

Training step 6

The new set of residual projection details, $q_i^2(\rho)$ are input to the wavelet matching algorithm from which a second set of matched wavelets is derived, $\psi_i^1(\rho)$. In this pass, however, the bandlimits in the matching algorithm are set to $0 < |\omega| < 4\pi$ and the phase of the wavelet is set to the phase of its corresponding projection. The matching algorithm will therefore, generate asymmetric, dyadic wavelets, which is appropriate since the residual projection detail signals should now contain predominantly high frequency content. Figure 7.17 shows the matched wavelets (solid line) and their corresponding projections, dilated for maximum energy (dashed line).

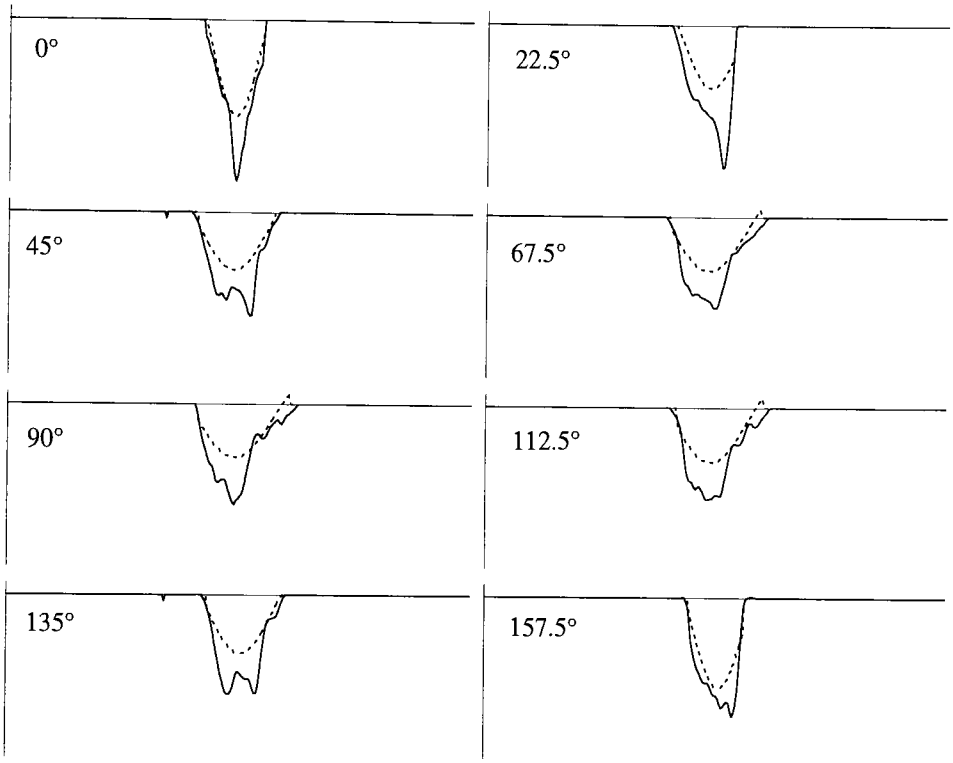

Figure 7.16: Projections and their estimate - pass 0

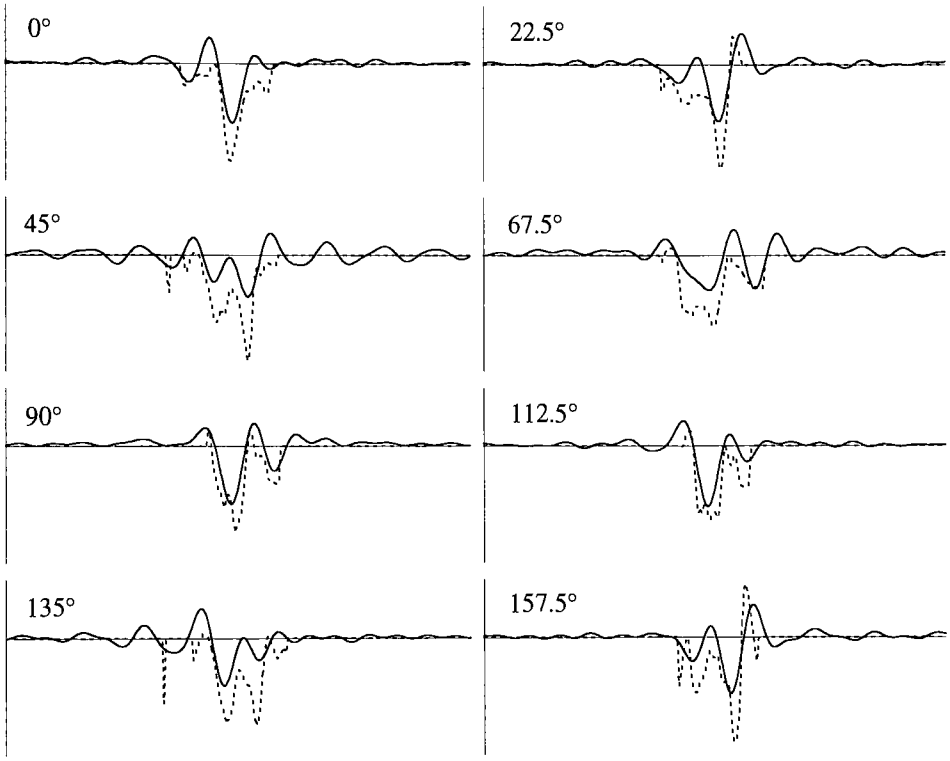

Figure 7.17: Dilated projections and their associated matched wavelets - pass 1

Training step 7-8

Steps 3 and 5 are repeated to obtain $\hat{q}_i^2(\rho)$ and $q_i^3(\rho)$, which are the projection estimate of pass 2 (Figure 7.18) and the new projections for pass 3 (if needed). Figure 7.18 shows the projection detail signals from pass 1 (solid line) and the estimates of the signal matched (dashed line). The data generated in this

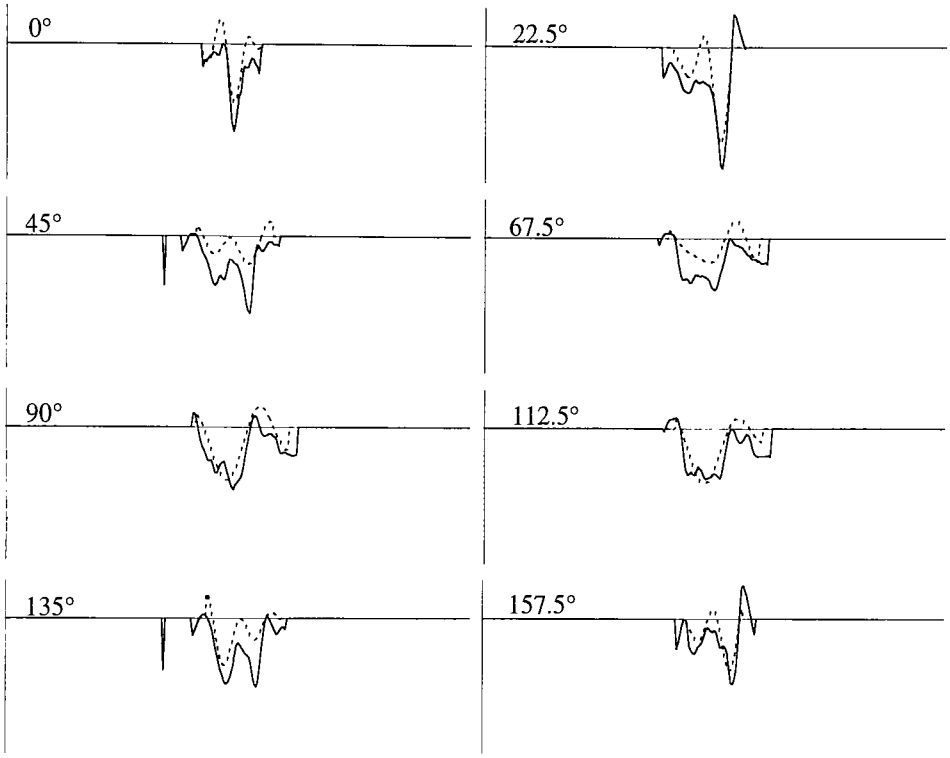

Figure 7.18: Projections and their estimate - pass 1

section can now be applied to an unknown object in order to determine if that object is the fighter aircraft used for training.

7.4.2 Object Detection

The algorithm for detecting and identifying an object developed in this section is a modification of the backprojection image reconstruction algorithm described in Section 7.2.2, and the Wavelet Radon Transform developed in Section 7.3. Figure 7.19 shows the algorithm developed in this section. Notice its sim-

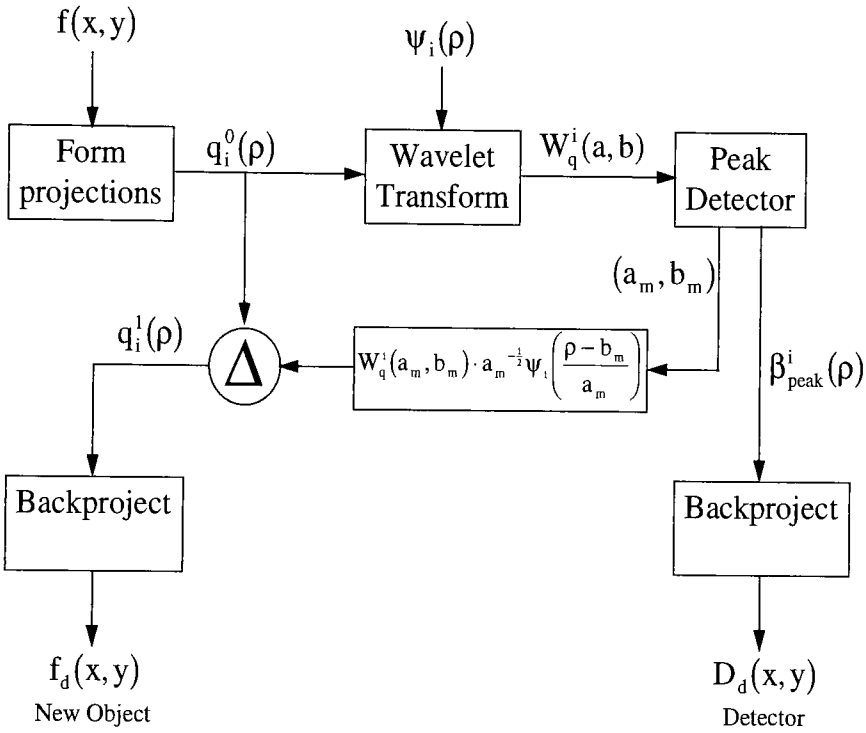

Figure 7.19: Object Detection Algorithm

ilarity to the backprojection image reconstruction algorithm shown in Figure 7.5. The key difference is that the $|\eta|$ filter is replaced by matched wavelet detection. The following paragraphs will explain each of the steps in the object detection algorithm using as an example image, the same image (Figure 7.11) used for training.

Detection step 1

The first step constructs 8 projections from the object image. Since the test image is the same as that used in training, the projections will obviously be the same (Figure 7.12).

Detection step 2

Step 2 calculates the CWT, $W_q^i(a,b)$, of the projections using the matched wavelets for pass 0 found during training. Again, since the example image in this case is identical to the training image, the CWT will be that of Figure 7.14.

Detection step 3

The peak scale vector, defined in (7.9), is derived from the CWT and will be used to determine whether the object is the same as the training object, and if so, its rotation and scale. Let $\tilde{\mathbf{a}}$ be the peak scale vector corresponding to the CWT found in this step. If the test object is a rotated and scaled version of the training object, then $\tilde{\mathbf{a}}$ will be a rotated and scaled version of $\mathbf{a}$. So, in order to determine rotation, $\tilde{\mathbf{a}}$ is circularly correlated with $\mathbf{a}$ found in Training Step 4, and then normalized by the maximum of the result, that is,

$$\mathbf{s} = \frac{\tilde{\mathbf{a}} \star \mathbf{a}}{sup\,[\tilde{\mathbf{a}} \star \mathbf{a}]} \tag{7.12}$$

where $\mathbf{s} = \{s(i) | 0 < s(i) \leq 1, \quad i = \{1, 2, \ldots, 8\}\}$ The angle of rotation will correspond to the location of the 1 (maximum value) in the circular correlation. For the example test object, $\tilde{\mathbf{a}} = \mathbf{a} = \{28, 32, 39, 42, 43, 41, 37, 31\}$. The normalized circular correlation, shown in Figure 7.20, indicates that the proposed angle of rotation is 0°, as it should be. The angle is considered a proposed angle because it has not yet been determined that the object in question is in fact the training object.

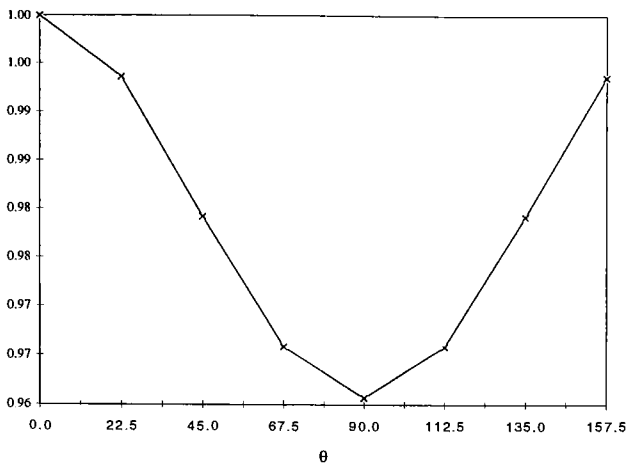

Figure 7.20: Normalized Circular Correlation, s - 0°

Once the proposed angle of rotation is determined, $\tilde{\mathbf{a}}$ can be circularly reordered to align with $\mathbf{a}$. In other words, if the proposed rotation were 22.5°, then $\tilde{a}_2$ would correspond to a_1, $\tilde{a}_3$ to a_2 and so on, finishing with $\tilde{a}_1$ corresponding to a_8, due to the symmetry of the Radon Transform. The reordered $\tilde{\mathbf{a}}$, call it $\bar{\mathbf{a}}$, can be used to find the proposed scale of the test object and a decision criteria for detection. If the test object is a scaled and rotated version of the training object, $\bar{\mathbf{a}}$, having been corrected for rotation, will be a scaled version of $\mathbf{a}$ and the scale factor across i will be a constant in the ideal case. Let γ be defined as

$$\gamma = \{\gamma_i | \gamma_i = \bar{a}_i / a_i, \quad i = \{1, 2, \ldots, 8\}\} \tag{7.13}$$

and let

$$\mu = \frac{1}{8} \sum_{i=1}^{8} \gamma_i \tag{7.14}$$

and

$$\sigma = \left\{ \frac{1}{8} \sum_{i=1}^{8} (\gamma_i - \mu)^2 \right\}^{\frac{1}{2}} \tag{7.15}$$

be the mean and standard deviation of γ. If σ is below some threshold, then the test object is detected, that is, it is the same as the training object, and μ is the scale factor of the test object to the training object.

Detection step 4

Once the test object is determined to be the training object, the remainder of the algorithm can provide additional information. Assume the peak of $W_q^i(a,b)$ occurs at (a_m^i, b_m^i). The estimate of the projection information, $\hat{q}_i^0(\rho)$, calculated using (7.10), where $m_i(\rho)$ is the mask function described in Training step 5, is the detected information. The residual details signals, $q_i^1(\rho)$, given by (7.11) represent the details remaining in the image after pass 0. Each of these sets of projections are backprojected creating a detected image, $f_d(x,y)$, and a residual detail image, $f^1(x,y)$. Figure 7.21a shows the detected image $f_d(x,y)$ overlayed on the test image. Notice that the detected image reflects the position, aspect ratio, rotation, and scale of the target. Figure 7.21b shows the resultant detail image after the first pass. Both backprojected images were thresholded at 70% of their maximum to eliminate the noise inherent to backprojection.

Detection step 5

Before repeating steps 3-4 for $q_i^1(\rho)$, the matched wavelets, $\psi_i^1(\rho)$, calculated in Training step 6 have to be adjusted for rotation. First, they have to be reordered in the same way that $\tilde{\mathbf{a}}$ was reordered so that they will align with the test projections. Second, some of the matched wavelets must be flipped along their horizontal axis. The training projections were collected at $0 \leq \theta < \pi$. If the test object is rotated an angle, φ, relative to the training image, then it is as though the test projections were collected at $\varphi \leq \theta < \pi + \varphi$. Because $q_{\theta+\pi}(\rho) = q_\theta(-\rho)$, the test projections collected for $\theta > \pi$ are ρ–reversed. Therefore, their corresponding matched wavelet must be ρ–reversed so that they will match their corresponding projections in the CWT. This procedure was not necessary in the first pass because the matched wavelets were symmetric.

Once the matched wavelets for the second pass are adjusted, Detection steps 3-4 are repeated with $q_i^1(\rho)$ as input. The backprojection results are shown in Figure 7.21c and d. The results in Figure 7.21 represent a template for a human observer to use to further identify a test object.

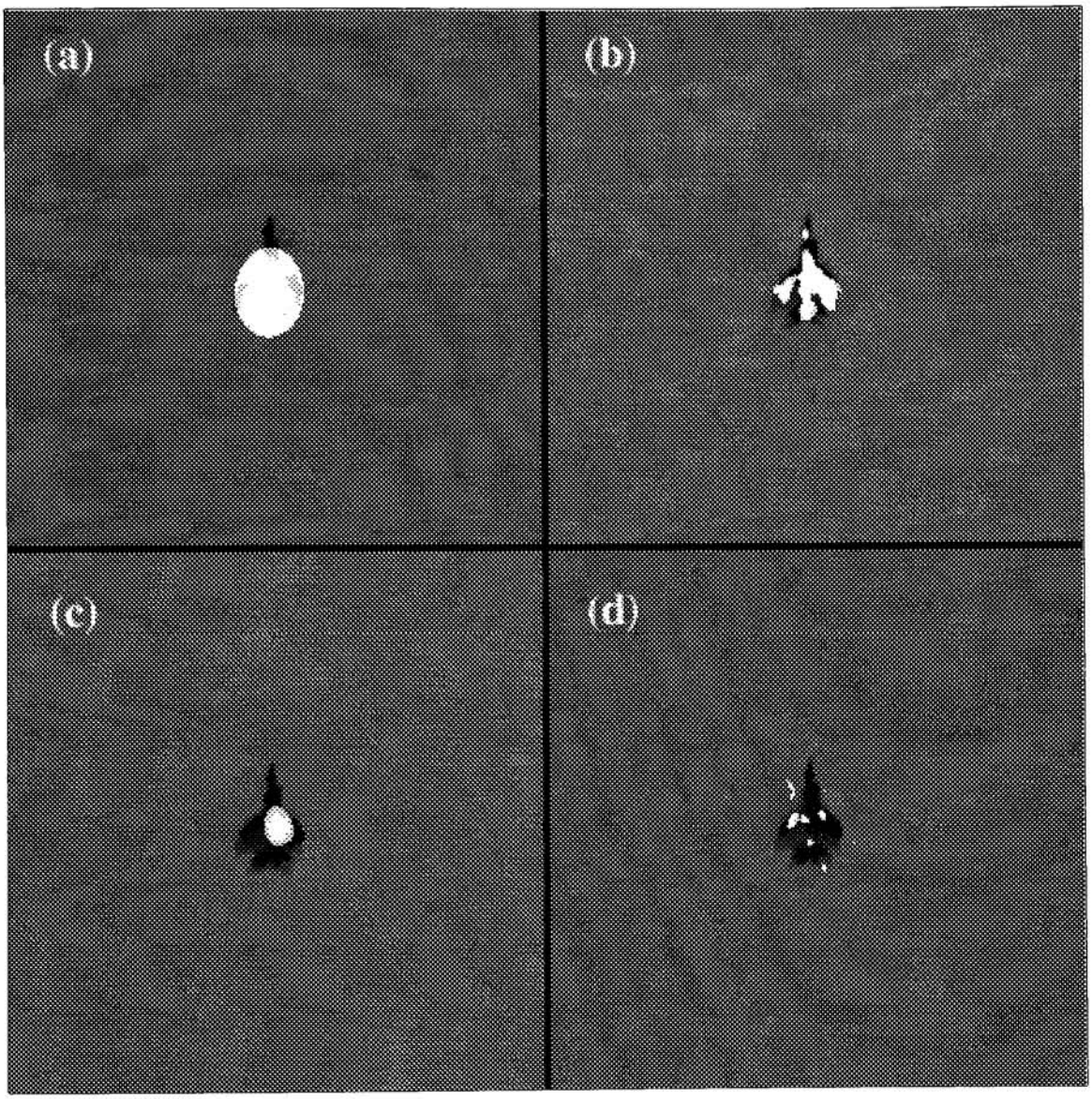

Figure 7.21: Results of backprojected detection and detail signals - 0°

7.4.3 Detection Results for an Unknown Object

To test all the functions developed in the previous section, a test image, shown in Figure 7.22, was constructed by rotating, scaling, shifting and adding noise to the fighter aircraft shown in Figure 7.11. The

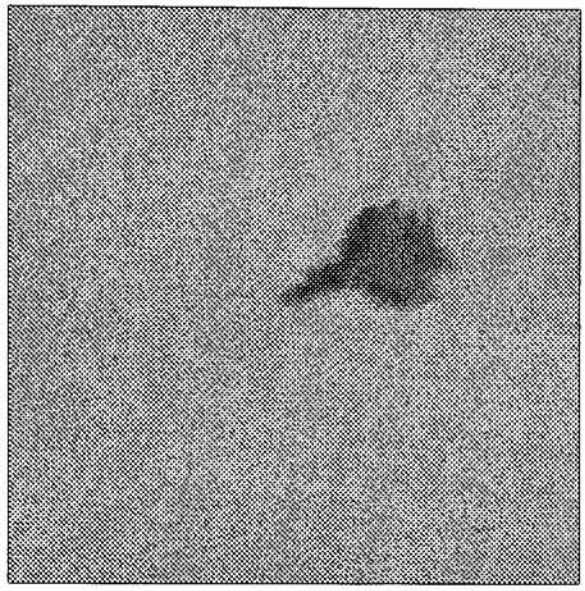

Figure 7.22: Test image for detection

angle of rotation is 112.5°, and the scale factor is 1.5. The aircraft was translated 15 pixels up and 30 pixels to the right of center and 23dB of uniform white noise was added making the calculated SNR= 2.1dB. Figure 7.23 shows the test projections and their detected estimate found from Detection steps 2–4. The Wavelet Radon Transform from pass 0 is shown in Figure 7.24. The same characteristic sinusoidal path seen in the Radon Transform of a shifted point is evident in the WRT of the translated object.

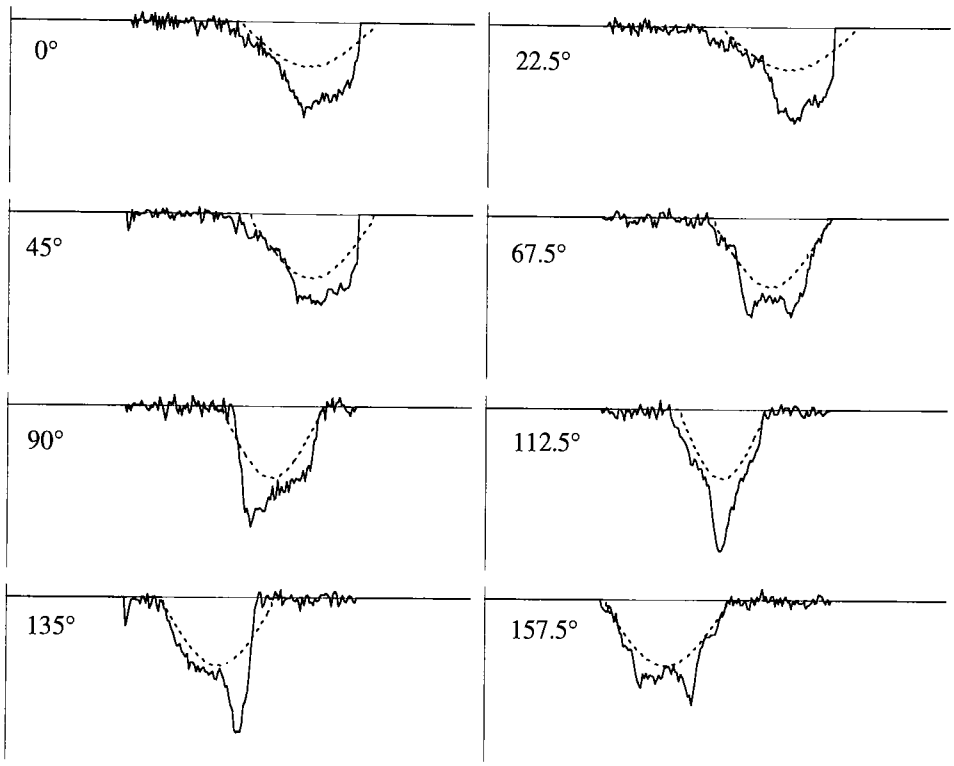

Figure 7.23: Projections and their estimate - test image, pass 0

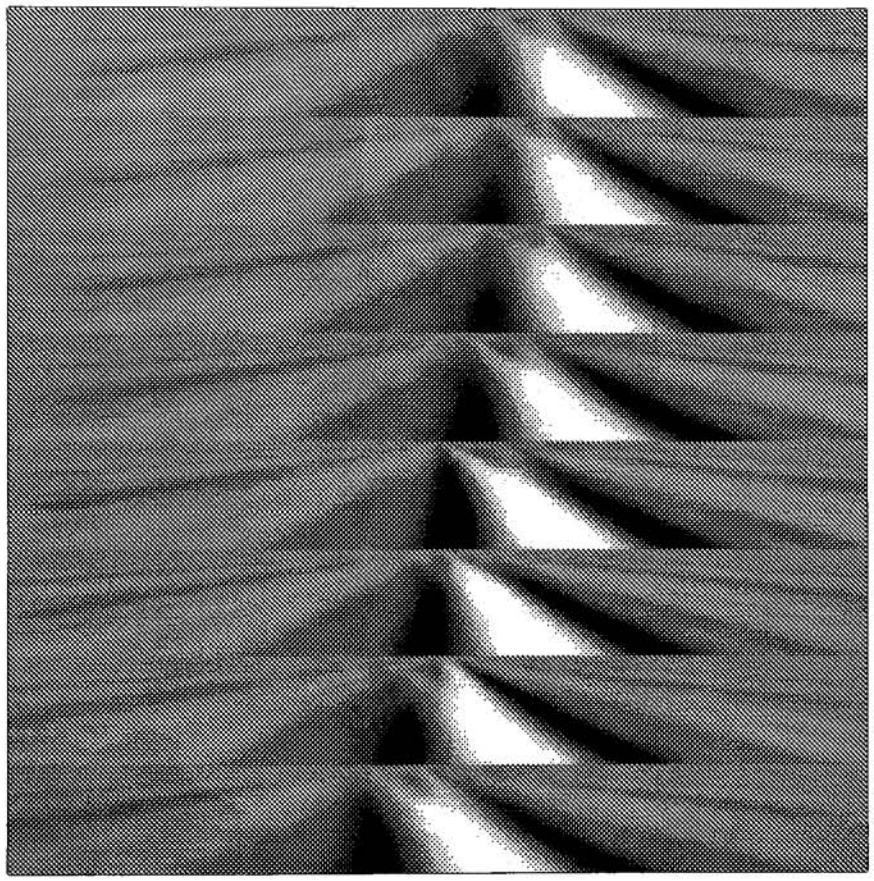

Figure 7.24: Wavelet Radon Transform of Test image projections - pass 0

The maximum scale vector for the test image is given as

$$\tilde{\mathbf{a}} = \begin{bmatrix} 64 \\ 64 \\ 60 \\ 56 \\ 48 \\ 41 \\ 54 \\ 60 \end{bmatrix}. \tag{7.16}$$

The results of circularly correlating $\tilde{\mathbf{a}}$ with $\mathbf{a}$ in (7.9) is shown in Figure 7.25. The peak corresponds to

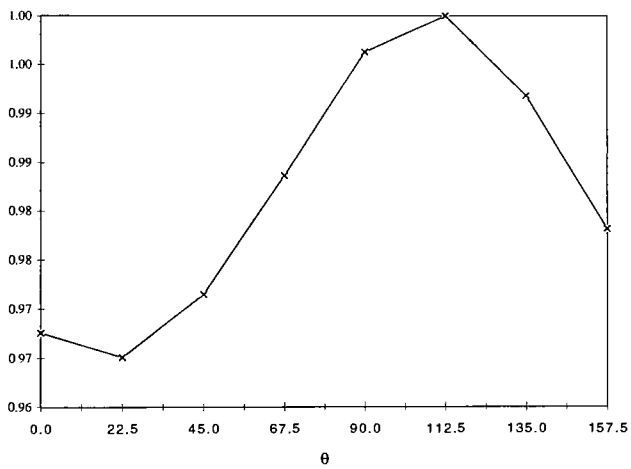

Figure 7.25: Normalized Circular Correlation, $\mathbf{s}$ - Test image

$\theta = 112.5°$, as expected. The vector, γ, is calculated using (7.13) to be

$$\gamma = \begin{bmatrix} 1.464 \\ 1.688 \\ 1.538 \\ 1.524 \\ 1.488 \\ 1.463 \\ 1.514 \\ 1.548 \end{bmatrix}. \tag{7.17}$$

The mean, $\mu = 1.529$, and standard deviation, $\sigma = 0.0671$, of γ give the scale factor and goodness of fit of the test object to the training object. The mean is close to the actual scale factor of 1.5 and σ is very small indicating that the object is in fact the fighter aircraft used for training.

The results of backprojecting both the detected signals, $\hat{q}_i^0(\rho)$, and the detail signals, $q_i^1(\rho)$ are shown in Figure 7.26a and b. Notice that Figure 7.26b looks very much like Figure 7.21b. The estimated details survived scaling, rotation, translation and noise. These details can be used as additional templates to a human observer to verify the automatic detection results or for further more detailed classfication.

The WRT of $q_i^1(\rho)$ using the matched wavelets for pass 1 is shown in Figure 7.27. The projection details and their detected estimates are shown in Figure 7.28. The backprojected results of detection in pass 1 and the new details are shown in Figure 7.26 c and d. The results of pass 1 are shown in Figures 7.28, 7.27, and 7.26c and d.

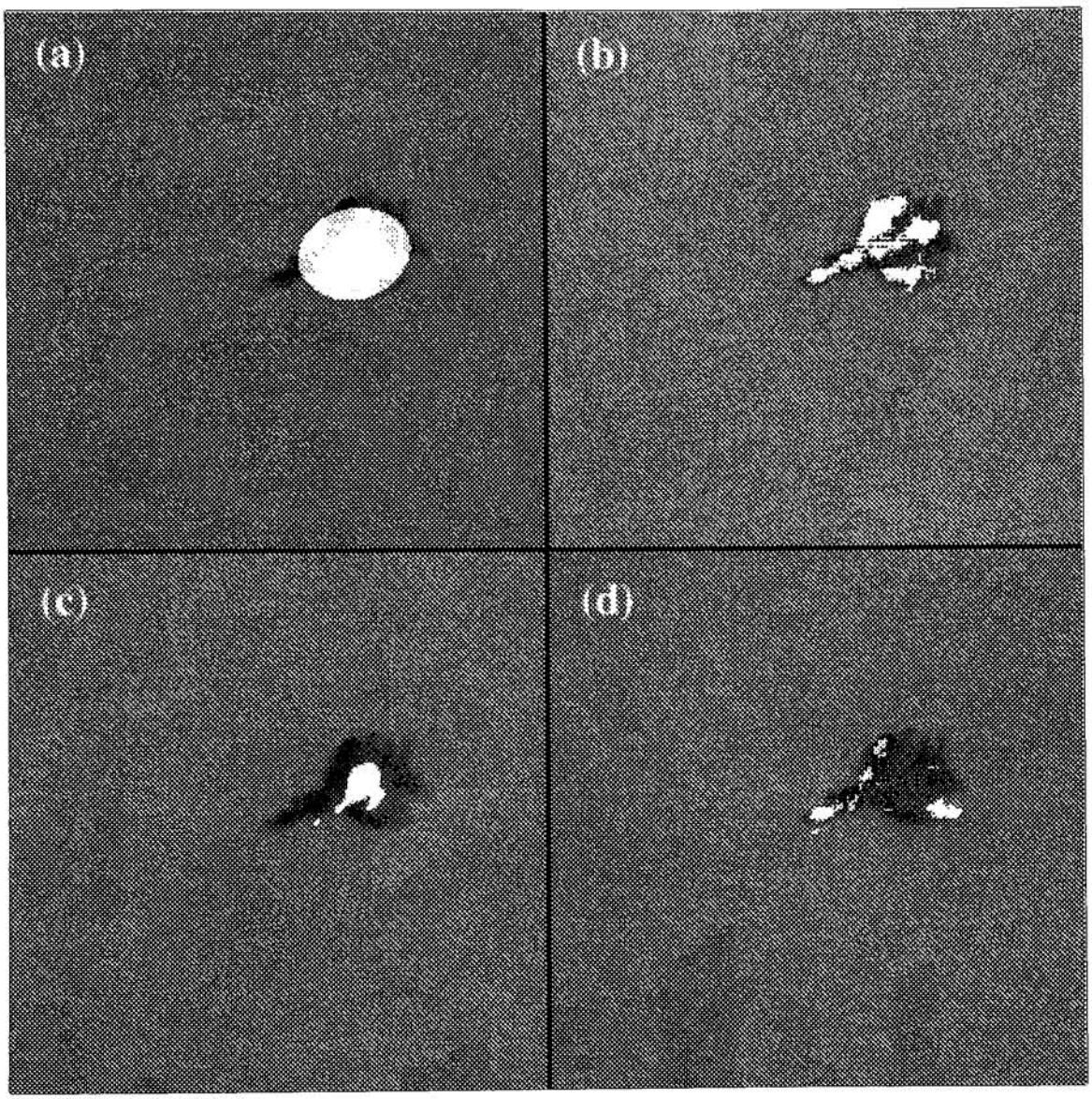

Figure 7.26: Results of backprojected detection and detail signals - Test image

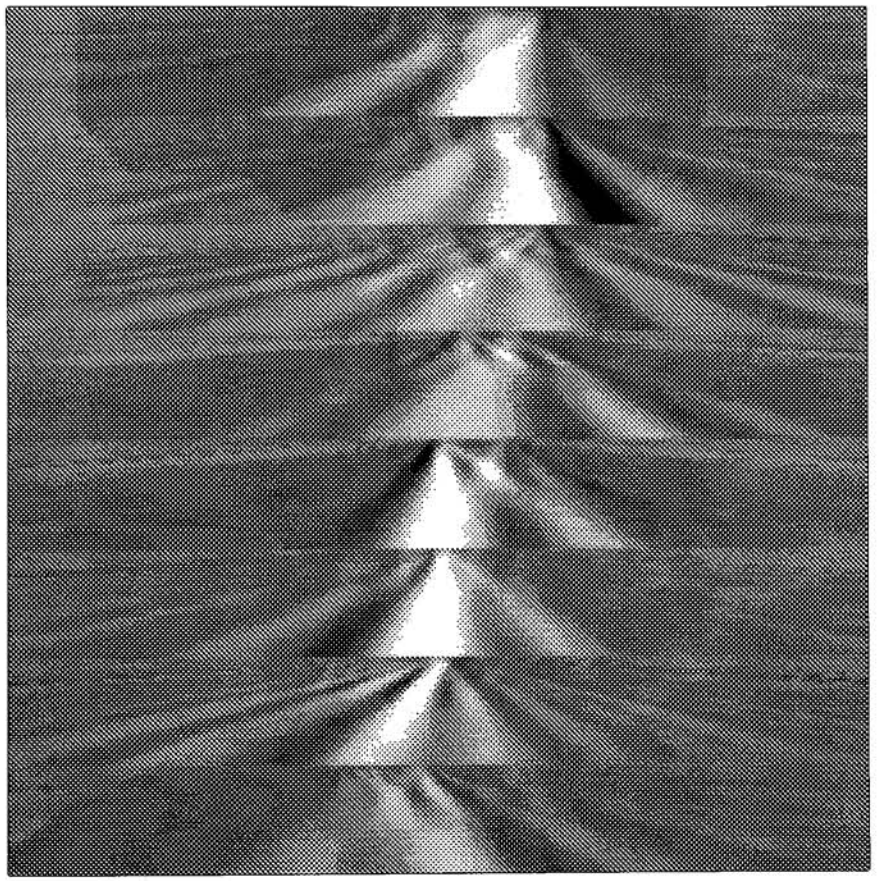

Figure 7.27: Wavelet Radon Transform of Test image projections - pass 1

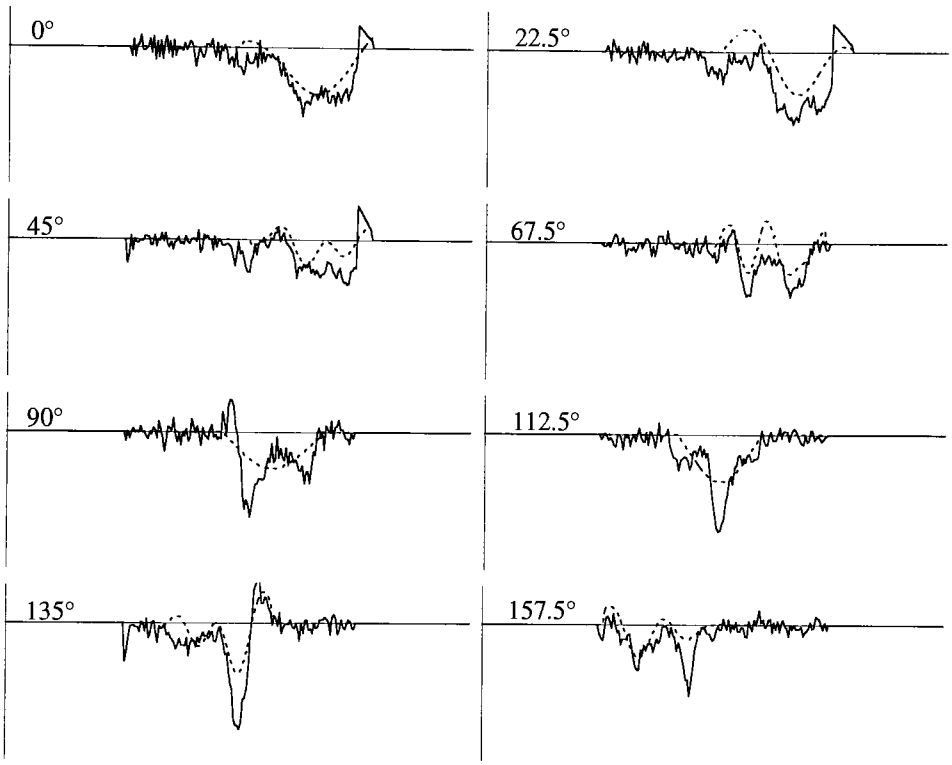

Figure 7.28: Test image projections and their estimate - pass 1

Chapter 8

Summary

The research results presented in this dissertation show by proof and example that it is possible to design bandlimited wavelets that optimally match a signal of interest in the least squares sense. The algorithm developed can be constrained such that the resultant wavelets either form an orthonormal basis of $L^2(\Re)$ or are dyadic wavelets that satisfy the stability condition. The development of the wavelet matching algorithm provides insight into the characteristics of both the amplitude and phase of an orthonormal wavelet spectrum. The wavelet matching algorithm is superior to existing wavelet design techniques in that it places the design emphasis on the shape of the wavelet and the RMS error with respect to the signal of interest. The target detection and identification algorithm was developed to be shift, scale and rotation invariant with optimal detection capability by combining the Radon Transform, backprojection and the Continuous Wavelet Transform with matched wavelets. It was demonstrated to work well with a target against a benign background embedded in white noise. The residual projection details were shown to survive rotation, shift, scale and noise. The second level of residual projections, however, did not survive, which was due to their small amplitudes relative to the projections from the first pass. The matched wavelets increased the detection performance as expected since they were specifically designed to match the projections under analysis. As the targets and backgrounds become more complicated, this optimal performance should prove beneficial in detecting targets in clutter.

8.1 Future Research

The next logical development step for the wavelet matching algorithm is to extend it to bi-orthogonal wavelets, that is, wavelets that reside in a multiresolution analysis (MRA) context whose duals reside in a dual MRA. The QMF constraints exploited in the development of the matching algorithm in this dissertation become much more complicated for bi-orthogonal wavelets. This added complication will need to be overcome before the algorithm can be extended to bi-orthogonal wavelets.

The target detection and identification algorithm can be improved to include targets in clutter. Surrounding clutter will add significant unwanted energy to the projections. It may be necessary to take windowed Radon Transforms to eliminate the unwanted energy from other parts of the scene. The identification capability based on aspect ratio can be improved to full classification capability by applying pattern classification techniques to the residual detail signals from the first pass. Also, increasing the number of projections, while increasing the computational burden, may increase the algorithm's performance significantly.

8.2 Conclusion

Wavelet theory and its applications are exciting and growing fields. The zoom in, zoom out capability of the wavelet transform and the ability to build matched wavelets makes their application to image processing even more significant. The engineering community is still on the threshold of developing solid, useful applications of wavelets in signal processing that truly take advantage of all that wavelets have to offer. Like many other engineers and scientists, much of the research conducted in support of this dissertation was focused on developing an in-depth understanding of wavelets and their characteristics. It seems clear that once the engineering community has the same depth of understanding of wavelet theory as they do for Fourier theory, they will develop new applications that are ideally suited to wavelets and the advantages they hold.

Appendices

Appendix A: Proof – Guaranteeing Orthonormality

Substituting $\omega = \eta + 2\pi m$ in (5.37) gives

$$|\Phi(\eta + 2\pi m)|^2 = \begin{cases} 1 & \text{for } \eta + 2\pi m = 0 \\ \sum_{n=0}^{\infty} \left|\Psi\left(2^{n+1}(\eta + 2\pi m)\right)\right|^2 & \text{for } \eta + 2\pi m \neq 0 \end{cases}. \tag{A-1}$$

Summing both sides of (A-1) over m gives

$$\sum_{m=-\infty}^{\infty} |\Phi\left(\eta + 2\pi m\right)|^2 = \begin{cases} 1 & \eta + 2\pi m = 0 \\ \sum_m \sum_n \left|\Psi\left(2^{n+1}(\eta + 2\pi m)\right)\right|^2 & \eta + 2\pi m \neq 0 \end{cases}. \tag{A-2}$$

The left side of (A-2) is the Poisson summation, which by (5.16) must is 1 everywhere when $\phi_{j,k}$ is an orthonormal basis of V_j. Therefore, because of the equality in (5.37), $\phi_{j,k}$ is an orthonormal basis of V_j if and only if

$$\sum_{m=-\infty}^{\infty} \sum_{n=0}^{\infty} \left|\Psi\left(2^{n+1}(\eta + 2\pi m)\right)\right|^2 = 1. \tag{A-3}$$

□

Appendix B: Proof–Bandlimited Φ

The Fourier transform of the scaling function's 2-scale relation is given as

$$\Phi(\omega) = H\left(\frac{\omega}{2}\right) \Phi\left(\frac{\omega}{2}\right). \tag{B-1}$$

From this expression, it is clear that the maximum bandwidth of $\Phi(\omega)$ is equal to the maximum bandwidth of one period of $H(\omega/2)$. Let the maximum half-bandwidth of $\Phi(\omega)$ be given as $\alpha\pi$ then the maximum half-bandwidth of one period of $H(\omega)$ is also $\alpha\pi$. The maximum half-bandwidth of $\Phi(\omega/2)$ is $2\alpha\pi$. In order for (B-1) to be satisfied for bandlimited scaling functions, $\Phi(\omega/2)$ must not extend into the second period of $H(\omega/2)$, which implies

$$\begin{aligned} 2\alpha\pi &\leq 4\pi - \alpha\pi \\ \alpha &\leq \frac{4}{3}. \end{aligned} \tag{B-2}$$

The maximum scaling function bandwidth is therefore $|\omega| \leq 4\pi/3$.

□

Appendix C: Proof–Bandlimited Ψ

Let ω_{max}^{Ψ} and ω_{max}^{Φ} be the upper frequency bounds of bandlimited Ψ and Φ, respectively. From (5.37)

$$|\Phi(\omega)|^2 = |\Psi(2\omega)|^2 + |\Psi(4\omega)|^2 + \cdots \qquad \text{for } \omega \neq 0. \tag{C-1}$$

Clearly, the upper frequency bound of $\Phi(\omega)$ is due to $\Psi(2\omega)$ only. Therefore,

$$\omega_{max}^{\Psi} = 2\omega_{max}^{\Phi} = \frac{8\pi}{3}. \tag{C-2}$$

If $\phi(x-k)$ is orthonormal, its Poisson summation must be 1 everywhere,

$$\sum_{m=-\infty}^{\infty} |\Phi(\omega + 2\pi m)|^2 = 1 \tag{C-3}$$

which for bandlimited scaling functions (Theorem 6) implies

$$|\Phi(\omega)| = 1 \qquad \text{for } \tfrac{-2\pi}{3} \leq |\omega| \leq \tfrac{2\pi}{3}. \tag{C-4}$$

Let the lower frequency bound of Ψ be given as ω_{min}^{Ψ}, so that the bandlimits of $\Psi(\omega)$ is $\omega_{min}^{\Psi} \leq |\omega| \leq 8\pi/3$. Let $\Phi_1(\omega)$ be the portion of Φ between $\pi/3$ and $2\pi/3$. From (C-1) and (C-2)

$$|\Phi_1(\omega)|^2 = |\Psi(2\omega)|^2 + |\Psi(4\omega)|^2 = 1 \qquad \text{for } \tfrac{\pi}{3} \leq |\omega| \leq \tfrac{2\pi}{3}. \tag{C-5}$$

Let $\Phi_2(\omega)$ be the portion of Φ between $\pi/6$ and $\pi/3$ and $\Psi_2(\omega)$ the portion of Ψ between $\pi/3$ and $2\pi/3$, then

$$\begin{aligned} |\Phi_2(\omega)|^2 &= |\Psi(2\omega)|^2 + |\Psi(4\omega)|^2 + |\Psi(8\omega)|^2 = 1 \\ &= |\Psi_2(2\omega)|^2 + |\Phi_1(2\omega)|^2 \qquad = 1 \qquad \text{for } \tfrac{\pi}{6} \le |\omega| \le \tfrac{\pi}{3}. \\ &= |\Psi_2(2\omega)|^2 + 1 \qquad = 1 \end{aligned} \tag{C-6}$$

So,

$$|\Psi_2(\omega)|^2 = 0 \qquad \text{for } \tfrac{\pi}{3} \le |\omega| \le \tfrac{2\pi}{3}. \tag{C-7}$$

We can generalize this approach by letting $\Phi_j(\omega)$ be the portion of Φ between $2\pi/3 \cdot 2^j$ and $4\pi/3 \cdot 2^j$ and $\Psi_j(\omega)$ be the portion of Ψ between $4\pi/3 \cdot 2^j$ and $8\pi/3 \cdot 2^j$, for $j = \{2, 3, \ldots, \infty\}$, then

$$|\Phi_j(\omega)|^2 = \textstyle\sum_{k=0}^{j} |\Psi(2^{k+1}\omega)|^2 = 1 \qquad \text{for } \tfrac{2\pi}{3\cdot 2^j} \le |\omega| \le \tfrac{4\pi}{3\cdot 2^j}. \tag{C-8}$$

However, for any value of j, $\Psi_{j-1}(\omega)$ has already been shown to be 0, so that

$$\begin{aligned} \sum_{k=0}^{j} |\Psi(2^{k+1}\omega)|^2 &= |\Psi_j(2\omega)|^2 + \sum_{n=2}^{j-1} |\Psi_n(2^{j-n+1}\omega)|^2 + |\Phi_1(2^{j-1}\omega)|^2 \\ &= |\Psi_j(2\omega)|^2 + 1. \end{aligned} \tag{C-9}$$

Substituting back into (C-8) gives

$$|\Phi_j(\omega)|^2 = |\Psi_j(2\omega)|^2 + 1 = 1 \qquad \text{for } \tfrac{2\pi}{3\cdot 2^j} \le |\omega| \le \tfrac{4\pi}{3\cdot 2^j}. \tag{C-10}$$

Therefore,

$$\Psi_j(2\omega) = 0 \qquad \text{for } \tfrac{2\pi}{3\cdot 2^j} \le |\omega| \le \tfrac{4\pi}{3\cdot 2^j} \tag{C-11}$$

and

$$\Psi_j(\omega) = 0 \qquad \text{for } \tfrac{4\pi}{3\cdot 2^j} \le |\omega| \le \tfrac{8\pi}{3\cdot 2^j}. \tag{C-12}$$

Combining all $\Psi_j(\omega)$ for $\{j = 2, 3, \ldots, \infty\}$ gives

$$|\Psi(\omega)|^2 = 0 \qquad \text{for } 0 \le |\omega| \le \tfrac{2\pi}{3}. \tag{C-13}$$

Therefore, $\omega_{min}^{\Psi} = 2\pi/3$ and the bandlimits on Ψ for bandlimited Φ in an orthonormal MRA is

$$\frac{2\pi}{3} \le |\omega| \le \frac{8\pi}{3}. \tag{C-14}$$

□

Appendix D: Proof–Guaranteeing an Orthonormal MRA

Let $|\Psi(k\Delta\omega)|$ be a sampled wavelet spectrum in an orthonormal MRA with sample spacing $\Delta\omega_\Psi = 2\pi/2^M$. According to Theorem 4, we can calculate the scaling function spectrum at any value, $|\Phi(k\pi/2^\ell)|$, using (5.29), where $\ell = \{0, 1, \ldots, M\}$. Let $\Delta\omega = \pi/2^\ell$ in (5.29), then

$$|\Phi(n\Delta\omega)|^2 = \sum_{p=0}^{\ell} \left| \Psi\left(\frac{2^{\ell+1} n \Delta\omega}{2^p} \right) \right|^2 . \tag{D-1}$$

Substituting $n\Delta\omega = n\Delta\omega + 2\pi m$ and summing over m gives

$$\sum_{m=-\infty}^{\infty} |\Phi(n\Delta\omega + 2\pi m)|^2 = \sum_{m=-\infty}^{\infty} \sum_{p=0}^{\ell} \left| \Psi\left(\frac{2^{\ell+1}}{2^p} (n\Delta\omega + 2\pi m) \right) \right|^2 . \tag{D-2}$$

The left side of (D-2) is the Poisson summation sampled at $\Delta\omega$ and is therefore equal to 1. Substituting back in for $\Delta\omega$ gives

$$\sum_{m=-\infty}^{\infty} \sum_{p=0}^{\ell} \left| \Psi\left(\frac{2\pi}{2^p} \left(n + 2^{\ell+1} m \right) \right) \right|^2 = 1. \tag{D-3}$$

Let $Y(k) = |\Psi(k\Delta\omega_\Psi)|^2$ where $\Delta\omega_\Psi = 2\pi/2^M$, then the constraint on Y becomes

$$\sum_{m=-\infty}^{\infty} \sum_{p=0}^{\ell} Y\left(\frac{2^M}{2^p} \left(n + 2^{\ell+1} m \right) \right) = 1 \tag{D-4}$$

$$\text{for } \ell = \{0, 1, \ldots, M\}. \tag{D-5}$$

Rewriting (5.42) in Corollary 7 for sampled wavelet spectra gives

$$\frac{2\pi}{3} \leq |k\Delta\omega| \leq \frac{8\pi}{3}. \tag{D-6}$$

Dividing through by $\Delta\omega = 2\pi/2^M$ gives the index constraint on k.

$$\frac{2^M}{3} \leq |k| \leq \frac{2^{M+2}}{3}. \tag{D-7}$$

Substituting the index of Y in (D-4) gives the bandlimit constraint on the samples of Y.

$$\frac{2^M}{3} \leq \left| \frac{2^M}{2^p} \left(n + 2^{\ell+1} m \right) \right| \leq \frac{2^{M+2}}{3}. \tag{D-8}$$

□

Appendix E: Proof–Matched Wavelet Amplitude

The problem of finding the optimal $\mathbf{Y}$ given the error

$$E = \frac{(\mathbf{W}-\mathbf{Y})^T(\mathbf{W}-\mathbf{Y})}{\mathbf{W}^T\mathbf{W}} \tag{E-1}$$

and the equality constraints

$$\mathbf{AY} = \mathbf{1} \tag{E-2}$$

can be solved easily using Lagrangian multipliers. The Lagrangian is given as

$$L = \frac{(\mathbf{W}-\mathbf{Y})^T(\mathbf{W}-\mathbf{Y})}{\mathbf{W}^T\mathbf{W}} + \lambda^T(\mathbf{AY}-\mathbf{1}). \tag{E-3}$$

The error function, E, is minimized by setting $\nabla_Y L = 0$, $\nabla_\lambda L = 0$ and solving for $\mathbf{Y}$ [21].

$$\nabla_Y L = \frac{2}{\mathbf{W}^T\mathbf{W}}(\mathbf{W}-\mathbf{Y}) + \mathbf{A}^T\lambda = 0. \tag{E-4}$$

Setting $\nabla_\lambda L = 0$, we get back our equality constraints.

$$\mathbf{AY} = \mathbf{1}. \tag{E-5}$$

Multiplying (E-4) by $\mathbf{A}$ and substituting (E-5) gives a solution for λ.

$$\begin{aligned}
\frac{2}{\mathbf{W}^T\mathbf{W}}(\mathbf{AW}-\mathbf{AY}) + \mathbf{AA}^T\lambda &= 0 \\
\frac{2}{\mathbf{W}^T\mathbf{W}}(\mathbf{AW}-\mathbf{1}) + \mathbf{AA}^T\lambda &= 0 \\
\frac{2}{\mathbf{W}^T\mathbf{W}}(\mathbf{AA}^T)^{-1}(\mathbf{1}-\mathbf{AW}) &= \lambda.
\end{aligned} \tag{E-6}$$

Substituting (E-6) back into (E-4) gives the solution for $\mathbf{Y}$.

$$\mathbf{Y} = \mathbf{W} + \mathbf{A}^T(\mathbf{AA}^T)^{-1}(\mathbf{1}-\mathbf{AW}) \tag{E-7}$$

and substituting (E-7) into (E-1) gives the error in the match,

$$\begin{aligned}
E &= \frac{-(\mathbf{A}^T(\mathbf{AA}^T)^{-1}(\mathbf{1}-\mathbf{AW}))^T(-1)(\mathbf{A}^T(\mathbf{AA}^T)^{-1}(\mathbf{1}-\mathbf{AW}))}{\mathbf{W}^T\mathbf{W}} \\
&= \frac{(\mathbf{1}-\mathbf{AW})^T(\mathbf{AA}^T)^{-T}\mathbf{AA}^T(\mathbf{AA}^T)^{-1}(\mathbf{1}-\mathbf{AW})}{\mathbf{W}^T\mathbf{W}} \\
&= \frac{(\mathbf{1}-\mathbf{AW})^T(\mathbf{AA}^T)^{-1}(\mathbf{1}-\mathbf{AW})}{\mathbf{W}^T\mathbf{W}}.
\end{aligned} \tag{E-8}$$

Because $\mathbf{Y}$ is a power spectrum, we must add the inequality constraints

$$Y(k) \geq 0 \qquad \text{for all } k. \tag{E-9}$$

Note: If an element of $\mathbf{Y}$ *is negative, then we must add an equality constraint forcing that element to* 0. *This is done by appending a* 0 *to* $\mathbf{1}$ *and adding a row to the bottom of* $\mathbf{A}$ *containing all* 0*'s and a* 1 *in the column corresponding to the negative element.*

Notice in (E-7) and (E-8) that $\mathbf{Y}$ and E are very much dependent on the amplitude of $\mathbf{W}$. Since the matched wavelet must match the desired signal up to a scale factor, K, as shown in (5.4), we can scale $\mathbf{W}$ so that E is minimized. Let the scale factor be $1/a$ so that the desired signal spectrum is $\mathbf{W}/a$. The error function becomes

$$E(a) = \frac{(\mathbf{1} - \frac{1}{a}\mathbf{AW})^T(\mathbf{AA}^T)^{-1}(\mathbf{1} - \frac{1}{a}\mathbf{AW})}{\frac{1}{a^2}\mathbf{W}^T\mathbf{W}} \tag{E-10}$$

and the solution for $\mathbf{Y}$ becomes

$$\mathbf{Y} = \frac{1}{a}\mathbf{W} + \mathbf{A}^T(\mathbf{AA}^T)^{-1}(\mathbf{1} - \frac{1}{a}\mathbf{AW}). \tag{E-11}$$

Setting $dE(a)/da = 0$ gives

$$\begin{aligned}
\frac{d}{da}\frac{(\mathbf{1} - \frac{1}{a}\mathbf{AW})^T(\mathbf{AA}^T)^{-1}(\mathbf{1} - \frac{1}{a}\mathbf{AW})}{\frac{1}{a^2}\mathbf{W}^T\mathbf{W}} &= 0 \\
\frac{d}{da}\frac{(a\mathbf{1} - \mathbf{AW})^T(\mathbf{AA}^T)^{-1}(a\mathbf{1} - \mathbf{AW})}{\mathbf{W}^T\mathbf{W}} &= 0 \\
\frac{1}{\mathbf{W}^T\mathbf{W}}\left[(a\mathbf{1} - \mathbf{AW})^T(\mathbf{AA}^T)^{-1}\mathbf{1} + \mathbf{1}^T(\mathbf{AA}^T)^{-1}(a\mathbf{1} - \mathbf{AW})\right] &= 0 \\
\frac{2}{\mathbf{W}^T\mathbf{W}}\left[\mathbf{1}^T(\mathbf{AA}^T)^{-1}(a\mathbf{1} - \mathbf{AW})\right] &= 0.
\end{aligned} \tag{E-12}$$

Solving for a in (E-12) gives the expression for the scale factor that will minimize the error function E,

$$a = \frac{\mathbf{1}^T(\mathbf{AA}^T)^{-1}\mathbf{AW}}{\mathbf{1}^T(\mathbf{AA}^T)^{-1}\mathbf{1}}. \tag{E-13}$$

Because, the conditions on Ψ from Theorem 8 are satisfied through the constraints of the optimization equations, the scaling function spectrum calculated by way of (5.29) generates an orthonormal MRA.

Appendix F: Proof–Properties of Λ_Φ, Λ_Ψ, and λ

The proofs for (5.62), (5.63) and (5.64) are trivial. Since $\phi(x)$, $\psi(x)$, and h_k are all real quantities, their Fourier Transforms are Hermitian[3], that is, their magnitude is even and their phase is odd. Therefore, θ_Φ, θ_Ψ, and θ_H are odd functions. Since the derivative of an odd function is an even function if follows that $\Lambda_\Phi(\omega)$, $\Lambda_\Psi(\omega)$, and $\lambda(\omega)$ are all even functions. In order to prove (5.65) and (5.66), let $\lambda_0(\omega) = \lambda(\omega) - \bar{\lambda}$, where

$$\bar{\lambda} = \frac{1}{2\pi}\int_{-\pi}^{\pi} \lambda(\omega) d\omega \tag{F-1}$$

so that

$$\frac{1}{2\pi}\int_{-\pi}^{\pi} \lambda(\omega)_0 d\omega = 0. \tag{F-2}$$

The average value of $\Lambda_\Phi(\omega)$ is given by

$$\begin{aligned}
\int_{-\infty}^{\infty} \Lambda_\Phi(\omega) d\omega &= \int_{-\infty}^{\infty} \sum_{m=1}^{\infty} 2^{-m} \lambda\left(\frac{\omega}{2^m}\right) d\omega \\
&= \int_{-\infty}^{\infty} \sum_{m=1}^{\infty} 2^{-m} \left[\lambda_0\left(\frac{\omega}{2^m}\right) + \bar{\lambda}\right] d\omega \\
&= \sum_{m=1}^{\infty} 2^{-m} \left[\frac{1}{2\pi}\int_{-\pi}^{\pi} \left(\lambda_0\left(\frac{\omega}{2^m}\right) + \bar{\lambda}\right) d\omega\right] \\
&= \bar{\lambda} \sum_{m=1}^{\infty} 2^{-m} \\
&= \bar{\lambda}.
\end{aligned} \tag{F-3}$$

Similarly for $\Lambda_\Psi(\omega)$

$$\begin{aligned}
\int_{-\infty}^{\infty} \Lambda_\Psi(\omega) d\omega &= \int_{-\infty}^{\infty} -\frac{1}{2} - \frac{1}{2}\lambda\left(\frac{\omega}{2} + \pi\right) + \sum_{m=2}^{\infty} 2^{-m} \lambda\left(\frac{\omega}{2^m}\right) d\omega \\
&= \frac{1}{2\pi}\int_{-\pi}^{\pi} -\frac{1}{2} - \frac{1}{2}\lambda\left(\frac{\omega}{2} + \pi\right) + \sum_{m=2}^{\infty} 2^{-m} \lambda\left(\frac{\omega}{2^m}\right) d\omega \\
&= \frac{1}{2\pi}\int_{-\pi}^{\pi} -\frac{1}{2} - \frac{1}{2}\left(\lambda_0\left(\frac{\omega}{2} + \pi\right) + \bar{\lambda}\right) + \sum_{m=2}^{\infty} 2^{-m} \left(\lambda_0\left(\frac{\omega}{2^m}\right) + \bar{\lambda}\right) d\omega \\
&= -\frac{1}{2} - \frac{1}{2}\bar{\lambda} + \bar{\lambda} \sum_{m=2}^{\infty} 2^{-m} \\
&= -\frac{1}{2} - \frac{1}{2}\bar{\lambda} + \frac{1}{2}\bar{\lambda} \\
&= -\frac{1}{2}.
\end{aligned} \tag{F-4}$$

Appendix G: Continuous Wavelet Transform Implementation

The continuous wavelet transform is given by the following expression,

$$W_f(a,b) = \int_{-\infty}^{\infty} f(x) a^{-\frac{1}{2}} \psi\left(\frac{x-b}{a}\right) dx. \tag{G-1}$$

The wavelets used in this dissertation are discrete functions, $\psi(k) = \psi(k\Delta x)$, calculated using the matching algorithm of Chapter 5. Implementing the CWT with discrete quantities is done with summation rather than integration and the result is actually only an approximation to the CWT. The approximation to (G-1) is given by

$$W_f(m,n) = \sum_{k=-N/2}^{N/2-1} f(k\Delta x)\psi\left(\frac{k\Delta x - n\Delta b}{m\Delta a}\right) \tag{G-2}$$

where N is the number of points in $f(k\Delta x)$ and $\psi(k\Delta x)$. In order to simplify (G-2), assume $\Delta b = \Delta x$, which provides the finest translation steps possible, since the shift parameter cannot step any smaller than Δx. Rewriting (G-2) and dropping the Δx's gives

$$W_f(m,n) = \sum_{k=-N/2}^{N/2-1} f(k)\psi\left(\frac{k-n}{m\Delta a}\right) \tag{G-3}$$

which can be written in matrix notation as

$$W_f(m) = \mathbf{f}^T \mathbf{\Psi_m}^T \tag{G-4}$$

where $W_f(m)$ is row m of the approximate CWT and has length, N, $\mathbf{f}$ is a $N \times 1$ vector consisting of the samples of the input signal, $f(x)$, and $\mathbf{\Psi_m}$ is a $N \times N$ matrix where each row consists of the sampled wavelet, dilated to scale $m\Delta a$ and shifted by n, that is, $\psi(k-n)/m\Delta a$.

All approximate CWTs in this dissertation will be calculated for 64 discrete scales. Furthermore, as in Chapters 6 and 7, $N = 512$, $\Delta x = 1/32$, and $\Delta\omega = \pi/8$. Let $\psi(k)$ be the discrete wavelets calculated by the matching algorithm of Chapter 5 with the parameters given above. Because $\Delta x = 1/32$, $\psi(k)$ can be decimated up to 5 times giving $\sqrt{32}\psi(32k)$, where now $\Delta x = 1$. In this implementation, however, $\psi(k)$ is decimated only 4 times since a fifth decimation produces a function with only one non-zero value. So, if $\sqrt{16}\psi(16k)$ is used to calculate the first row of the CWT which would represent the smallest scale,

then $\sqrt{8}\psi(8k)$ will be used to calculate the second row, $\sqrt{4}\psi(4k)$ the fourth row, $\sqrt{2}\psi(2k)$ the eighth row and $\psi(k)$ the sixteenth row. Upsampling and interpolating $\psi(k)$ gives $\psi(k/2)$, which will be used to calculate the 32nd row of the CWT and upsampling and interpolating again gives $\psi(k/4)$, which will be used to calculate row 64 of the CWT. There are now discrete wavelets that will calculate the CWT at rows 2^j for $j = 0, 1, \ldots, 6$. The wavelets that will be used to calculate the other, non-dyadic rows, are found by interpolating the wavelets at the dyadic rows. For instance, to find the wavelet corresponding to the 23rd row of the CWT, the wavelet corresponding to row 16 is upsampled by a factor of $23/16$, which is done by upsampling and interpolating by a factor of $23/1$ and taking every 16th sample. Now that the wavelets corresponding to every scale in the output CWT has been calculated, they can be used in (G-4) to find the approximate CWT.

Bibliography

[1] P. Abry and A. Aldroubi. "Designing multiresolution analysis-type wavelets and their fast algorithms". Preprint.

[2] A. Aldroubi and M. Unser. "Families of multiresolution and wavelet spaces with optimal properties". *Numerical Functional Analysis and Optimization*, 14(5-6):417–446, 1993.

[3] R. N. Bracewell. *The Fourier Transform and Its Applications*, pages 14–16. McGraw–Hill Book Co., 1986.

[4] R. N. Bracewell. "Strip integration in radio astronomy". *Australian Journal of Physics*, 9:198–217, 1956.

[5] R. N. Bracewell. *Two-dimensional imaging*, chapter 6. Prentice Hall, Englewood Cliffs, NJ, 1995.

[6] P. J. Burt and E. H. Adelson. "The Laplacian pyramid as a compact image code". *IEEE Transactions in Communications*, COM-31:532–540, April 1983.

[7] J. O. Chapa and M. R. Raghuveer. "Constructing MRAs from desired wavelet functions". In *Proceedings on Asilomar Conference on Signals, Systems and Computers*, pages 1109–1113, IEEE, October 1994.

[8] J. O. Chapa and M. R. Raghuveer. "Optimal matched wavelet construction and its application to image pattern recognition". In *Wavelet Applications II*, pages 518–529, SPIE, April 1995.

[9] S. Chen and D. Donoho. "Basis pursuit". In *Proceedings on IEEE 28th Annual Asilomar Conference on Signals, Systems and Computers*, November 1994.

[10] C. K. Chui. *An Introduction to Wavelets*, chapter 1-3,5,7. Volume 1 of *Wavelet Analysis and Its Application*, Academic Press, Inc., 1992.

[11] R. Coifman and M. Wickerhauser. "Entropy–based algorithms for best basis selection". *IEEE Transactions on Information Theory*, 38(2):713–718, March 1992.

[12] I. Daubechies. "Orthonormal bases of compactly supported wavelets". *Communications on Pure and Applied Mathematics*, 41:909–996, 1988.

[13] I. Daubechies. *Ten Lectures on Wavelets*, chapter 3-5. Society for Industrial and Applied Mathematics, 1992.

[14] I. Daubechies. "The wavelet transform, time-frequency localization and signal analysis". *IEEE Transactions on Information Theory*, 36(5):961–1005, September 1990.

[15] S. R. Deans. *The Radon Transform and Some of Its Applications*, chapter 2,5,6. John Wiley and Sons, New York, NY, 1983.

[16] D. Gabor. "Theory of communication". *Journal of the IEE*, 93, 1946.

[17] J. D. Gaskill. *Linear Systems, Fourier Transforms, and Optics*, chapter 4. John Wiley and Sons, 1978.

[18] R. A. Gopinath, J. E. Odegard, and C. S. Burrus. "Optimal wavelet representation of signals and wavelet sampling theorem". *IEEE Transactions on Circuits and Systems–II: Analog and Digital Signal Processing*, 41(4):262–277, April 1994.

[19] G. Kaiser. *A Friendly Guide to Wavelets*, chapter 3,5,8. Birkhäuser, Boston, Massachusetts, 1994.

[20] W. M. Lawton. "Necessary and sufficient conditions for constructing orthonormal wavelet bases". *Journal of Mathematical Physics*, 32(1), January 1991.

[21] D. G. Luenberger. *Introduction to Linear and Nonlinear Programming*, pages 224–227. Addison–Wesley, 1973.

[22] D. G. Luenberger. *Optimization By Vector Space Methods*, chapter 2,3. John Wiley and Sons, 1969.

[23] S. G. Mallat. "A theory for multiresolution signal decompositions: the wavelet representation". *IEEE Transactions on Pattern Analysis and Machine Intelligence*, 11(7):674–693, July 1989.

[24] S. G. Mallat. "Multiresolution approximations and wavelet orthonormal bases of $L^2(\Re)$". *Transactions of the American Mathematical Society*, 315(1):69–87, September 1989.

[25] S. G. Mallat and Z. Zhang. "Matching pursuit with time-frequency dictionaries". *IEEE Transactions in Signal Processing*, 47(12), 1993.

[26] Y. Meyer. "Principe d'incertitude, bases hilbertiennes et algèbres d'opérateurs". *Séminaire Bourbaki*, 662, 1985-1986.

[27] Y. Meyer. *Wavelets and Operators*, chapter 2,3. Addison–Wesley, Cambridge University Press, 1992.

[28] Y. Pao. *Adaptive Pattern Recognition and Neural Networks*, pages 7–9, 43. Addison–Wesley, Reading, Massachusetts, 1989.

[29] J. Radon. "Über diebestimmung von funktionen durch ihre integralwerte längs gewisser mannigfaltigkeiten". *Berichte Sächsische Akademie der Wissenschaften. Leipzig, Math. Phys. Kl.*, 69:262–267, 1917.

[30] O. Rioul and M. Vetterli. "Wavelets and signal processing". *IEEE SP Magazine*, 8(4):14, October 1991.

[31] G. Strang. "Wavelets and dilation equations: a brief introduction". *Society for Industrial and Applied Mathematics*, 31(4):614–627, December 1989.

[32] W. Sweldens. *"The Lifting Scheme: A Custom-Design Construction of Biorthogonal Wavelets"*. Industrial Mathematics Initiative Research Report 1994:07, University of South Carolina, 1994.

[33] H. Szu, Y. Sheng, and J. Chen. "Wavelet transform as a bank of matched filters". *Applied Optics*, 31(17):3267–3277, June 1992.

[34] A. H. Tewfik, D. Sinha, and P. Jorgensen. "On the optimal choice of a wavelet for signal representation". *IEEE Transactions on Information Theory*, 38(2):747–765, March 1992.

[35] P. P. Vaidyanathan. "Multirate digital filters, filter banks, polyphase networks, and applications: a tutorial". *Proceedings of the IEEE*, 78(1):56–93, January 1990.

[36] M. V. Wickerhauser. Acoustic signal processing with wavelet packets. In C. K. Chui, editor, *Wavelets: A Tutorial In Theory and Applications*, pages 679–700, Academic Press, Cambridge, MA, 1992.